# INVESTIGATION OF WINTERTIME COLD-AIR POOLS AND AEROSOL LAYERS IN THE SALT LAKE VALLEY USING A LIDAR CEILOMETER

by

Joseph Swyler Young

A thesis submitted to the faculty of
The University of Utah
in partial fulfillment of the requirements for the degree of

Master of Science

Department of Atmospheric Sciences

The University of Utah

December 2013

**The University of Utah Graduate School**

# STATEMENT OF THESIS APPROVAL

The thesis of **Joseph Swyler Young**

has been approved by the following supervisory committee members:

| | | |
|---|---|---|
| **C. David Whiteman** | , Chair | **8/20/2013** Date Approved |
| **John D. Horel** | , Member | **8/20/2013** Date Approved |
| **Gerald G. Mace** | , Member | **8/20/2013** Date Approved |

and by **Kevin D. Perry** , Chair of the Department of **Atmospheric Sciences**

and by David B. Kieda, Dean of The Graduate School.

# ABSTRACT

This thesis investigates the utility of lidar ceilometers, a type of aerosol lidar, in improving the understanding of meteorology and air quality in persistent wintertime stable boundary layers, or cold-air pools, that form in urbanized valley and basin topography. This thesis reviews the scientific literature to survey the present knowledge of persistent cold-air pools, the operating principles of lidar ceilometers, and their demonstrated utility in meteorological investigations. Lidar ceilometer data from the Persistent Cold-Air Pool Study (PCAPS) are then used with meteorological and air quality data from other in situ and remote sensing equipment to investigate cold-air pools that formed in Utah's Salt Lake Valley during the winter of 2010-2011.

The lidar ceilometer is shown to accurately measure aerosol layer depth and aerosol loading, when compared to visual observations. A linear relationship is found between low-level lidar backscatter and surface particulate measurements. Convective boundary layer lidar analysis techniques applied to cold-air pool ceilometer profiles can detect useful layer characteristics. Fine-scale waves are observed and analyzed within the aerosol layer, with emphasis on Kelvin-Helmholz waves. Ceilometer aerosol backscatter profiles are analyzed to quantify and describe mixing processes in persistent cold-air pools. Overlays of other remote and in-situ observations are combined with ceilometer particle backscatter to describe specific events during PCAPS. This analysis describes the relationship between the aerosol layer and the valley inversion as well as interactions with large-scale meteorology.

The ceilometer observations of hydrometers are used to quantify cloudiness and precipitation during the project, observing that 50% of hours when a PCAP was present had clouds or precipitation below 5 km above ground level (AGL). Then, combining an objective technique for determining hourly aerosol layer depths and correcting this subjectively during periods with low clouds or precipitation, a time series of aerosol depths was obtained. The mean depth of the surface-based aerosol layer during PCAP events was 1861 m MSL with a standard deviation of 135 m. The aerosol layer depth, given the approximate 1300 m altitude of the valley floor, is thus about 550 m, about 46% of the basin depth. The aerosol layer is present during much of the winter and is removed only during strong or prolonged

precipitation periods or when surface winds are strong. Nocturnal fogs that formed near the end of high-stability PCAP episodes had a limited effect on aerosol layer depth.

Aerosol layer depth was relatively invariant during the winter and during the persistent cold-air pools, while $PM_{10}$ concentrations at the valley floor varied with bulk atmospheric stability associated primarily with passage of large-scale high- and low-pressure weather systems. $PM_{10}$ concentrations also increased with cold-air pool duration. Mean aerosol loading in the surface-based aerosol layer, as determined from ceilometer backscatter coefficients, showed weaker variations than those of surface $PM_{10}$ concentrations, suggesting that ineffective vertical mixing and aerosol layering are present in the cold-air pools. This is supported by higher time-resolution backscatter data, and it distinguishes the persistent cold-air pools from well-mixed convective boundary layers where ground-based air pollution concentrations are closely related to time-dependent convective boundary layer/aerosol depths.

These results are discussed along with recommendations for future explorations of the ceilometer and cold-air pool topics.

# CONTENTS

# LIST OF FIGURES

# LIST OF TABLES

# ACKNOWLEDGEMENTS

This thesis would not have been possible were it not for the support, patience, and opportunities I have received while working on it. First, the exhaustive efforts of my advisor, Dr. C. David Whiteman in guiding, editing, and supporting my research and writing process are greatly appreciated. The frequent assistance, conversation, and research opportunities from Drs. Sebastian Hoch, John Horel, Erik Crosman, and PhD student Neil Lareau are greatly appreciated. The PCAPS dataset would not have been possible without the other UU participants in the field program. NCAR EOL personnel operated the ceilometer and supplied the data. I also wish to thank Dr. Jay Mace for being a member of my committee and providing valuable feedback on this research, on lidars, and on ceilometers. I would also like to thank all my friends, family, and fellow graduate students for helping me get here today.

The research reported in this thesis was supported by Kennecott Utah Copper grant no. 10020948 and by National Science Foundation grant ATM-0938397. We thank the Jordan Valley Water Conservancy District in West Jordan, Utah for providing the operating location for the ceilometer.

# CHAPTER 1

# INTRODUCTION

Persistent or multiday stable boundary layers or cold-air pools often form in valleys and basins during wintertime when the weak daytime sensible heat flux is unable to remove the stable layer. If sources of air pollution are present, particulate pollutants may build up within the stable layer, leading to serious multiday air pollution episodes. Complex terrain, such as restricted basins, contribute to and enhance the processes which cause cold-air pool persistence. In the past, observational limitations prevented observation of important physical characteristics that govern these phenomena. Owing to high particulate concentrations, high-resolution lidar remote sensing techniques are ideal for studying persistent cold-air pools.

One type of aerosol lidar is the laser ceilometer, an instrument frequently deployed globally for measuring cloud base heights (cloud ceilings) by recording lidar backscatter. In recent studies, ceilometers have been shown to provide detailed observations of aerosol layers associated with surface-based convection over simple terrain. The low cost and low maintenance requirements make ceilometers a desirable observing platform for multilocation, remote, or long-term observations in often harsh cold-air pool environments.

In this thesis, the meteorology of particulate-laden cold-air pools in Utah's Salt Lake Valley is investigated using a laser ceilometer, a type of aerosol lidar. We also investigate the utility of laser ceilometers in gaining improved understanding of the meteorology of stable boundary layers in complex terrain. Our investigations are made using laser ceilometer and other supporting datasets collected in Utah's Salt Lake Valley in the winter of 2010-2011 as part of the Persistent Cold-Air Pool Study (PCAPS), as funded by the National Science Foundation.

This thesis begins with a survey of literature on cold-air pools (Chapter 2) and lidars (Chapter 3). This is followed in Chapter 4 by a description of the Persistent Cold-Air Pool Study conducted in 2010-2011 in Utah's Salt Lake Valley. The valley is described along with information on the types and locations of meteorological and air quality instruments

available for examination of persistent cold-air pool events. Chapter 5 presents analyses of the applications of laser ceilometers in the study of persistent cold-air pools. Analyses focus on ceilometer backscatter cross-sections and their use in determining the characteristics of persistent cold-air pools. Chapter 6 assesses the utility of the laser ceilometer in stable boundary layer investigations and summarizes the meteorological findings. Suggestions are also made for future work.

# CHAPTER 2

# COLD-AIR POOL BACKGROUND

This chapter presents the current state of knowledge regarding persistent cold-air pools, which are the phenomenon examined in this thesis. Complex terrain diurnal cold-air pools (CAPs) are discussed first, along with a survey of field and modeling observations that have been performed on these phenomena. PCAPS characteristics and processes leading to persistent cold-air pools are then discussed and compared to diurnal cold-air pools. Scientific questions on persistent cold-air pools are then presented along with a brief discussion of their societal impacts.

## 2.1 Cold-air pools and persistence

A cold-air pool (CAP) is a layer of stagnant air confined by topography and colder than the air above it (Whiteman et al. 2001). CAPs can form within any enclosed basin where cooler, more-dense air can accumulate (Bodine et al. 2009; Price et al. 2011). There are two types of cold-air pools, diurnal cold-air pools and persistent cold-air pools.

Diurnal cold-air pools or nocturnal temperature inversions generally form overnight due to turbulent sensible heat flux divergence and radiative flux divergence, although cold-air advection from nearby slopes and drainage basins can also play a significant role. They are destroyed the following day after sunrise by a convective boundary layer that grows upward from the heated ground (Whiteman 1982; Whiteman and McKee 1982; Whiteman et al. 2001, 2004). The stability and depth of the cold-air pool can be modulated by differential advection, differential vertical motion (Wolyn and McKee 1989), radiative flux divergence (Whiteman et al. 2004), and other physical processes. Diurnal cold-air pools in basins and valleys have received much study (e.g., Kondo et al. 1989; Whiteman et al. 2001, 2008; Doran et al. 2002; Clements et al. 2003; Zardi and Whiteman 2012). They are especially prominent in climate zones with weak winds aloft and clear skies and can undergo modification by larger-scale weather systems (Dorninger et al. 2011) and turbulent erosion (Petkovšek 1992; Zhong et al. 2003; Fritts et al. 2010).

Persistent cold-air pools (PCAPs) are CAPs that last for more than one day. These are most common in winter. Incoming solar radiation is reduced in winter and is often reflected back to space by snow-covered ground or low clouds. The lower radiation input to the ground reduces the sensible heat flux that drives convection. Thus, in winter, the CAPs are less likely to be broken diurnally by daytime convection and more likely to persist for multiple days. A PCAP can begin as a nocturnal CAP, as a layer of cold air left in the valley by the passage of a cold front (Whiteman et al. 2001), or when large-scale advection or subsidence increases air temperatures above the basin (Wolyn and McKee 1989; Whiteman et al. 1999). Because PCAPs persist for many days, they are subject to modification by passing synoptic-scale weather systems as well as by local-scale processes. These interactions are complex and nonlinear, making PCAPs a particularly difficult phenomenon to study and predict.

Once a persistent cold-air pool forms, there are many processes that can modify the strength of the stable layer, including differential large-scale advection, differential vertical motions, radiative influences from clouds, snow cover and atmospheric water vapor, and turbulent mixing and stresses (Zhong et al. 2001; Gillies et al. 2010). The diurnal formation of stable and unstable boundary layers over the sidewalls, and differential heating on opposing sidewalls, lead to up- and downslope flows (Whiteman et al. 2004) and cross-basin or cross-valley flows (Lehner et al. 2011) that redistribute heat and pollutants internally in the CAP. Noncontiguous mixing processes may occur within a PCAP, as well, affecting only parts of the basin. Partial mix-outs can occur, reducing energy deficits and pollution, but failing to eliminate the stable air mass (Whiteman et al. 2001).

The time of breakup of PCAPs is especially difficult to forecast and leads to large temperature forecast errors (Reeves and Stensrud 2009; Gillies et al. 2010). Modeling studies in real (Zängl 2005) and idealized (Zhong et al. 2003; Zoumakis and Efstathiou 2006) situations have identified numerous influences on the processes leading to CAP breakup.

A PCAP can be eventually broken up via the same convection mechanism that leads to the breakup of most diurnal CAPs (Whiteman et al. 2001). In valleys or basins, the advection of the stable air mass out of the valley may also play a role. The usual mechanism, however, is cold air advection aloft, and high winds and rising motions associated with the passage of low-pressure centers or troughs (Reeves and Stensrud 2009). If PCAPs were destroyed only by traveling low-pressure troughs, there would be little preference for time of day. Climatological studies (Whiteman et al. 1999; Zhong et al. 2001; Whiteman, 2013, personal communication), however, show that PCAPs are most frequently destroyed in the

afternoon. Thus, it is clear that daytime convective mixing is often the final mix-out process that leads to cold-air pool breakup that is often begun by synoptic-scale processes.

## 2.2 Observing and defining PCAPs

This thesis uses data collected from a field project specifically studying PCAP episodes in the Salt Lake Valley. The project is discussed in Chapter 4; however, here we will outline some of the methods used to measure and describe CAPs, which are used later in this research. PCAP field observations have been quite limited up to now because of the difficulty of making wintertime observations and observing relevant features with available observing platforms (Whiteman et al. 2001; Reeves and Stensrud 2009; Gillies et al. 2010). The complexity and scale of the radiative and turbulent interactions within and above a decoupled stable CAP also make them difficult to model (Zängl 2002; Billings et al. 2006; Reeves et al. 2011). Evaluation with numerical models is hindered by known difficulties in developing turbulence parameterizations in stable atmospheres (Zängl 2002; Fernando and Weil 2010).

### 2.2.1 CAP presence and stability

Objective methods can be used to determine the presence of a CAP in a basin and the atmospheric stability within the CAP. Stability can be referred to as CAP strength, though the term 'strength' may also refer to CAP depth or PCAP episode length. A strong CAP takes more energy to convectively mix than a weaker CAP.

A simple method to determine the gross stability within a basin CAP is to measure the potential temperature difference between the basin floor and some fixed level. The chosen level can represent the approximate ridge top of the basin, as a CAP is ideally trapped within the surrounding topography. Figure 2.1 shows time series of basin floor and top potential temperatures from the PCAPS field project, which is introduced later in the thesis. The time series shows diurnal surface temperature variations and warming and cooling episodes aloft, both of which affect potential temperature deficits in the valley. The presence of a potential temperature deficit between two fixed heights does not guarantee the presence of a CAP, however, providing no information on layers of different stability between the measurement points. Stratus clouds, drainage flows, and other microscale processes can create the appearance of a large stable layer in a basin. In the absence of continuous vertical temperature profiles, surface temperature differences between basin floors and nearby peaks can use this method (Whiteman et al. 2001).

A similar metric is used in many climatological studies, where the atmospheric temper-

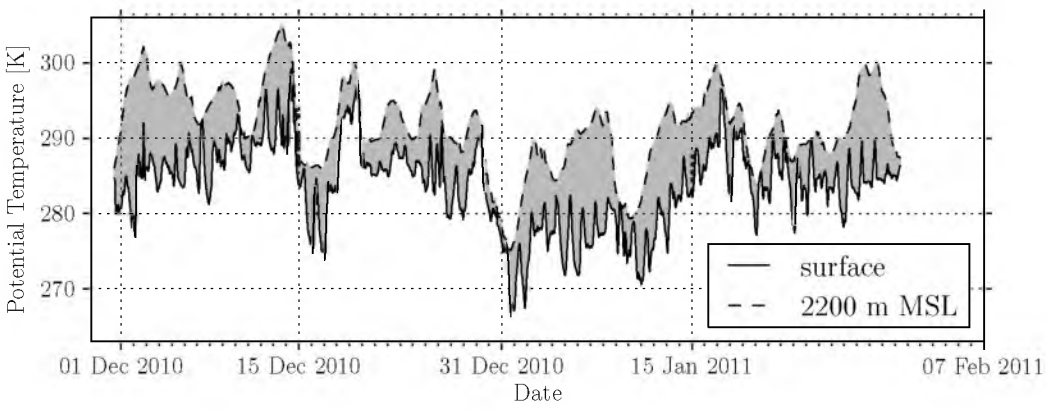


**Figure 2.1**. Time series of potential temperatures from the basin floor (solid line) and basin top (dashed line) from the Salt Lake Valley during the PCAPS field project. The grey shaded area emphasizes the potential temperature differences.

ature lapse rate, as measured by regular soundings, is used as a measure of stable layer presence. Wolyn and McKee (1989) defined a deep stable layer as 65% of the lowest 1.5 km of a sounding having a lapse rate of 2.5 $^{o}$C km$^{-1}$. Such definitions enable climatologies to be computed from regular soundings, where they are available. Reeves and Stensrud (2009) used a similar metric, simply detecting an inversion below the crest of the surrounding mountains. To improve detection accuracy, all of these studies utilized a wind velocity definition (nominally low wind speeds within the CAP layer) in addition to the thermal detection method. Zhong et al. (2011) used only a potential temperature lapse rate definition.

CAP detection via bulk indices can be performed by computation of some value of stability or energy with respect to height up to the top of the basin or some other relevant height. A valley or basin heat deficit is defined as the amount of heat that would have to be put into an atmospheric column to bring it to a constant potential temperature. This could be calculated for a unit vertical air column or the integration could be accomplished for the entire volume of the valley or basin using a volumetric integration of the energy required to raise the temperature of dry air. The formula, from Whiteman et al. (1999), is

$$H_h = c_p \int_0^h \rho(z)[\theta_h - \theta(z)]Adz \qquad \text{[J]} \tag{2.1}$$

where $H$ is the heat required in joules, $\rho$ is the atmospheric density, $h$ is the depth of integration, $\theta_h$ is the potential temperature at the top of the layer, $\theta(z)$ is the vertical potential temperature sounding, and A = 1 m$^2$ is the area of the base of the column. This method assumes that $\theta(z)$ and $\theta_h$ represent the entire valley. Using this definition, CAP strength can be computed at any time when a measurement of $\theta(z)$ is available, and a string of such soundings can be used to observe changes in CAP strength over time. Frequently the basin depth is used as the value of $h$. This integral method better quantifies the depth and stability of the CAP layer, where a thin, strongly stable CAP layer (such as a nocturnal CAP) will require less energy to mix out than a deep and less stable layer, which is more characteristic of a PCAP. To make the integration, a profile of potential temperatures must be available, and an integration depth must be chosen that best captures the stable layer without excessive measurement of the atmosphere above it.

The actual depth of a CAP layer is often difficult to determine and depth definitions are often the subject of debate. One such definition can describe the top of a CAP as the top of the deepest stable layer below the surrounding ridge line. Such a method presents complications when multiple stable layers are present. Unlike a convective boundary layer, inversions may persist over multiple days, creating complex stratification.

The depth of stable boundary layers can be calculated by the parcel method or Richardson number method (Sugiyama and Nasstrom 1999). Significantly more research has been dedicated to determining the depth of convective boundary layers, which usually use methods not physically valid in stable boundary layers (Emeis et al. 2008b).

An alternative definition of stable layering is the energy required to lift a parcel a certain distance, calculated at every height. In this metric, a local minimum occurs at the top of a stable layer, and therefore an absolute minimum should occur at the top of the maximum stable layer.

## 2.3 Cold-air pools in the Salt Lake Valley

This thesis focuses on PCAP evolution within the Salt Lake Valley (SLV) of Northern Utah using data from the Persistent Cold-Air Pool Study of 2010-2011 (Lareau et al. 2013). No major meteorological field experiments focused specifically on persistent wintertime cold-air pools had ever been conducted in this valley or in any other valley in the western United States before this program. The radiosondes that have been routinely launched in the valley over many decades, however, have been used by previous investigators to determine the seasonal strength of temperature inversions in the valley (Wolyn and McKee 1989; Reeves and Stensrud 2009; Zhong et al. 2011). Some aspects of the CAP-relevant meteorology of the Salt Lake Valley are known from previous field investigations, including the DOE-funded Vertical Transport and Mixing Experiment (VTMX) in October 2000 (Doran et al. 2002). VTMX investigations focused on vertical transport and mixing in the valley, through examinations of basin flows and interactions.

The SLV is similar to other locations in exposure to synoptic-scale troughs and ridges that pass across the Intermountain Basin. Utah's Cache Valley (Malek et al. 2006) and the Uintah Basin (Streater 2010), for example, experience similar persistent cold-air pools. Neighboring polluted basins underscore the regional importance for developing an improved understanding of the physics and impacts of PCAP events. This thesis attempts to use novel observational techniques to analyze urban PCAP events for improved description, parameterization, and, ultimately, prediction.

## 2.4 Pollution and human impacts from PCAPs

The societal impacts of PCAPS are significant. They can produce high particulate and chemical pollutant concentrations within the ground-based stable layers and can produce travel impacts from low visibility, fog, and freezing precipitation (Reddy et al. 1995; Whiteman et al. 2001; Silcox et al. 2012).

When PCAPs form in densely populated urban basins, such as Salt Lake City, Utah or Boise, Idaho (Wolyn and McKee 1989) anthropogenic emissions of particulates and chemicals from transportation, heating, and industry will accumulate within the stagnant atmosphere, increasing pollutant concentrations (Reddy et al. 1995; Malek et al. 2006; Silcox et al. 2012). In the Salt Lake Valley, the primary particulate hazard comes from airborne particles less than 2.5 microns in diameter (i.e., $PM_{2.5}$), which are small enough to get lodged in human lungs, causing immediate and long-term health effects (Pope III and Dockery 2006). Rates of emergency room visits for asthma increase 42% in days 5-7 of a persistent CAP in the Salt Lake Valley (Utah Asthma Program 2010). In 2005, the U.S. EPA implemented a National Ambient Air Quality Standard for $PM_{2.5}$ based on human health effects that specified that 24-hour-average concentrations should remain below 35 micrograms per cubic meter. Most areas of Salt Lake County presently exceed the NAAQS more than 10 days per year (Silcox et al. 2012; Utah Department of Public Health 2013; U.S. EPA 2013). States with areas that exceed the ambient air quality standards are obliged to write State Implementation Plans to implement regulations and technologies that will eventually reduce ambient air concentrations to meet these standards. The state of Utah is developing a SIP for $PM_{2.5}$ as this thesis is being written.

Other impacts of PCAPs on the Salt Lake Valley include reduced visibilities from particulate concentrations and fogs, and increased frequencies of fogs, stratus, and freezing precipitation within the PCAPs. When surface temperatures are below freezing and an inversion is present so that there is warmer air aloft, liquid precipitation from clouds above and within the valley can freeze on ground-based objects, leading to icy roadways and runways (Whiteman et al. 2001), severely hampering travel. CAPs also affect sound propagation (Ovenden et al. 2009) within the basin.

The severe societal implications, combined with the lack of direct, focused observations of persistent cold-air pools motivates further investigation into the mechanisms of formation and removal. Improving and understanding the characterization, predictability, and air quality influences from PCAPs is an important goal for improving quality-of-life in the intermountain west.

# CHAPTER 3

# LIDARS

This chapter provides background information on remote sensing of the atmosphere with lidars (LIght Detection and Ranging). The chapter provides a historical context for lidar use in atmospheric sciences, and describes the relevant physics and operating principles. Special emphasis is given to lidar (or laser) ceilometers and their advantages and disadvantages relative to other types of lidars, as analysis using this instrument is the main focus of this thesis. The applications of lidar in atmospheric sciences and, specifically, in complex terrain are discussed through a survey of the literature. The methods used to determine mixing layer heights (MLH) are emphasized, as this has received the most attention from previous investigators. Finally, because this thesis will compare ceilometer observations to those of other remote sensing systems, the operating principles of the other remote sensors are briefly discussed.

## 3.1 History of lidars

An early use of light beams in atmospheric science was the detection of cloud base height, or cloud ceiling, using scanning searchlights (Meissner 1960; Segre and Truscott 1976; Weitkamp 2005). The instrument that measured ceiling heights was referred to as a ceilometer.

Atmospheric ranging and scattering measurements with visible wavelength searchlights have been used for cloud height and atmospheric density measurements since the 1940s (Elterman 1951; Meissner 1960). These applications used triangulation, with side scattering for detection. Pulsed detection methods, based on measuring the delay from a returned signal, were developed in the 1950s. Backscatter lidar developed soon after the development of the laser in the early 1960s (Burch 1963; Collis 1966), and was used to observe small particles (and molecules) in the atmosphere much like radar was used for larger particles (Weitkamp 2005). The evolution of lidar since that time has been to improve frequency, precision, detector sensitivity, resolution, and reduction of costs and maintenance requirements.

## 3.2 Lidar principles and the lidar equation

Lidar uses radiative transfer principles to produce an electromagnetic signal and observe how it interacts with the atmosphere along a path. This is the principle for all lidars. By considering the additional radiation emitted from the atmosphere and the instrument characteristics, the lidar equation can be derived following Weitkamp (2005).

The power received from a scattering event at a distance ($r$) in the atmosphere is a product of the power emitted ($P_0$), an instrument specific coefficient ($K$), a correction for radiative geometric effects ($G(r)$), the scattering coefficient ($\beta(r)$), and the two-way atmospheric transmission along the path ($T(r)$). The influence of background atmospheric emissions ($P_{\mathrm{BG}}$) must also be considered . The lidar equation can thus be written as

$$P(r) = P_0 K G(r) \beta(r) T(r) + P_{\mathrm{BG}} \qquad [\mathrm{W}]. \tag{3.1}$$

This lidar equation has a simple form; however, most of its terms are highly complex. The following paragraphs will discuss the terms in order. The first term ($P_0K$) quantifies the initial energy emitted by the lidar as well as other constant instrument and physical properties and is given by

$$P_0 K = P_0 \frac{c\Delta t}{2} A\eta \qquad [\mathrm{W\ m^3}] \tag{3.2}$$

where $\Delta t$ is the pulse length, and $c$ the speed of light in a vacuum, so that $c \cdot \Delta t$ is the spatial distance of any pulse. Similarly, $P_0 \cdot \Delta t$ is the total energy contained in a pulse. $A$ is the effective area of the receiver optics, $\eta$ is a coefficient representing the total system efficiency for emission and reception. The division by two is a coefficient compensating for the two directions a pulse must travel, which reduces the spatial volume sampled.

The second term ($G(r)$, the geometric effect) assigns how much scattered energy would reach the lidar from a certain point in the atmosphere, disregarding the effects of transmission (extinction).

$$G(r) = \frac{O(r)}{r^2} \qquad [\mathrm{m^{-2}}]. \tag{3.3}$$

The two primary influences are the $r^{-2}$ range correction (produced by the change in energy along a path as the beam spreads) and an empirical function based on the optical characteristics of the lidar, which compensates for transmitter and receiver overlap ($O(r)$). For mathematical stability, $O(r) \to 0$ as $r \to 0$.

The third term is the backscatter coefficient, expressing the portion of incident power that is returned to the lidar. The backscatter coefficient contains all the physics of interactions with scatterers that result in a 180-degree change in photon direction. The scattering coefficient is defined as the differential scattering cross-section per unit solid angle, with

photon direction change $\theta$ at wavelength $\lambda$ ($\sigma_{\text{sca}}(\theta, \lambda)$ [$\text{m}^2$ $\text{sr}^{-1}$]), times the number density ($N$ [$\text{m}^{-3}$]) of scattering particles integrated over all solid angles $\Omega$. Thus, the backscatter coefficient is the scattering coefficient for only a 180-degree angle (i.e., $\theta = \pi$ radians). Thus, the backscatter coefficient is the differential backscattering cross-section times the number of particles illuminated by the incident lidar beam. Considering multiple particle sizes ($j$), this can be written (Weitkamp 2005, eq. 1.5) as

$$\beta(r, \lambda) = \sum_j N_j(r) \frac{d\sigma_{j,\text{sca}}(\pi, \lambda)}{d\Omega} \qquad [\text{m}^{-1}\text{sr}^{-1}] \tag{3.4}$$

where $d\Omega$ represents the area evaluated by integration over observed solid angles. The backscatter coefficient can be linearly combined with the coefficients of scattering in every other scattering angle and absorption to form a total beam extinction coefficient ($\alpha_{\text{ext}}$). Thus, $\beta$ can be interpreted as the fraction of total extinction along a path, which can be expressed as

$$\beta(r, \lambda) = k(r, \lambda)\alpha_{\text{ext}}(r, \lambda) \; [\text{m}^{-1}\text{sr}^{-1}] \tag{3.5}$$

where $k$ is the lidar ratio. Both laboratory and field studies have attempted to quantify lidar ratios for a range of conditions, scatterers, and wavelengths. There have been efforts to develop a database of calculated lidar ratios to allow improved surface and satellite data profiles (Franke et al. 2001). Many of these studies identify values between 0.01 and 0.07 for water haze at wavelengths near 0.7 $\mu$m (Spinhirne et al. 1980). This small range of values has led to the adoption of fixed values for analytical applications (Rogers et al. 1997; Vaisala 2004).

Bissonnette (1996) and Franke et al. (2001) described situations where the lidar ratio changed substantially with height, while remaining within these ranges. For this reason, especially when analyzing aerosols, a fixed lidar ratio cannot be assumed. While particles in the atmosphere are often 1-100 $\mu$m in diameter, scattering for wavelengths near 1 $\mu$m is in the far more complex Mie region (see Figure 3.1). This means that even understanding the size distribution will be very complex, as Mie scattering is highly variable.

One last topic of importance for the backscatter coefficient is the influence of molecular versus particulate scattering. Rayleigh or molecular scattering (and some Mie scattering at UV wavelengths) causes backscattering that adds to the backscatter from particles. Thus, it is reasonable to split the backscatter coefficient into two terms, which add linearly. This is more technically accurate and allows the molecular component to be omitted when appropriate for some specialized lidars (Emeis 2011).

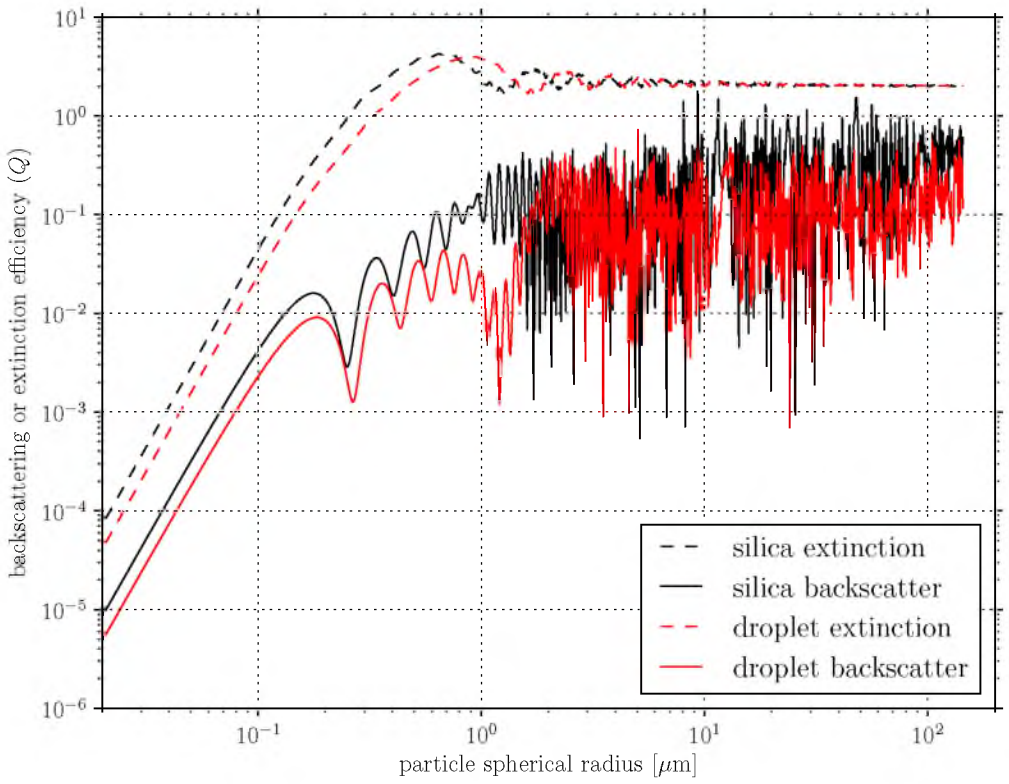


**Figure 3.1**. Sample calculations for scattering efficiencies (proportional to cross-sections, $\sigma$, not coefficients $\beta$, $\alpha$). Though not directly derived from this, the lidar ratio is related to the ratio of backscatter to extinction lines. For particles of $10^0$ to $10^2$ $\mu$m in diameter (as most airborne particulates are) this ratio will be variable. Computations were made with a software package called MiePlot (`http://www.philiplaven.com/mieplot.htm`)

The final term of the lidar equation addresses extinction, and is an expression of how much energy will be lost to the atmosphere along the light's two-way path. The transmission term can vary between 0 and 1, where 0 means none of the transmitted energy will complete the journey, and 1 meaning all energy will complete the journey. Thus, the transmission coefficient is the ratio of the received radiation ($I_r$) to the emitted radiation ($I_0$) via Beers law. Emitted radiation that is not backscattered is lost and thus not considered. Disregarding geometric ($r^{-2}$) effects, the ratio of the energy scattered downwards to the energy received can be written as

$$T_{\text{one-way}} = \frac{I_r}{I_0} = \exp\left[-\int_0^r \alpha(r,\lambda)dr\right] = \exp[-\tau(r,\lambda)] \qquad \text{[unitless]}. \tag{3.6}$$

This is the one-way attenuation caused by irradiance passing through an atmosphere with a varying extinction coefficient alpha. For simplicity, the far right-hand version of the equation uses optical depth $\tau$. Because attenuation occurs on both the up and down pathways, the two-way transmission would be

$$T_{\text{two-way}} = T^2_{\text{one-way}} = \exp\left[-2\int_0^r \alpha(r,\lambda)dr\right] = \exp[-2\tau(r,\lambda)] \qquad \text{[unitless]}. \tag{3.7}$$

The two in the exponent considers both directions of travel, assuming a plane-parallel (and stationary for the moment of transmission) atmosphere. The extinction coefficient is similar to the backscatter coefficient, in that it is the product of extinction cross-section and the number concentration of particles with that cross-section. Sources of extinction are both absorption and scattering for either molecules or particles. Thus there are four possible constituents to the extinction coefficient.

Following this discussion of individual equation terms, the lidar equation for a single wavelength lidar can be written as

$$P(r) = P_0 \frac{c\Delta t}{2} A\eta \frac{O(r)}{r^2}\beta(r)\exp\Big(-2\tau(r)\Big) + P_{\text{BG}} \qquad \text{[W]}. \tag{3.8}$$

This equation describes the physics that determines how much energy is backscattered to the receiver from an initial emitted pulse $P_0$ at a range-resolved point in time. Coefficients and terms contain physical and statistical wave-particle interactions, which are undetermined when considered independently (e.g., scattering and extinction). Different types of lidar use this equation to make qualitative or quantitative analyses of the atmosphere.

The instrument characteristics (efficiency $\eta$, for example) can be combined into a single instrument coefficient $C(r)$. Thus, the lidar equation can be written as

$$P(r) = \frac{C(r)}{r^2}\beta(r)T(r) + P_{\text{BG}} \qquad \text{[W]} \tag{3.9}$$

where

$$C(r) = \frac{P(r)r^2}{\beta(r)T(r)} \qquad [\text{m sr}^{-1}]. \tag{3.10}$$

With this, the lidar equation is governed by three terms, the instrument coefficient, the backscatter coefficient, and atmospheric transmission. If the instrument coefficient is known, the resulting measurement is considered calibrated, meaning the attenuated backscatter coefficient is directly derived from atmospheric particle conditions. A lidar can be calibrated using molecular (rayleigh-based) backscattering. By combining information about the density of atmospheric molecules, the measured backscatter coefficient can be directly compared to its known value (predicted from atmospheric density measurements) and a calibration offset can be determined via eq. 3.10 (Reagan et al. 2002). Alternatively, if the atmospheric optical depth is known and aerosols measured by the lidar form the majority of this optical depth and the instrument coefficient is considered constant with height, a calibrated $\beta$ profile can be derived. This is done by iteratively solving for the instrument coefficient such that the integral of the calibrated $\beta$ profile equals the measured atmospheric optical depth (Weitkamp 2005). The relationship between an uncalibrated lidar backscatter profile and measured particulate sizes and concentrations is expected to change over time due to variable, unquantified instrument characteristics.

One important use of lidar is in the measurement of particle motion using the Doppler effect. This is distinctly different from optical information in the lidar equation, and will be described briefly here. Doppler lidar usually uses coherent (heterodyne) detection where the known frequency-emitting laser is combined with a known local oscillator (LO) laser to determine the frequency shift. The LO is offset a fixed amount from the emitted signal. The Doppler-shifted return signal is optically merged with the LO signal, and the resulting beat frequency is measured (Grund et al. 2001; Emeis 2011). Velocities along the beam direction can be computed from Doppler shifts and different scanning patterns can be used to measure atmospheric winds.

## 3.3 Lidar ceilometers

A laser or lidar ceilometer is an elastic backscatter lidar that produces height estimates of cloud bases by sensing the presence of cloud particles via their strong backscattering cross-section. The operational goals of a ceilometer are quick, accurate cloud base height detection with low maintenance requirements (Münkel et al. 2007). Sensitivity and spectral precision are secondary considerations that would be expensive to incorporate and would make a ceilometer more difficult to maintain. For this thesis, a Vaisala CL-31 lidar ceilometer will

be used to examine boundary layer structure. These simple elastic backscatter lidars have important limitations that can be discussed in terms of the lidar equation in section 3.2.

The emitted power, lidar efficiency, and source function terms in the lidar equation (eq. 3.8) are assumed to be constants that are predetermined for the life of the ceilometer, making all measurements uncalibrated. A ceilometer also does not make any attempt to quantify atmospheric transmission, because this is impractical without using multiple frequencies or high spectral resolution. Therefore, the effects of transmission and backscattering coefficients in the lidar equation are combined into an attenuated backscatter coefficient ($\beta_a$), limiting practical quantitative analysis (Rogers et al. 1997; Münkel et al. 2007).

$$\beta_a(r) = \beta(r)T^2(r) \qquad [\mathrm{m}^{-1}\mathrm{sr}^{-1}] \tag{3.11}$$

Two environments where an analysis can be made are those where gross assumptions are reasonable. The first such environment is a particle-free convective boundary layer where until a cloud is reached, attenuation can be assumed to be zero (Münkel et al. 2007). A second environment is precipitation, where with full attenuation and approximated scatterer size distributions, extinction coefficients can be estimated via integration (Rogers et al. 1997; Weitkamp 2005). A polluted CAP environment fulfills neither of these conditions.

In a CAP, especially within an urban environment, particles will both backscatter strongly and attenuate the signal non-negligibly. Were a ceilometer to be oriented horizontally, it is possible that full attenuation would be observed, and integrative measurements of extinction could be evaluated. However, vertically oriented lidars in CAP environments will have an attenuating path length of less than 2 km (before emerging into the relatively low-attenuation free atmosphere), and therefore are unlikely to be entirely attenuated by a shallow CAP layer. This is analogous to an observer still viewing blue sky above his position in a polluted CAP valley, though he may not be able to see the sidewalls.

It is possible to use surface-derived transmission measurements (often in the form of visibility) to approximate vertical extinction (or, with full attenuation, to use extinction to approximate visibility; Weitkamp 2005). Much like using a surface-derived particle backscatter-extinction ratio (the lidar ratio), different particle concentrations and compositions vertically cause large variability in attenuation values with height. Therefore, any improved precision of an analysis using this information will be undermined by a loss of accuracy.

Additional limitations to quantitatively analyzing ceilometer data are the imprecise nature of the emitter frequency (Vaisala 2004), and complex calibration coefficients, which

are not carefully monitored (Rogers et al. 1997). Research continues into improved understanding and application of quantitative analysis methods represented by research papers by Münkel et al. (2004, 2007) and Van der Kamp (2008).

As noted, this work intends to extend this body of research into complex terrain persistent cold-air pool studies. Our field-study-based datasets will be used to demonstrate the usefulness of less expensive ceilometers for gaining a better understanding of complex terrain boundary layers.

## 3.4 Lidar research and applications

This section will summarize published meteorological research relevant to this thesis that has been accomplished using lidars. First, we will describe the methods that have been used to determine boundary layer depths. This will be followed by a review of lidar investigations of meteorology in complex terrain.

### 3.4.1 Measuring boundary layer/mixing layer depth with lidar

Particulate densities are generally higher within the portion of the atmosphere in direct interaction with the Earth's surface, the atmospheric boundary layer or ABL (Stull 1988; Piironen and Eloranta 1995; Seibert et al. 2000; Emeis et al. 2011). Lidar is an ideal platform for measuring boundary layer depth and dynamics using particulate scatterers (Emeis et al. 2008b).

This thesis focuses on persistent stable boundary layers, while most of the published lidar research has investigated convective boundary layers over simple terrain (e.g., Kunkel et al. 1977; White et al. 1999; Cohn and Angevine 2000; Davis et al. 2000; Haeffelin et al. 2011; Haman et al. 2012) and over the ocean (e.g., Melfi et al. 1985; Porter et al. 2003; Sicard et al. 2006). Lidar, however, is a research tool having the spatial resolution to make important contributions to the understanding of complex atmospheric motions (e.g., Banta et al. 2004; Pinto et al. 2006; Price et al. 2011).

Particle backscatter is often a secondary interest to those studying the dynamics of boundary layer flows. Airborne and high-resolution Doppler lidars have been used in these dynamical studies. See, for example, Grund et al. (2001), Banta et al. (2004), Weissmann et al. (2005), or Godwin et al. (2012).

Modern advanced profiling lidars do not require significant space or energy to make observations. Because of this, lidars are popular instrumentation for deployment on aircraft. Airborne lidars can measure winds, particulates, boundary layer structure, and air chemistry (Antokhin et al. 2012; De Wekker et al. 2012). Lidars are also used in space, where the

A-train constellation of earth orbiting satellites includes the CALIPSO satellite, which possesses a two-channel polarized lidar for examining atmospheric aerosol profiles, cirrus clouds, and fine structure at the top of convective plumes (Hunt et al. 2009; Vaughan et al. 2009).

Satellite research into complex terrain boundary layer structures is limited for a combination of technical reasons. Spaceborne lidars have been able to observe complex terrain cold-air pooling. Brun et al. (2011) shows CALIPSO lidar cross-sections of an aerosol laden CAP in the Himalayas (in the context of desert dust advection). This research is rare, and difficult for smaller basins because polar orbiting lidars have small observation footprints and return to within ± 20 km of the same point only every 16 days, with gaps of hundreds of km between effective 70 m lidar swaths (Stephens et al. 2002; Winker et al. 2003).

### 3.4.2 Objective methods of determining MLH

The optical profile of the atmospheric boundary layer is visually similar across most particulate-laden boundary layer types. For this reason, it is possible to develop routines to analyze backscatter profiles to objectively determine boundary layer characteristics (Emeis et al. 2008b). Most of these methods do not require calibrated backscatter observations, in that the magnitudes of the analyzed variable need only correspond to the relative density of particulates. As a result, any boundary layer can be analyzed where a lower layer contains higher backscatter than the free atmosphere above.

There are multiple methods that can be applied to optical backscatter data to quantify the depths of the atmospheric boundary layers, mixing layers, or aerosol layers. The methods used can be categorized as: threshold, gradient, inflection point, idealized profile, and variance. These five basic methods will be discussed in this section.

#### 3.4.2.1 Threshold method

The threshold method is the simplest analytical technique for determining mixing layer depth. It was first described by Melfi et al. (1985). To determine the boundary layer depth, subjective backscatter values for both the polluted boundary layer and the clear atmosphere are defined. A threshold is then determined where, when backscatter decreases below such a value, the atmosphere is considered clear. This is synonymous with creating an isopleth of the threshold value in the backscatter profile. This method is illustrated in Figure 3.2.

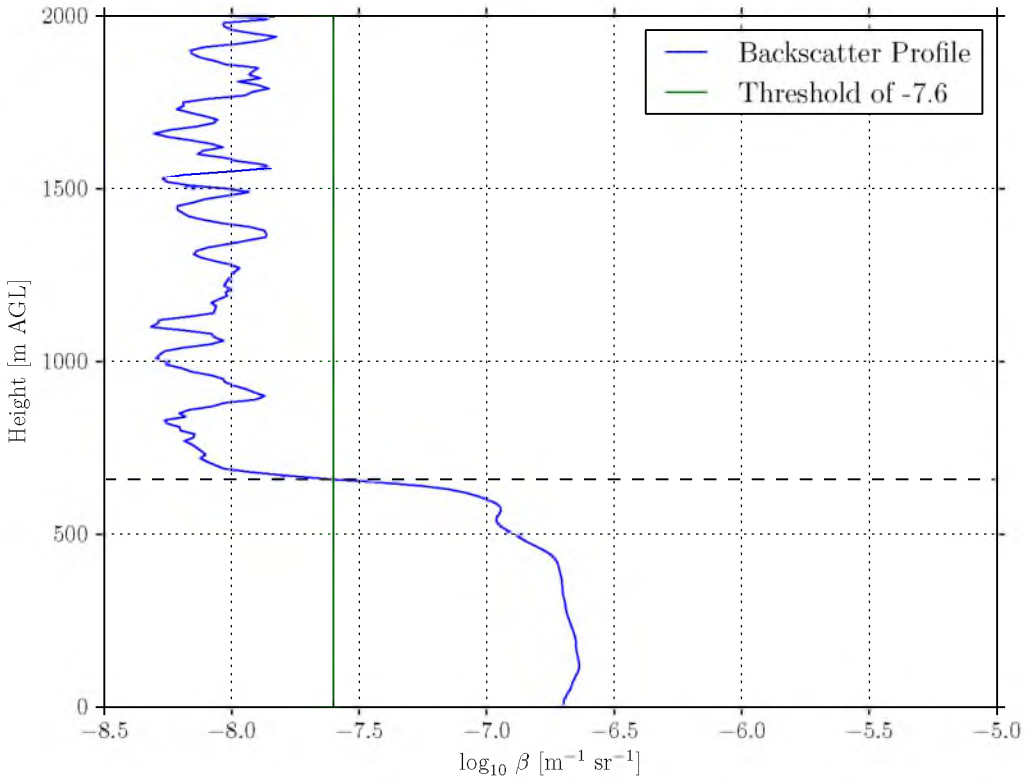


**Figure 3.2**. Illustration of the threshold method. Here a threshold $\log_{10}$ backscatter coefficient ($\beta$) value of -7.6 $m^{-1}$ $sr^{-1}$ results in an aerosol layer depth of 620 m AGL.

#### 3.4.2.2 Gradient method

The most popular method for determining mixing depth is the gradient method, proposed by Hayden et al. (1997) and Emeis et al. (2008b). In this method, the height of the maximum negative gradient of backscatter is considered to be the depth of the mixing layer. This method is illustrated in Figure 3.3. Mathematically this is written as

$$h_{\mathrm{GM}} = \min[G(z)], \text{ where } G(z) = \frac{\partial \beta}{\partial z} \tag{3.12}$$

A gradient profile $G$ is evaluated to find $h_{\mathrm{GM}}$ where the above criteria are met. This can be used to define one maximum gradient point, or it can be used to identify all local maxima in decreasing aerosol content, allowing the detection of the depth of a surface-based layer and the depths of elevated aerosol layers, identifying processes occurring vertically (Emeis et al. 2007, 2008a).

#### 3.4.2.3 Inflection point method

The inflection point method uses the second derivative of backscatter with respect to height to detect the height where backscatter begins to decrease. This is shown in Figure 3.4, and is described by Menut et al. (1999). Mathematically this is written as:

$$h_{\mathrm{IPM}} = \min[R(z)], \text{ where } R(z) = \frac{\partial^2 \beta}{\partial z^2} \tag{3.13}$$

The profile $R$ is evaluated for a minimum value to find $h_{\mathrm{IPM}}$. This method, in our application, has difficulty compensating for instrument noise. Sicard et al. (2006) has found that this method, which generally picks a lower height value than the gradient method (as seen in Figure 3.4), is also generally more in agreement with gradient Richardson number-based MLH values derived from radiosonde data.

#### 3.4.2.4 Idealized profile method

Steyn et al. (1999) proposed that a simple function could be fit to the backscatter profile to characterize both the mixing layer depth and entrainment strength. The function, which is a vertical application of the error function, is fit by minimizing the mean-squared error (MSE) between it and the backscatter profile. The mathematical function for this method in the form of Eresmaa et al. (2005) is

$$B(z) = \frac{B_m + B_u}{2} - \frac{B_m - B_u}{2} \mathrm{erf}\left(\frac{z-h}{\Delta h}\right) \tag{3.14}$$

A backscatter profile $B$ is a function of mixing layer backscatter ($B_m$), the free atmosphere backscatter ($B_u$), the height of the mixing layer ($h$), and the entrainment thickness

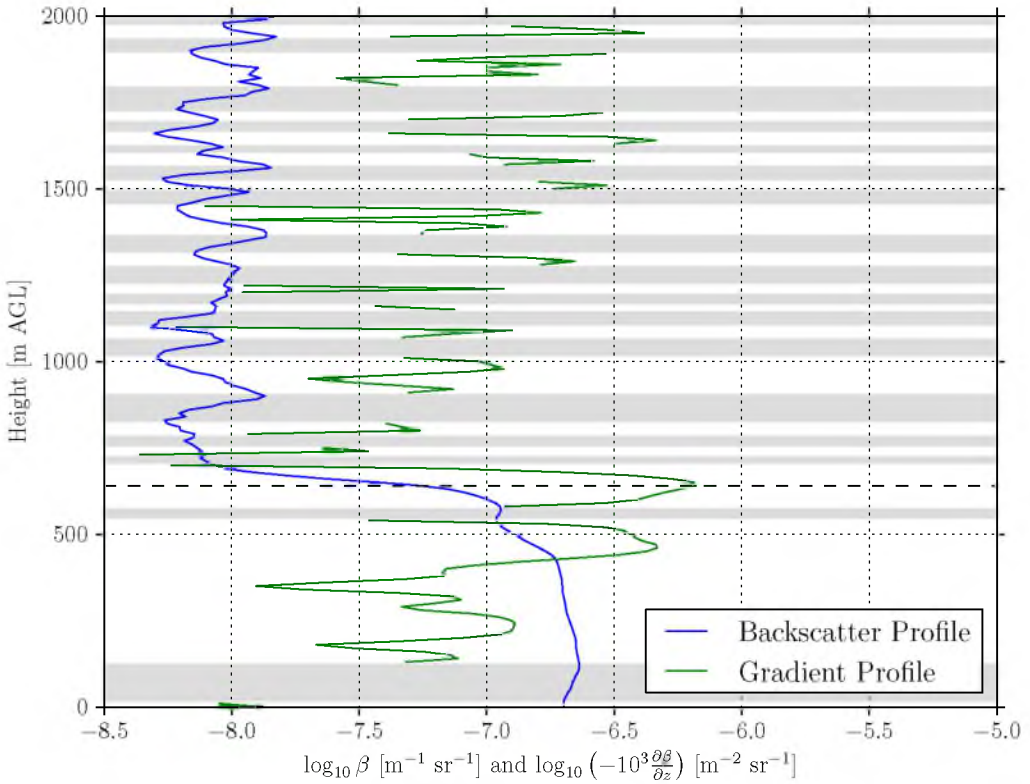


**Figure 3.3**. Illustration of the gradient method for aerosol layer detection and characterization. The $\log_{10}$ backscatter coefficient ($\beta$) profile is shown in blue, with the $\log_{10}$ of the negative scaled backscatter gradient ($G$ in eq. 3.12) shown in green. The periods of zero or positive gradient are shaded in grey. The black dashed line indicates the maximum negative gradient, which is assumed to be the top of the aerosol layer. An alternative application of the method detects *all* local minima in the field.

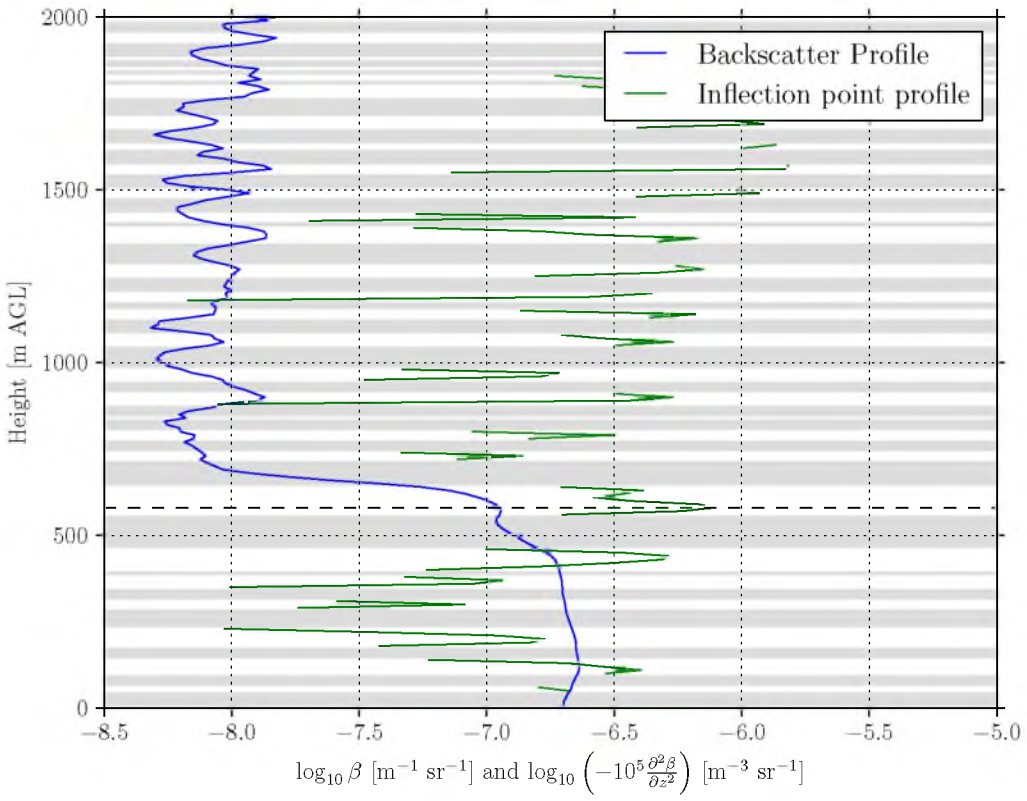


**Figure 3.4**. Illustration of the inflection point method for aerosol layer detection and characterization. The $\log_{10}$ backscatter coefficient ($\beta$) profile is shown in blue, with the $\log_{10}$ of the negative scaled second derivative with respect to height of the backscatter coefficient ($R$ in eq. 3.13) shown in green. The periods of zero or positive $\partial^2\beta/\partial z^2$ are shaded in grey. The black dashed line indicates the maximum negative value of $R$, which is an approximation of the top of the aerosol layer.

($\Delta h$). This function produces a sloped shift from a high concentration in the boundary layer to a lower clear air concentration (Figure 3.5). Iteration is used to determine $h$ and $\Delta h$, but $B_m$ and $B_u$ are assessed by other means. Different implementations of the method use different first guesses, which we will investigate in the results section. In this method, a homogeneous boundary layer is assumed, and information is lost pertaining to nonideal vertical structure within an aerosol layer.

Eresmaa et al. (2012) describes an improvement to the idealized profile method that allows for the detection of three distinct mixing heights. This modification requires more computation, and works on the premise that backscatter concentrations decrease monotonically. Because backscatter concentrations generally do not decrease monotonically during PCAPS, we have not investigated this modification further.

#### 3.4.2.5 Variance method

The final method that we have evaluated uses the temporal or spatial variance in backscatter at the top of the ABL. This method assumes that the backscatter density near the top of the ABL (at some fixed altitude) will change from polluted to clean frequently. Piironen and Eloranta (1995) showed that the CBL top height and associated aerosol concentrations undergo fluctuations. Menut et al. (1999) have suggested a modification to this technique using a variance centroid.

This list of methods to determine mixed layer heights is not exhaustive. Additional methods are discussed in individual papers, such as Menut et al. (1999), Haij et al. (2007), and others. These methods, however, are almost exclusively developed for determining the depths of convective boundary layers over relatively flat terrain. Our application focuses on stable boundary layers rather than convective layers, and the utility of the methods can be expected to differ from that of convective boundary layers.

### 3.4.3 MLH research with ceilometers

The novelty of the work in this thesis is the application of lidar boundary layer analysis to ceilometers in complex-terrain CAP environments. The ceilometer has found wide application in MLH detection for convective boundary layers and nocturnal residual layers (e.g., Emeis et al. 2007; Haij et al. 2007; Münkel and Roininen 2010; Emeis et al. 2011; Eresmaa et al. 2012). The advantages provided by ceilometers are long-term observations and widespread use, allowing seasonal and multilocation studies (Emeis et al. 2008a; Van der Kamp 2008; Muñoz and Undurraga 2010).

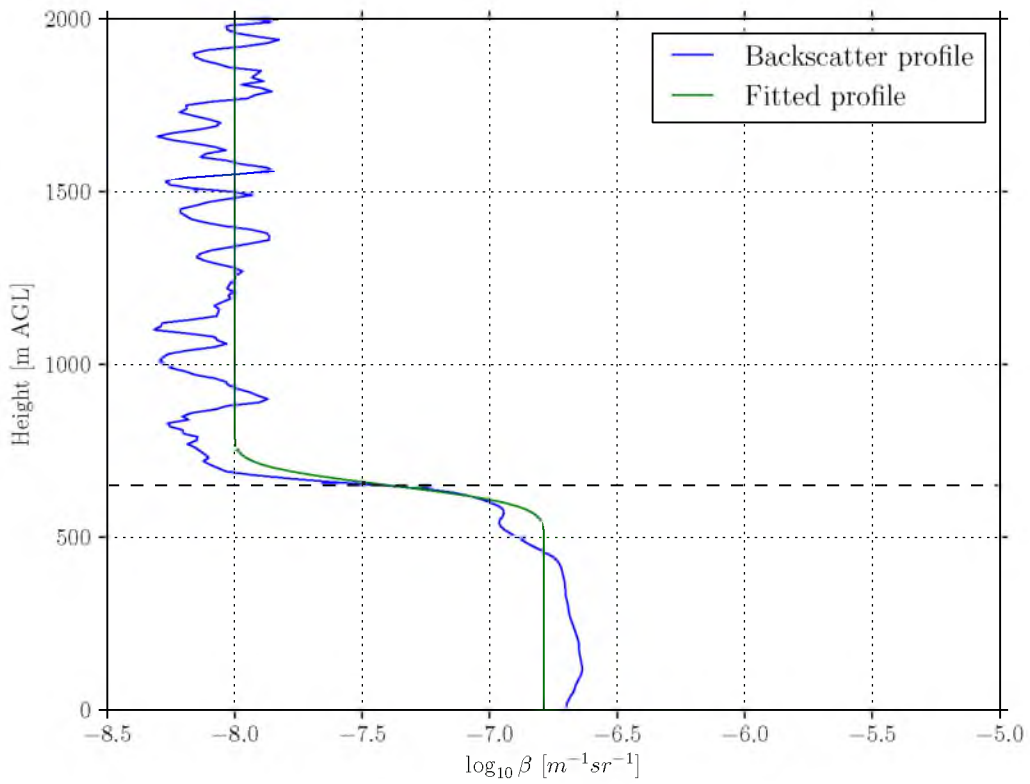


**Figure 3.5**. Illustration of an idealized profile function (green curve) fitted to the blue backscatter profile. By minimizing the mean square error (MSE) between the two profiles an aerosol layer depth (dashed black line) and an entrainment layer depth can be determined. A first guess for aerosol depth in this method is based on the threshold method.

All of the optical MLH analysis methods discussed previously have been applied to ceilometer backscatter (Eresmaa et al. 2005; Weitkamp 2005; Emeis et al. 2008a). Numerical analyses of ceilometer data, with the intention of determining particulate extinction, continue to be investigated in studies by Rogers et al. (1997), Shephard (1998), Markowicz et al. (2008), among others.

National-level synoptic and mesoscale networks of ceilometers recording full backscatter information have been established in Europe (Haeffelin et al. 2011), facilitating an expanding scope of research into operational applications of ceilometer data (Seibert et al. 2000; Haij et al. 2007). Long-term boundary layer and pollution-based studies have also used ceilometer data because of its relatively low cost (e.g., Münkel et al. 2004; Di Giuseppe et al. 2012; Haman et al. 2012). Studies have also compared ceilometer boundary layer characterization data with that of other more expensive and/or demanding remote sensing technologies (Emeis et al. 2004, 2009; McKendry et al. 2009; Arend et al. 2010; Heese et al. 2010).

## 3.5 Complex terrain studies with lidar

The high temporal and spatial resolution of lidars make them particularly valuable for the study of complex terrain meteorological phenomena. The lidars used for these studies are primarily Doppler and aerosol lidars (Banta et al. 2004; Weissmann et al. 2005; Hill et al. 2010).

The Atmospheric Studies in Complex Terrain (ASCOT) study in a narrow Colorado valley in 1984 was among the first to use a scanning Doppler infrared lidar to examine flow systems within a narrow valley. The lidar observed katabatic and anabatic flow structure, with especially detailed observations of the transition from downvalley flow to upvalley flow (Post and Neff 1986). Doppler lidar was also used to observe canyon flow reversals in Arizona's Grand Canyon caused by strong ambient winds (Banta et al. 1999). It was also used to observe weaker thermally forced flows within the canyon, and proved useful in characterizing the aerosols and mixing within these environments.

The Vertical Transport and Mixing eXperiment (VTMX) used both aerosol and Doppler lidars to examine transport and mixing in the Salt Lake Valley during both daytime and nighttime during the fall 2000 experimental period (Doran et al. 2002). Lidar backscatter was used to observe waves at the top of a stable boundary layer (Cooper et al. 2006) and to verify a complex terrain dynamic model (Fast and Darby 2004). The Terrain-induced Rotor Experiment (T-REX) used a combination of scanning Doppler and aerosol lidars (Grubišić et al. 2008). Descriptions of flow convergence and convection (both from Doppler

measurements and by visualizing particle transport with an aerosol lidar) were used in conjunction with radar datasets to describe the circulations in the Owens Valley.

## 3.6 Other remote sensing systems

The research for this thesis compares ceilometer data with data obtained with other remote sensing systems. The operating principles of these systems will be discussed below, but in less detail than for lidars since they are not the focus of this work. Also, information is available from other sources. For radar wind profilers see Cohn and Angevine (2000) and for RASS see Emeis et al. (2004), among others. The reader is referred to textbooks such as Emeis (2011) for more information on these technologies.

### 3.6.1 Radar wind profilers

The Radar Wind Profiler (RWP) uses electromagnetic waves of longer wavelengths than lidar to profile air motions and turbulence. Profilers can be varied in antenna/emitter size, frequency, power, orientation, and detection theory. For that reason, and because the interactions between the atmosphere and larger radar waves can be very complex, this section will provide only a brief summary of RWP technology.

RWPs were deployed in PCAPS as part of the NCAR Integrated Sounding System (Parsons et al. 1994). Two different types of radar were used, one that computes winds based on Doppler beam swinging (DBS), which uses velocities in the path of three or more angled profiles to compute horizontal winds and a second called a multiple antenna profiler radar (MAPR), which uses spaced antenna measurement techniques to determine horizontal atmospheric motions (Cohn et al. 1997, 2001, 2011; Brown et al. 2011). Though mostly used for wind profiles, convective boundary layer depths can be identified from SNR or backscattered power data from these wind profilers (White et al. 1999; Heinselman et al. 2009).

The DBS-based RWP operated at 915 MHz and provided clear air measurements of Doppler shifts and backscattered power from atmospheric turbulence structures via Bragg scattering (Emeis 2011). Wind vector computations from along-beam Doppler velocities are vulnerable to electromagnetic noise and side-lobe influences. For this reason, data are analyzed with an analytical image processing moment estimator called the NCAR Improved Moments Algorithm, described by Morse et al. (2002).

The MAPR uses a technique described by Cohn et al. (1997, 2001) where a single directional signal is emitted by all antennas (3 antennas in PCAPS), and the difference in returned signal from several spaced antennas is used to compute horizontal motions at

different range gates. By using a single vertical signal, this radar system probes a very small sampling volume when profiling the atmosphere. Since spatial homogeneity is not assumed, temporal averaging like that required for a full RWP is not needed. Therefore, this instrument can be operated with higher temporal resolution, on the order of 30 seconds, versus 30 minutes for a DBS RWP (Brown et al. 2011).

This system requires a robust signal to be received by all antennas. For this, the atmosphere must have a higher signal to noise ratio (SNR) than that required for DBS measurements (Cohn et al. 2001). Fuzzy logic and image processing techniques are performed on these data to remove biological and ground clutter from the output. A different processing method is used to compute wind velocities, known as full correlation analysis (Cohn et al. 1997).

### 3.6.2 Radio acoustic sounding system

Radio Acoustic Sounding Systems (RASS) combine radar wind profilers with sonic pulses to measure temperatures in the atmosphere. Acoustic waves are emitted into the atmosphere with twice the wavelength of the radar. These waves in the atmosphere will efficiently backscatter the radar's emissions when their frequency meets the Bragg condition $\lambda_e = 2\lambda_a$, where subscript $e$ represents radar, and subscript $a$ represents the acoustic wave front (Emeis 2011). Because electromagnetic waves travel much faster than sound, the propagating sonic wave front can be traced as it travels through the atmosphere. The speed of sound is a function of virtual temperature, allowing the computation of virtual temperature profiles.

RASS is limited by the distance the sonic wave can be detected, and by wind advecting the sonic wave out of the radar's field of view. As well, vertical motion in the atmosphere will change the measured speed of sound, which must be corrected for (Moran and Strauch 1994). Additional errors from wave detection and other radar principles make the data produced difficult to use for detailed research.

The previously discussed remote sensing platforms make volume-averaged measurements. This means that measurements contain errors caused by atmospheric inhomogeneities in the sampling volume. While radar and lidar methods have pulse repetition frequencies in the thousands per second, sonic methods require delays of up to several seconds in order to sample a full atmospheric volume. Fewer samples increase the effects of background noise.

Additional limitations and sources of error exist for each remote sensing platform. Many of these are addressed either through quality assurance processes, or through insightful analysis techniques, which consider the limitations when interpreting the data. Research

like that in this thesis is ongoing to increase the number of applications and the accuracies of remote sensing systems, whether surface-, aircraft-, or space-based (Parsons et al. 1994; Emeis 2011).

# CHAPTER 4

# FIELD OBSERVATIONS

This chapter describes the field observations of cold-air pools that are used in this thesis. This chapter outlines the NSF-funded Persistent Cold-Air Pool Study (PCAPS) by discussing the environment, goals, and resources used to study PCAP events. An emphasis is placed on the surface and remote sensing observations that are used to describe the atmosphere within a PCAP event.

## 4.1 The Persistent Cold-Air Pool Study

The Persistent Cold-Air Pool Study (PCAPS) was an NSF-funded, multi-investigator field observation and modeling experiment investigating persistent wintertime stable layers that form in valleys and basins. The field portion of the study was conducted from 1 December 2010 to 7 February 2011 in the Salt Lake Valley (SLV) of Northern Utah. The major participating organizations included the University of Utah (UU) Atmospheric Sciences department, the National Center for Atmospheric Research Earth Observing Laboratory (NCAR/EOL), and Michigan State University (MSU). The goals of the study were to observe the lifecycle of persistent multiday cold-air pool (CAP) events in the SLV, and to investigate the atmospheric processes that occur within the CAPs. A paper by Lareau et al. (2013) provides an overview of PCAPS, including some initial findings.

PCAPS is one of a few field programs that have specifically studied PCAP events. Other cool-season studies in the Salt Lake Valley and elsewhere have made or used observations from within CAPs, often while investigating other meteorological processes (e.g., Whiteman et al. 2001; Doran et al. 2002; Clements et al. 2003; Whiteman et al. 2008). The experimental design and observational studies were developed with the goal of documenting meteorological processes related to formation, maintenance, and removal of PCAPs from the basin.

Analyses of datasets collected for PCAPS are being used to develop a better understanding of PCAP processes. Datasets are also being supplied to test the simulations of

cold-air pool processes using numerical models. This thesis does not include modeling, but instead focuses on analyses.

## 4.2 Study environment

The SLV environment is well suited for the study of the lifecycle of CAPs and the increased pollutant and particulate concentrations that build up within these events due to the large number of urban pollutant sources. Previous experience and research for the SLV suggests numerous CAP events occur between December and February (Wolyn and McKee 1989), when the surface energy balance is negative due to reduced wintertime insolation and the frequent presence of wintertime cloud and snow cover. CAPs occur frequently in mid-to-high-latitude basins during the cold season when daytime surface heating is insufficient to convectively mix the cold, dense air with the warmer atmosphere above (Whiteman et al. 2001).

The SLV (Figure 4.1 (b)) is blocked on two sides by the Wasatch mountains to the east ( 3000 m MSL) and the Oquirrh mountains to the west ( 2500 m MSL). The high mountain barriers on the east and west reduce insolation at the valley surface via shadowing, and cooling can be exacerbated by drainage from multiple east-west oriented canyons in the Wasatch Mountains. The south end of the valley is obstructed by the Traverse Ridge, which has a gap that allows flow to pass between the the Utah Valley to the south and the Salt Lake Valley. The SLV is open to the northwest, where it is bounded by the Great Salt Lake.

Pollution in the SLV is the primary motivation for increasing understanding and predictability of these events. In the SLV, 24-hour mean concentrations of aerosol particulates less than 2.5 microns in diameter ($PM_{2.5}$) frequently exceed the National Ambient Air Quality Standard (NAAQS) of 35 $\mu$g m$^{-3}$ during CAP events (Silcox et al. 2012). Extreme particulate concentrations can exacerbate medical conditions and reduce visibilities, making exercise and travel potentially hazardous. With increased understanding of PCAP evolution, population habits in energy consumption and transportation could be modified to mitigate the pollution buildup within the stable layer.

The weather during the 2010-2011 PCAPS field experiment was somewhat unusual in that clouds and precipitation were present more frequently than expected climatologically. Thus, there were no full PCAP events without the complicating influence of clouds during any of the 10 IOP events that were observed in this winter (Lareau et al. 2013). This presented analysis and modeling challenges as clouds and precipitation are difficult to observe accurately and to simulate numerically.

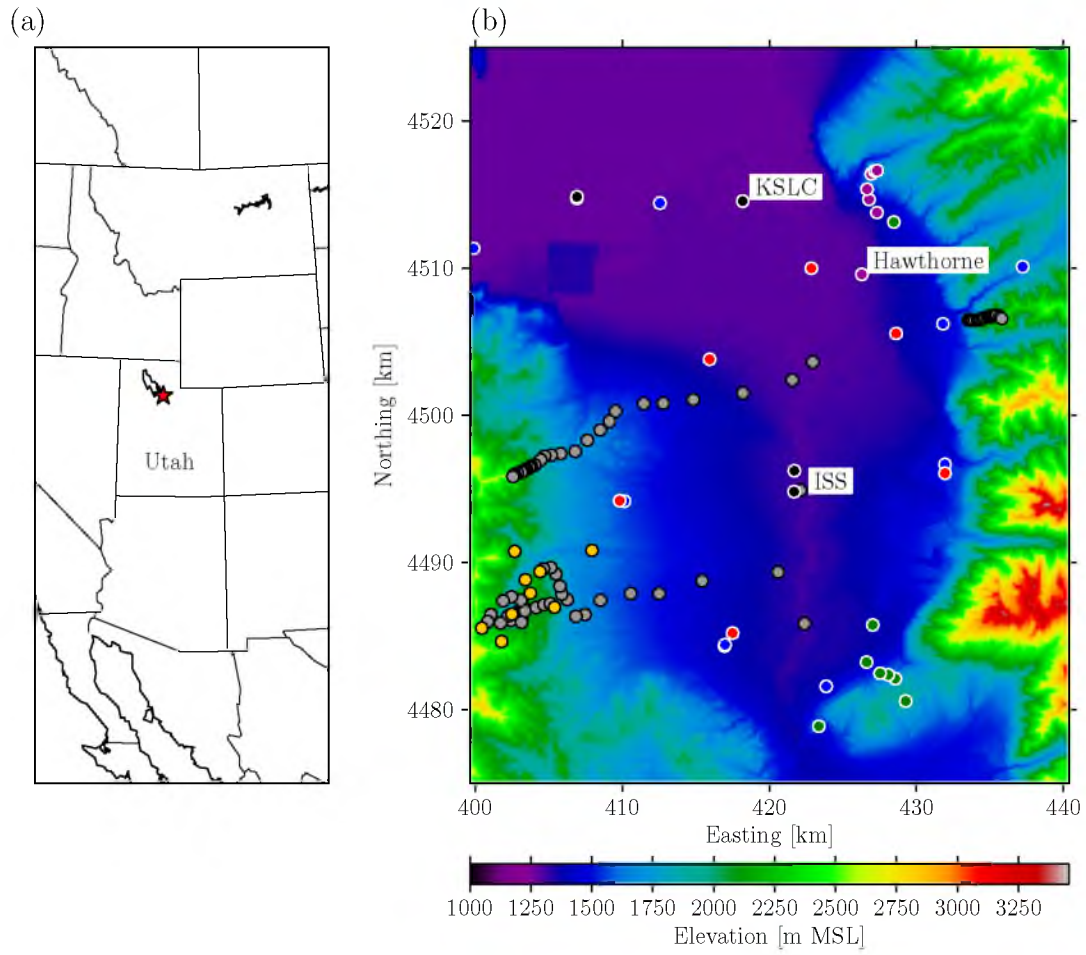


**Figure 4.1**. A depiction of the PCAPS study environment. (a) Utah's Salt Lake Valley (indicated by the star), and (b) SLV elevation and instrumentation locations for the PCAPS field program held in the SLV from 1 December 2010 to 7 February 2011. Instrument sites on the map include NCAR ISFS surface flux stations (red), HOBO temperature dataloggers (gray), Graw radiosonde and glider launch sites (blue), air quality sites (UU and Utah Division of Air Quality; purple), UU surface observing stations (green), Bingham Canyon Mine automatic weather stations (yellow). NCAR profilers were located at the ISS 2 (south, ceilometer location) and ISS 3 (north, location of RWP and RASS) identified on the map as 'ISS'. Radiosondes were launched from the Salt Lake Airport (KSLC) and from the NCAR ISS 2 site. The UU sodar was located in the northwest portion of the map (black dot) collocated with an ISFS surface station.

## 4.3 Experiment design

The experiments were designed to capture meteorological observations during PCAP events, through continuous surface and profiler observations, with special supplemental radiosoundings and mobile surface transects. Continuous observing platforms were either pre-existing (the MesoWest network and NWS radiosoundings), or were installed to maximize information for particular phases of the PCAPs. PIs and the graduate leadership of the project jointly made decisions during the pre-experiment planning stages.

Graduate students led the planning and IOP decision making along with the PIs, with daily forecast discussions and planning meetings. Field project participants included the funded PIs, graduate students, and NCAR field personnel, along with volunteers from the department and general public. Operational decisions were based on scientific value and available resources (both equipment and personnel). The project was successful, collecting thousands of observations and documenting 10 PCAP events (Lareau et al. 2013).

Meteorological decisions were based on forecasts of PCAP development. Since the buildup, maintenance, and breakup of PCAPs were all of interest, operations were generally continued throughout entire PCAP episodes. When such episodes were forecast, observations were often intensified via supplemental balloon launches from fixed sites, with the deployment of mobile radiosoundings and the collection of additional surface observations. The timing of the 10 IOP events is shown in Figure 4.2 with UTC begin and end times shown in Table 4.1. Along with basic PCAP lifecycle observations, sub-IOP operations were also occasionally undertaken to explore additional influences on Salt Lake Basin PCAPs caused by canyon flows, slope flows, and interactions with the Great Salt Lake or surrounding topography. The observing platforms used varied depending on experimental goals and equipment and personnel availability.

## 4.4 Observations from PCAPS

Observations were intended to provide the time and space resolution needed to monitor the development of cold-air pools. Surface stations provided information from many different locations and continuous and intermittent vertical profiling from a variety of sites provided information on temporal changes in vertical structure.

### 4.4.1 Surface observations

Surface sensors primarily consisted of pre-existing automatic weather stations within the MesoWest network, a set of 7 NCAR-PAM flux towers located around the valley, and supplemental automatic weather stations deployed near points of interest. HOBO®

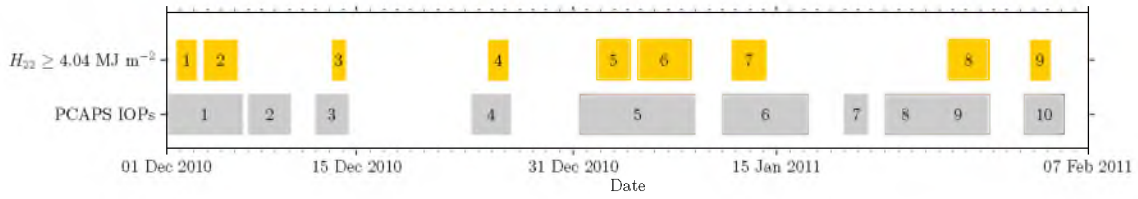


**Figure 4.2**. PCAPS operational timeline. Numbered yellow boxes show periods when $H_{22} \geq 4.04$ MJ m$^{-2}$. The numbered gray areas are PCAPS intensive observation periods. Specific times are shown in Table 4.1.

**Table 4.1**. Beginning and end times (in MST) for IOPs and $H_{22}$-defined PCAP episodes during the PCAPS field program

| Event | Begin | End |
|---|---|---|
| ***PCAPS Intensive observation periods*** | | |
| IOP 1 | Wed Dec 1 05:00:00 2010 | Mon Dec 6 19:00:00 2010 |
| IOP 2 | Tue Dec 7 05:00:00 2010 | Fri Dec 10 08:00:00 2010 |
| IOP 3 | Sun Dec 12 05:00:00 2010 | Tue Dec 14 14:00:00 2010 |
| IOP 4 | Thu Dec 23 17:00:00 2010 | Sun Dec 26 14:00:00 2010 |
| IOP 5 | Fri Dec 31 17:00:00 2010 | Sun Jan 9 05:00:00 2011 |
| IOP 6 | Tue Jan 11 05:00:00 2011 | Mon Jan 17 13:00:00 2011 |
| IOP 7 | Thu Jan 20 05:00:00 2011 | Fri Jan 21 23:00:00 2011 |
| IOP 8 | Sun Jan 23 05:00:00 2011 | Wed Jan 26 05:00:00 2011 |
| IOP 9 | Wed Jan 26 05:00:00 2011 | Sun Jan 30 23:00:00 2011 |
| IOP 10 | Wed Feb 2 11:00:00 2011 | Sat Feb 5 11:00:00 2011 |
| ***PCAP episodes ($H_{22} \geq 4.04$ MJ m$^{-2}$) $\pm$ 6 hours from sounding*** | | |
| Episode 1 | Wed Dec 1 10:00:00 2010 | Fri Dec 3 22:00:00 2010 |
| Episode 2 | Fri Dec 3 10:00:00 2010 | Mon Dec 6 22:00:00 2010 |
| Episode 3 | Sun Dec 12 22:00:00 2010 | Tue Dec 14 22:00:00 2010 |
| Episode 4 | Fri Dec 24 10:00:00 2010 | Sun Dec 26 22:00:00 2010 |
| Episode 5 | Sat Jan 1 10:00:00 2011 | Tue Jan 4 22:00:00 2011 |
| Episode 6 | Tue Jan 4 10:00:00 2011 | Sun Jan 9 10:00:00 2011 |
| Episode 7 | Tue Jan 11 10:00:00 2011 | Fri Jan 14 22:00:00 2011 |
| Episode 8 | Thu Jan 27 10:00:00 2011 | Mon Jan 31 10:00:00 2011 |
| Episode 9 | Wed Feb 2 10:00:00 2011 | Fri Feb 4 22:00:00 2011 |

temperature/RH dataloggers were arranged in lines running up both the Wasatch and Oquirrh mountain sidewalls to make pseudo-vertical soundings with 5-minute temporal and 50-meter vertical resolution (e.g., Whiteman et al. 2008). The NCAR flux towers measured surface radiation and energy balance variables, including incoming and outgoing longwave radiation, incoming and outgoing shortwave radiation, diffuse shortwave radiation, ground heat flux, sensible heat flux, and latent heat flux. Soil moisture and other soil variables were also measured at NCAR flux towers. The surface-based weather data were quality controlled and assimilated to a grid using a 2-dimension variational analysis system described by Tyndall (2011).

Air quality measurements for PCAPS came from two sources. The Utah Division of Air Quality (DAQ) provided criteria pollutant data from multiple sites in the SLV urban area including hourly data on atmospheric particulate matter less than 10 $\mu$m in diameter ($PM_{10}$) and matter less than 2.5 $\mu$m in diameter ($PM_{2.5}$). The $PM_{2.5}$ and $PM_{10}$ data from the Hawthorne Elementary School in the northwest part of the valley were of special interest because lidars respond to atmospheric particulates (see section 3.4.1) and because the SLV is not presently in attainment of the national $PM_{2.5}$ standard. Professor Geoffery Silcox in the University of Utah's Chemical Engineering department also collected $PM_{2.5}$ data from a line of sensors in the Avenues district at the north end of the valley (Silcox et al. 2012).

### 4.4.2 Remote sensing and vertical profiling

Vertical meteorological profiles were made using balloon-borne radiosoundings and surface-based remote sensors. NCAR provided radiosonde, radar, and lidar profiles from two sites in the middle of the valley, as seen in Figure 4.1. The southernmost of the two sites, designated ISS2, was equipped with a radiosonde sounding systems, a ceilometer, a GPS total column water vapor sensor, a scanning Doppler lidar, and a microwave radiometer (provided by San Jose State University). The ceilometer produced attenuated backscatter coefficient profiles every 16 seconds with a vertical resolution of 10 m, and computations of mixing height and cloud height every 5 minutes. A standard automatic weather station that also measured net radiation was located at the site. The other instruments are not used in this research.

The northernmost site, designated ISS 3, was equipped with a 915 MHz Doppler beam swinging-based radar wind profiler and RASS, and an experimental 449 MHz multiantenna profiling radar, along with a standard automatic weather station deployed on a small meteorological tower. The 915 MHz RWP and RASS produced profiles every 30 minutes with 60-m vertical resolution. The 449 MHz RWP produced profiles every 5 minutes with 150-m vertical resolution (Lindseth 2012). The maximum range was set at 4 km to focus on

the boundary layer. A University of Utah minisodar was deployed near the GSL to monitor lake-valley interactions. Finally, the scanning Doppler lidar (SDL) at ISS2 was redeployed in the Bingham Canyon Mine on the west side of the valley briefly at the end of the PCAPS operational period.

Radiosoundings from the ISS 2 site were made during IOPs using the Global Atmospheric Upperair Sounding (GAUS) system, a Vaisala-based radiosonde system. These soundings supplemented radio soundings launched routinely at 12-h intervals by the National Weather Service (NWS) from the Salt Lake International Airport (KSLC) as part of the national upper air sounding network. The KSLC location is indicated in Figure 4.1. By offsetting ISS 2 soundings by 6 hours from KSLC, researchers were able to achieve 6-hour sounding resolution, although from locations separated by 19 km.

During breakup events, soundings were launched as often as every 3 hours and/or at the same time as a KSLC sounding to give increased spatial information. Additional spatial coverage was obtained in special circumstances by launching sondes at other locations from two mobile rawinsonde sets (blue dots on Figure 4.1)

### 4.4.3 Computed datasets from PCAPS

Individual soundings provide vertical profiles at variable vertical resolutions of usually less than 5 meters, at various times and altitudes in the atmosphere. Many forms of analysis benefit from standardized resolutions in both time and space. The PCAPS vertical profiling dataset has been combined into two types of fixed-resolution vertical profiles. The first was a reprocessing of individual radiosoundings into 10-m resolution profiles all originating at 1250 m allowing direct comparison of different measurements without correcting for elevation or resolution. The second analysis combined radiosounding profiles, surface observations, and remote sensor observations, relying on RASS temperatures and RWP winds to provide above-surface information between radiosounding observations.

These variables were combined by PhD student Neal Lareau into an hourly time-height dataset with 10-m vertical resolution. The dataset includes potential temperature, relative humidity and wind components. From the time-height dataset, overlays could be added to other datasets including the ceilometer time-height dataset. This interpolated, fixed-grid dataset has been used in this thesis.

To assist in relating observations to atmospheric state, the valley heat deficit (eq. 2.1) has been calculated for every KSLC radiosounding made during the PCAPS field experiment. The valley heat deficit, a measure of bulk atmospheric stability in the valley, is the heat required to bring a unit column of the valley atmosphere to a constant potential

temperature equal to that observed in radiosonde data at an altitude near the valley top. The heat deficit was calculated to a height of 2200 m MSL, approximately 300 m below the highest ridges of the Oquirrh Mountains west of the valley. Heat deficits calculated to this height, $H_{22}$, are most closely related to high daily-average $PM_{2.5}$ concentrations measured on the valley floor at Hawthorne School (C. D. Whiteman, pers. comm. 2013). Whiteman's previous research found, on the basis of daily $PM_{2.5}$ measurements made at Hawthorne School since 1998, that heat deficits that equal or exceed 4.04 MJ $m^{-2}$ trigger the buildup of cold-air pools in the valley that lead to 24-h observations of $PM_{2.5}$ exceeding 17.5 micrograms per cubic meter, i.e., half of the National Ambient Air Quality Standard for $PM_{2.5}$. Valley heat deficits ranged from near-zero to greater than 11 MJ $m^{-2}$ during the winter period. Periods where $H_{22}$ equaled or exceeded 4.04 MJ $m^{-2}$ are shown as orange boxes in Figure 4.2.

# CHAPTER 5

# ANALYSIS RESULTS

This chapter investigates the use of lidar ceilometers for analyzing the state and structure of the stable boundary layer in CAP environments during the NSF-funded PCAPS study in the Salt Lake Valley, December 2010 to February 2011. Aerosol backscatter is compared to photographic observations of CAP characteristics. Quantitative comparisons are made between low-level backscatter coefficients and surface-based particulate concentrations from an air quality station. Aerosol layer depths and other characteristics are then investigated by applying the objective analysis techniques that have been developed for convective boundary layers as outlined in section 3.4.2. These analysis methods are used to examine ceilometer-observed waves in CAP layers, with emphasis placed on the observation of Kelvin-Helmholz waves. The description and detection of mixing processes in CAPs are investigated using ceilometer data. The analytical benefit of overlaying additional measured datasets on ceilometer backscatter profiles is shown, and with this, the way a CAP interacts with both the valley-based stable layer and large-scale subsidence inversions is described. Finally, the ceilometer analytical techniques developed in the previous sections are combined to describe and relate how particulates, stabilities, and aerosol layer depths behaved during the entire PCAPS project period.

## 5.1 Processing of ceilometer data

Ceilometers are generally used by national weather services in a limited way to generate text messages stating the measured cloud base heights. A modification of the ceilometer's operation and a translation of the resulting encoded data messages are required to access the raw backscatter profiles. For Vaisala ceilometers, the decoding is most frequently done via proprietary software packages such as 'BL-View' or MATLAB-based 'MLH'. These commercial software packages decode and analyze the backscatter profiles, presenting the user with a visual record of the profiles, estimated cloud base heights, and boundary layer depths. To perform additional analysis directly from the backscatter data, the messages

require manual decoding. Technical manuals for the ceilometers provide the necessary information to download and decode data messages. This information was used in this research to decode the ceilometer backscatter profiles using a computer program written in the Python programming language.

Ceilometer data files, after downloading, contain both the backscatter profiles and various status and metadata information, including both internal (e.g., cloud detection algorithm parameters) and external (e.g., detected cloud heights) statistics. Because the status and metadata information was not immediately relevant for this research, decoded backscatter coefficient values $\beta$, as described in section 3.3, were stored separately from the status and metadata messages. Analysis was performed with the former, while the latter was retained in case of future need. In remote sensing, power and variables derivative from power (e.g., the backscatter coefficient) are logarithmic in nature, and for that reason, plots are made contouring $\log_{10}(\beta)$. For certain analyses, this can change the magnitude, shape, or depth of contoured values (such as when computing gradients).

For this thesis, a Vaisala CL-31 lidar ceilometer operated by NCAR/EOL was used. This ceilometer was set up to produce a 7700 m vertical ($<1^o$ deviation from vertical) uncalibrated attenuated backscatter coefficient profile with 10-m range gates every 16 seconds. Each recorded profile is the sum of roughly 160,000 laser pulses (a pulse repetition frequency of 10 kHz). The sum of a large number of shots is used to minimize noise. As is discussed in section 3.3, the Vaisala CL-31 operated at a wavelength of 910 $\pm$ 20 nm. This wavelength, approximated as 1 $\mu$m for scattering theory purposes, varies slightly with laser temperature.

The random background noise in single ceilometer shots can be quite high, a result of atmospheric emission, emitter frequency, and electronic interference. This noise can undermine backscatter data analyses and for that reason, smoothing in time and height is often applied to ceilometer data. Smoothing also allows features such as aerosol gradients to be more recognizable. A proper balance must be obtained to ensure that smoothing to reduce noise does not adversely reduce the detection of meteorological features of interest.

Direct analysis of ceilometer backscatter profiles allows the depiction and analysis of meteorological features that might be impractical or impossible to observe using proprietary commercial software. Backscatter profiles from ceilometers are generally viewed in the form of time-height cross-sections in which the various levels of $\log_{10}\beta$ are plotted in colors. Figure 5.1 is presented as an example. A brief description of this figure will be given to illustrate the techniques, and this figure will be referenced further in later sections of this

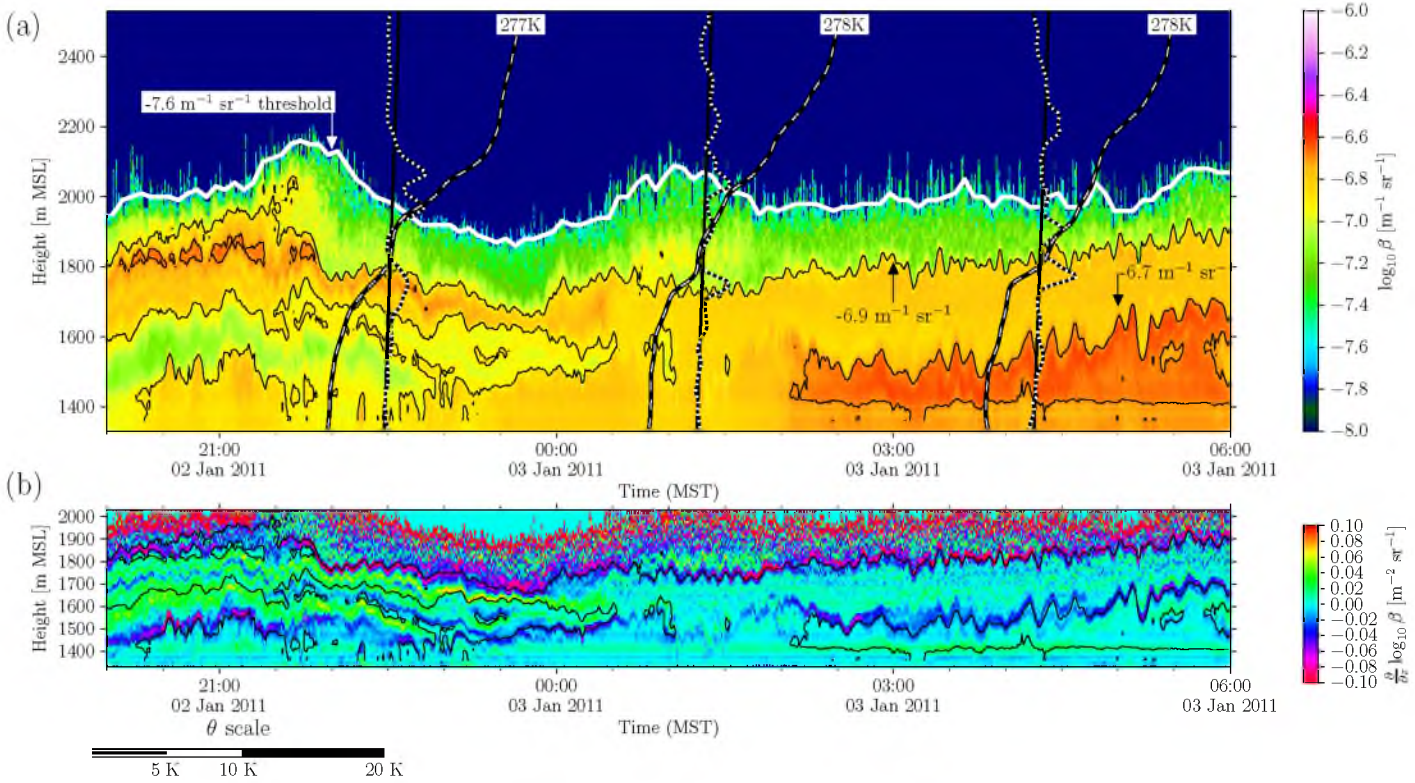


**Figure 5.1**. A demonstration and examination of ceilometer visualizations. (a) Ceilometer backscatter coefficient (see color scale), with NCAR potential temperature ($\theta(z)$) soundings (black and white dashed line) and $\frac{\partial\theta}{\partial z}$ (black and white dotted line) overlaid. The number at the top of each $\theta$ profile is the surface potential temperature for that profile. The near-vertical black solid line indicates the approximate balloon path through the CAP. For the backscatter contour, warmer colors indicate higher particulate backscatter, and gradients in particulate backscatter are indicated by sharp color changes. Backscatter isopleths are plotted at -6.9 and -6.7 m$^{-1}$ sr$^{-1}$ (solid black lines) and -7.6 m$^{-1}$ sr$^{-1}$ (white line). These isopleths indicate different physical processes and boundaries within the aerosol layer. (b) shows the gradient of the backscatter field (colors) and includes the same $\log_{10}\beta$ isopleths as (a). The contoured changes in plotted color are coincident with the strong gradients in aerosol backscatter.

thesis. Figure 5.1 (a) shows an overnight, 10-hour period during PCAPS's IOP 5, where aerosol layers are stratified at the beginning, become more homogeneously distributed in the vertical around 0000 MST and then begin to restratify as sunrise approaches. This information is seen primarily from ceilometer backscatter profiles, which are plotted with a color scale tuned to emphasize aerosol backscatter. The clear atmosphere appears in dark colors, and aerosol concentrations increase from green to red. The customized color scale is set so that backscatter from large particles, such as condensed water droplets, exceed the color scale and are plotted as white (this is not seen in Figure 5.1). This allows the largest variation in colors between aerosol layer backscatter coefficients. To emphasize some of these gradients further, contouring has been applied to this figure at three specific values of aerosol backscatter. The first, represented by a white line, is -7.6 $m^{-1}$ $sr^{-1}$. This value is used to indicate the boundary between the clear and polluted atmosphere layers. The second is a contour of -6.9 $m^{-1}$ $sr^{-1}$, which coincides with the transition from green to orange in Figure 5.1 (a). During the first 4 hours of the plotted period, this contour also highlights the local minimum in aerosols between 100 and 400 m AGL. Finally, a higher $\log_{10}\beta$ value of -6.7 $m^{-1}$ $sr^{-1}$ is contoured to highlight the formation of a stronger (red) layer within the observed aerosol layer. Figure 5.1 (a) also illustrates another technique that will be used throughout this thesis in which data from other meteorological sensors is overlaid on top of the time-height cross-sections (in this case, potential temperature soundings). This overlay technique is a very powerful analysis tool.

Because the color scale is adjusted to highlight changes and strata in the aerosol layer, it is important to ensure that visible gradients in the color of the plot correspond to actual changes in backscatter concentration, as opposed to a change in the colorbar's values. Figure 5.1 (b) shows the same time period as Figure 5.1 (a), plotting the vertical backscatter *gradient*. The three contours from Figure 5.1 are also repeated, and it can be seen that the heights contoured correspond to minima or maxima in the gradient field (minima at the top of a layer, maxima at the bottom). More information on this technique and the analysis of this event will be given in section 5.7. This confirms that when changes in color occur within a plot (this same color scale is used for all ceilometer plots from the PCAPS CL-31), it is indicative of a strong gradient in backscatter magnitude.

### 5.1.1 Effects of hydrometeors on lidar backscatter

In the SLV, common wintertime meteorological phenomena such as snow, fog, and subcloud evaporation (SCE) interfere with the use of the lidar for detecting pollution aerosols that are a primary feature of persistent cold-air pools. These hydrometeors and

aerosols scatter significantly more than pollution-based airborne particulates, significantly attenuating the lidar signal. This strong backscatter and attenuation prevents meaningful analysis (except for specific examples, such as in Rogers et al. (1997)) of the aerosol layer. In a PCAP environment, precipitation that reaches the ground can sometimes eliminate the CAP layer. Complete signal attenuation and multiple order-of-magnitude higher backscatter signals from hydrometeors results in lidar backscatter profiles that do not represent the state of pollutant aerosol particles in the atmosphere. The effects of precipitation on ceilometer aerosol analyses will be seen in later sections of this thesis.

## 5.2 Comparing ceilometer backscatter measurements to CAP photographs

The lidar ceilometer observes backscatter from particles, responding in a way similar to the human eye. Unlike the human eye, which is a passive sensor, the ceilometer can measure particulates along a path (it is range resolved), instead of just an aggregate of emissions at the observed azimuth. Thus, ceilometer backscatter plots are similar to visual photographs, in that the features it observes are similar to those a human would observe, except providing CAP cross-sections instead of passive observations.

Photographs contain passive remotely sensed information from reflected solar insolation within the visible spectrum, 400-700 nm. Since passive detection means all emissions into a path are added together, determining spatial structure of particulates is difficult. As a result, passively observing structure requires an observer to be outside the CAP, which in complex terrain requires being at an elevation equal to or above the top of the aerosol layer. Photographs taken during PCAPS, from within the CAP and at various locations on the valley sidewalls, provide a number of visual records from CAP events. The characteristics photographed can be compared to the ceilometer observations to test the similarity between aerosol backscatter and visual appearance, testing the validity of using a ceilometer to study CAP layer characteristics.

### 5.2.1 Comparison of visible aerosol loading and ceilometer backscatter

In polluted urban atmospheres, CAPs can be identified visually by a layer of polluted air at the bottom of a basin. The loading of aerosols creates an opaque layer of air which is seen both visibly and in lidar backscatter by particle interaction with incident light rays. A quantitative examination will be performed in section 5.3, but it is important to qualitatively show how ceilometer backscatter compares to visual observations. Figure 5.2

uses the visibility of the Wasatch mountains, as viewed from the PCAPS ISS 2 site 18 km away, to compare various levels of aerosol loading in the valley.

Figure 5.2 provides a comparison between ceilometer backscatter and aerosol loading as determined visually. Figures 5.2 (a) and (b) show a clear surface layer, during a pause in precipitation, which resulted in the surface being scoured of particulates. Figures 5.2 (c) and (d) show a period of lighter aerosol concentrations, in which the Wasatch mountains are easily seen. Progressively increasing levels of aerosol loading as determined visually (decreasing discernibility of the Wasatch mountains) are seen in Figures 5.2 (e) and (f), and Figures (g) and (h). Finally, Figures 5.2 (i) and (j) show the impact of fog on the ceilometer. The laser beam attenuates very quickly in fog and clouds, but not before producing significant backscatter from the large particles present at close range.

All of these figures show that as visible loading of aerosols increases, so too does the aerosol backscattering observed by the ceilometer. Though this is an expected conclusion, it is important to demonstrate how the intensity of backscatter observed by the ceilometer relates to what is visually observed.

### 5.2.2 Comparison of visual and ceilometer measurements of aerosol depth

Section 5.2.1 compared visual observations of aerosol loading within a CAP with coincident ceilometer backscatter coefficients. To observe other CAP characteristics, an observer could take a position outside the CAP looking down or across it. The valley sidewalls allowed collection of this kind of information, although such observations were not available on a continuous basis. Above the CAP, an observer can infer characteristics such as the depth of the CAP, the abruptness of the transition from polluted to clear air at the AL top, and the spatial homogeneity of the CAP, both in terms of depth and aerosol concentration. Both the observed AL depth and abruptness of the transition from polluted to clean air can be compared to ceilometer observations to examine the validity of the ceilometer-derived CAP properties.

Figure 5.3 compares photographs taken from above the CAP layer (left side of Figure 5.3) with ceilometer backscatter profiles (right side of Figure 5.3). Figures 5.3 (a) and (c) were taken at or very near the AL top from the side of Grandeur Ridge at elevations of 1850 m, as recorded by the photographer. These elevations correspond well to coincident measurements from the ceilometer. In Figure 5.3 (e), the elevation is unknown, but judging from terrain visible in the background of the figure, the shallow AL is estimated to be 150 m above the Jordan river where the ceilometer is located, which corresponds well with the

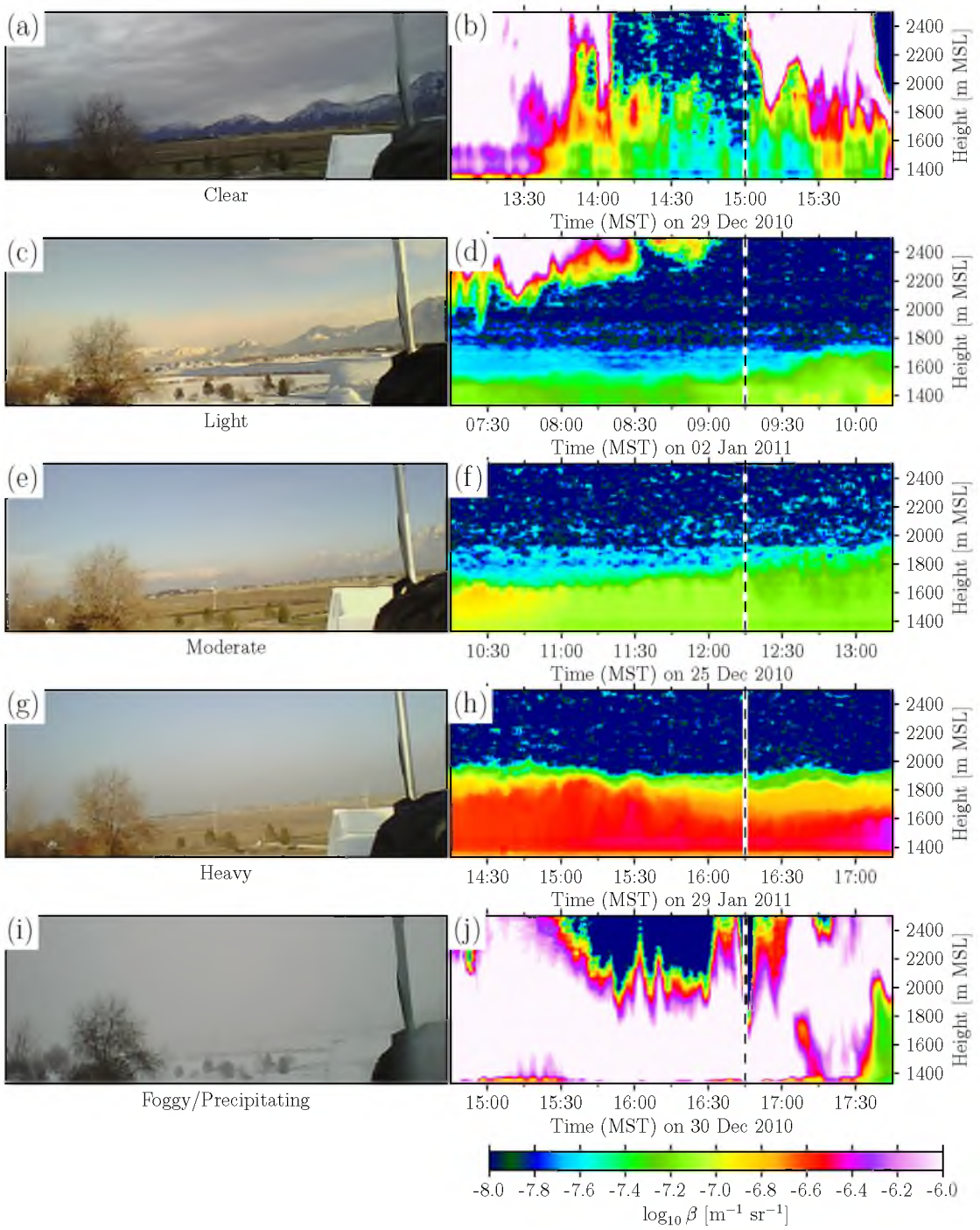


**Figure 5.2**. Photographs from the ISS 2 site ((a), (c), (e), (g), (i)) and corresponding ceilometer backscatter profiles ((b), (d), (f), (h), (j)), where the vertical white-black dashed line indicates the exact time of the photograph. The visibility or clarity of the atmosphere is indicated by the visibility of the Wasatch mountains, where Grandeur peak near the center of Figure (a) is approximately 18 km away.

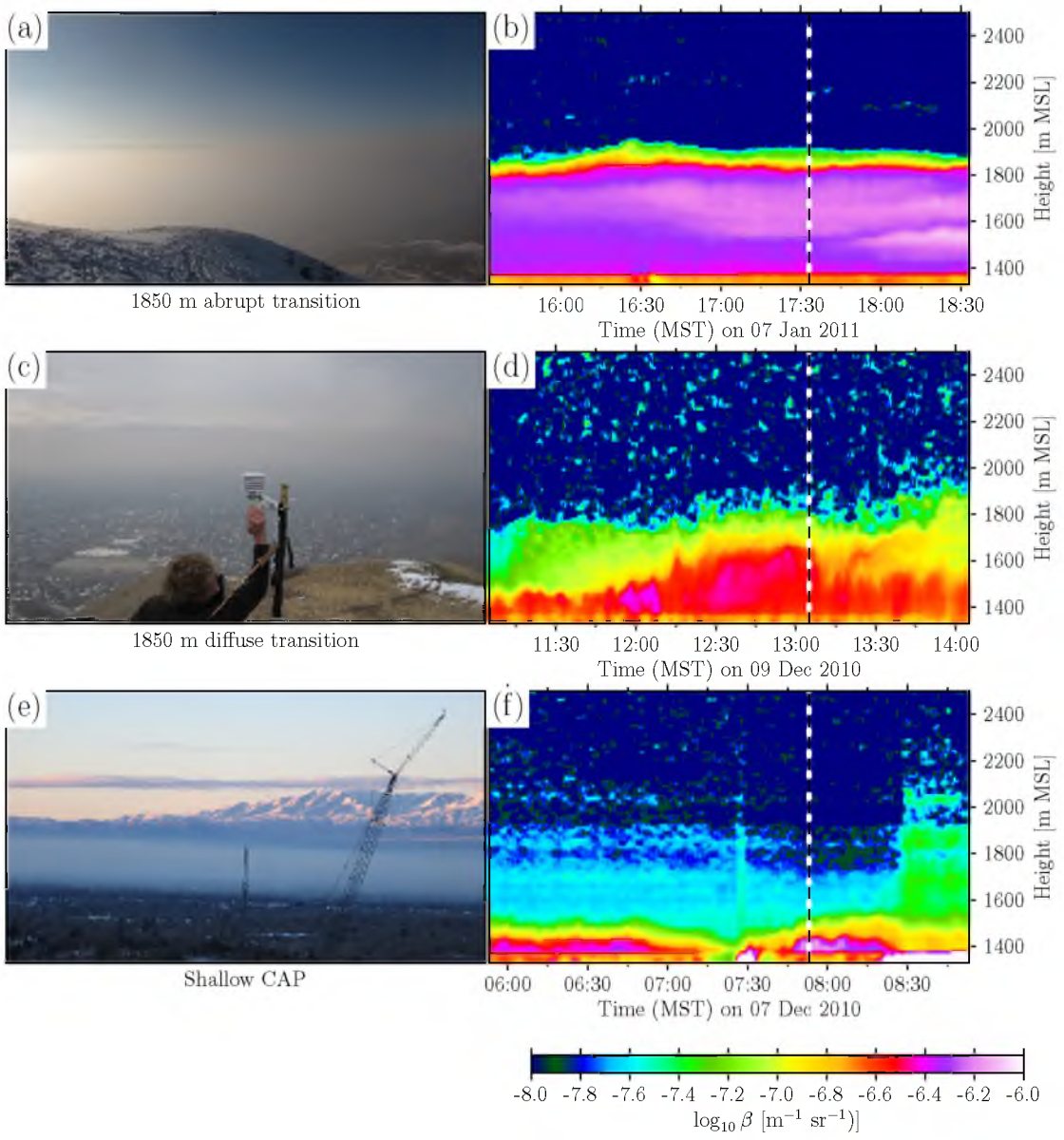


**Figure 5.3**. Comparison of photographs of CAPs from the east ridge of Grandeur Peak with concurrent ceilometer backscatter profiles. Figures (b), (d), and (f) are ceilometer backscatter time-height images recorded from the NCAR ISS 2 site noted in section 4.4.2, spanning the time 2 hours prior through 1 hour after the photographs taken in Figures (a), (c), and (e).

shallow backscatter layer observed in Figure 5.3 (f).

From these examples, the depth of the aerosol layer indicated by the ceilometer corresponds well to the visible layer of particulates seen from above the CAP layer. There are relatively few periods where the depth of the aerosol layer was visually recorded during PCAPS, but for every one, the visible depth of the particulate layers agrees with that seen by the ceilometer. This confirms that, even for densely polluted periods, like that shown in Figures 5.3 (a) and (b), the ceilometer produces an accurate measurement of aerosol depth, and does not appear to attenuate to a degree such that this information is compromised. This is an important finding for the study of PCAPs with ceilometers, as we can be confident that the depths of layers indicated by a ceilometer correspond well to visual estimates.

The last CAP characteristic that can be determined visually is the abruptness of the transition from polluted to clear air. The terms 'diffuse' and 'abrupt' will be used to describe where there is a quick step change or a slow transition from polluted to clear. The causes of the shape of the transition are thought to be similar to the influences on stability at CAP top, described in section 5.7, where stronger gradients are considered indicative of stronger stability, and possibly other mechanisms forcing aerosols up or down.

Figure 5.3 also shows this characteristic. Figure 5.3 (a) shows the appearance of an abrupt transition, where aerosols quickly decrease with height quite near the elevation from which the photo is taken. In agreement, the ceilometer backscatter coefficient profile in Figure 5.3 (b) shows an abrupt transition from -6.3 to -8 $m^{-1}$ $sr^{-1}$. In Figure 5.3 (c), the transition zone is much broader with lower aerosol concentrations and clouds. The broader transition zone is also seen in the ceilometer plot of Figure 5.3 (d). The third comparison, Figure 5.3 (e) and (f), is difficult to interpret visually for the abruptness of the transition because of the low angle of the photograph. Nonetheless, the ceilometer successfully represents the intensity of the transition from polluted to clear atmosphere as well as providing an accurate representation of visual depth.

## 5.3 Backscatter comparison with in-situ particulate concentration measurements

Because the ceilometer beam scatters off aerosol particles, it is important to explore the relationship between in-situ quantitative measurements of atmospheric particulates and backscatter coefficients from ceilometers. This relationship can be used for insight into the vertical distribution of particulates within the CAP environment. Previous researchers have made direct comparisons between in-situ particulate measurements and $\log_{10}\beta$ (Münkel et al. 2007) and have used aerosol-property and distribution estimations to determine

extinction coefficients and lidar ratios (Markowicz et al. 2008). The CAP environment, with nonnegligible beam attenuation and irregular scatterer distribution in both space and size, invalidates most lidar assumptions, so instead, the technique used by Münkel et al. (2007) has been applied for our purposes.

Particulate concentration measurements were available for the PCAPS period from continuous surface monitoring stations operated by the Utah Division of Air Quality (DAQ). The nearest DAQ particulate sampling site was at the Hawthorne Elementary School located approximately 15.4 km northeast of the ceilometer. This station measures near-surface airborne particulate concentrations ($\mu$g m$^{-3}$) on daily and hourly time scales. The measured particle sizes sampled are those less than 2.5 $\mu$m in diameter ($PM_{2.5}$), and those less than 10 $\mu$m in diameter ($PM_{10}$). $PM_{2.5}$ particulates are identified as a hazard to human health because the fine particles enter and deposit in the lungs (Utah Department of Public Health 2013).

Though lidar beams will scatter off any particle, the amount of energy scattered differs from particle to particle. A ceilometer, a low-power remote sensor, cannot easily discern the small amount of energy received from these small particles from noise. 2.5 $\mu$m-diameter particles are quite near the wavelength of the ceilometer ($\approx$ 1 $\mu$m), resulting in variable scattering characteristics, as seen in Figure 3.1. Larger particles scatter more as a function of both their size and concentration. Thus, more scattered energy is received from larger particles, and changes in the concentration of larger particles is associated with increases in lidar backscatter (Münkel et al. 2007; Vaisala 2004). Thus, $PM_{10}$ particles will account for more of the scattering than $PM_{2.5}$ particles.

### 5.3.1 Filtering the $PM_{10} - \beta$ comparison dataset

#### 5.3.1.1 Correcting for influences of ambient moisture

Increases in aerosol particle concentration are expected to produce concurrent changes in both $PM_{10}$ and $\log_{10}\beta$. However, increases in particle size could cause an increase in backscatter without necessarily changing $PM_{10}$ concentrations. The main driver of changes in particle size is moisture. High ambient moisture will cause hygroscopic particulates to swell with moisture, or even condense into cloud droplets. When this occurs, the $PM_{10}$-$\log_{10}\beta$ relationship is not expected to hold. For this reason, periods of high moisture when relative humidity exceeds 80% at the surface or in the first 250 m (from the smoothed time-height dataset discussed in section 4.4.3) are excluded from our analysis.

While we exclude the high humidity events from our main analysis, it is important to point out that ceilometers can be used to verify this relationship between scattering

and moisture uptake. Figure 5.4 shows backscatter during a period of high surface (and CAP) relative humidity in which backscatter increases with time at lower levels (Figure 5.4 (a)). The corresponding time series of $PM_{10}$, RH, and 1400 m MSL backscatter coefficient are shown in Figure 5.4 (b). High surface RH between the hours of 0900 to 1500 MST corresponds to decreasing $PM_{10}$ and increasing backscatter. Backscatter increase is most likely from enlarged particles, as moisture is unlikely to create a higher concentration of particles. The effect on $PM_{10}$ is either a result of increased settling and precipitation of the particles from the air, or a portion of particles growing beyond 10 $\mu$m in diameter, and therefore not being measured by the $PM_{10}$ metric. Both processes contribute to the decrease in $PM_{10}$ observed.

#### 5.3.1.2 Restricting comparison to periods with a CAP

To best represent and identify CAP characteristics, the comparison between $\beta$ and $PM_{10}$ is made only during periods when a CAP was present. A CAP was considered to be present when potential temperature at 2500 m MSL (basin-top temperature) exceeded the potential temperature at the surface by 4 K. If the potential temperature deficit is less than 4 K, a CAP is not present in the valley. This lenient CAP definition is used to allow the filtered dataset to be as large as possible.

#### 5.3.1.3 Determining temporal and spatial ranges to compare

An analysis was performed to determine the temporal period of ceilometer profiles that best compares to the hour-averaged $PM_{10}$ sampling period. For collocated measurements, the ceilometer backscatter would be averaged over the same hour during which the particulate measurements are taken. Due to the distance between the two measurement sites, we attempted to determine if any temporal shift in averaging times would improve correlations. The correlations of the PCAPS dataset were computed for 10 different temporal ranges before and after the period during which the $PM_{10}$ measurement was made. The hour that was contemporaneous with the $PM_{10}$ observation was found to provide the best correlation.

A final analysis consideration was to determine the appropriate vertical range of the ceilometer profile to use. The first 30 m of ceilometer data are influenced by the lidar overlap function (discussed in section 3.2), and appear to suppress backscatter values in excess of -6.7 $m^{-1}$ $sr^{-1}$. Therefore, values from a higher level must be used to compare to the surface-based particulate concentration measurements. The study by Münkel et al. in CBLs used the averaged backscatter profile from 0 to 70 m AGL. Our correlations between

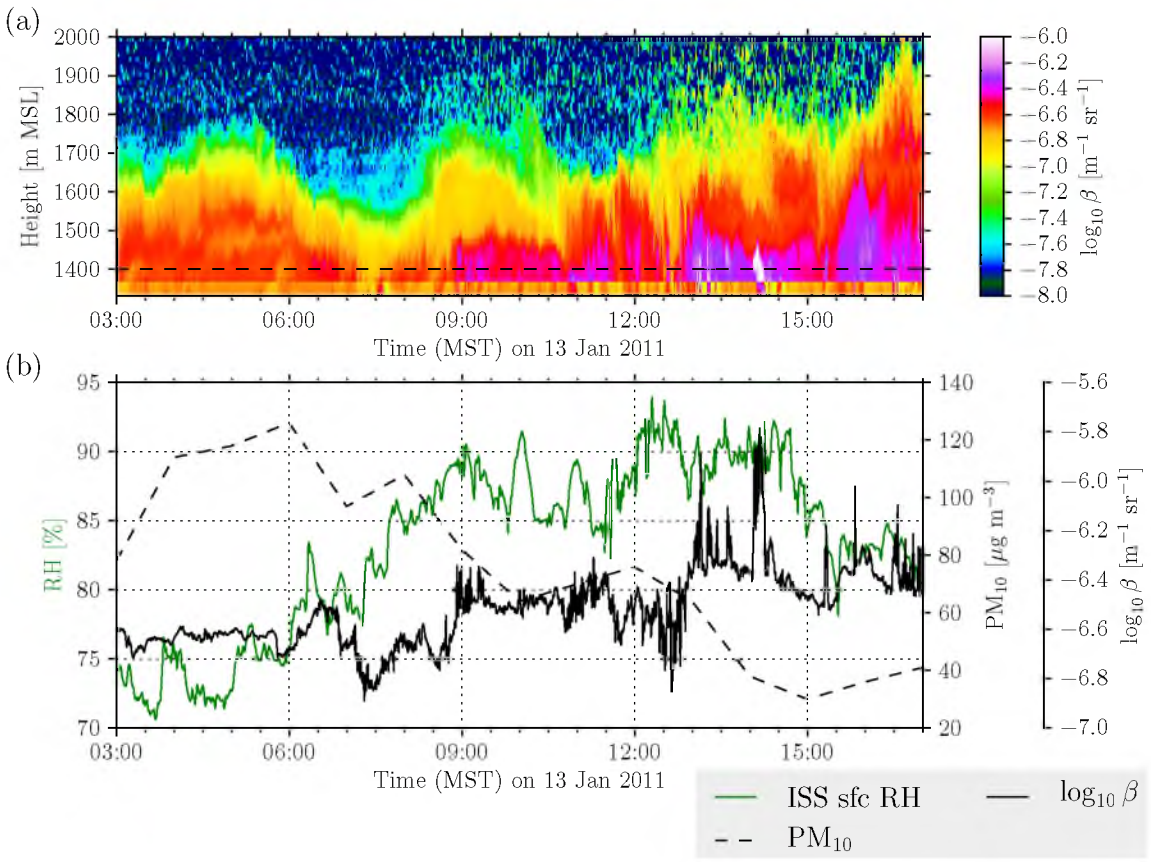


**Figure 5.4**. A demonstration of the effect of relative humidity on ceilometer backscatter coefficient and $PM_{10}$ measurements. (a) ceilometer time-height cross-section of backscatter between 0300 and 1700 MST 13 January 2011. (b) time series of measurements of surface RH (green line), $PM_{10}$ (dashed line), and $\log_{10}\beta$ at 1400 m MSL (solid black line) for the same time period as (a).

$PM_{10}$ and $\log_{10}\beta$ were tested for a set of 10 vertical ranges. An average between 30 to 50 m AGL produced the highest correlation. This value is reasonable because it is the lowest possible level, allowing the closest assessment of ground conditions in a nonconvective environment. The short averaging length (only 20 m as compared to 70 m in Münkel et al. (2007)) is assumed to reduce the influence of strong stratification observed in PCAP events, increasing the likelihood that the aerosol concentration sampled is that of the surface.

Hourly $PM_{10}$ particulate concentration measurements at Hawthorne Elementary were compared with ISS ceilometer backscatter coefficient averaged between 30 to 50 m AGL over the hour of the corresponding $PM_{10}$ observation for all times when the potential temperature difference between 2500 m AMSL and the surface were greater than 4 K, and the relative humidity in the lowest 250 m of the atmosphere was below 80%. The final dataset consisted of 490 individual $PM_{10}$ and backscatter coefficient observations.

### 5.3.2 Results from comparing backscatter coefficient to $PM_{10}$

The scatter of these two variables is shown in Figure 5.5, where a linear relationship between the $\log_{10}$ backscatter coefficient and $PM_{10}$ concentration is identified, with a correlation coefficient of 0.65.

There are several implications from the correlation between particulate concentration and backscatter coefficient highlighted in Figure 5.5. The first is that a similar relationship exists between backscatter and $PM_{10}$ concentration for cold-air pools as was identified by Münkel et al. (2007) for convective boundary layers. This verifies what is qualitatively assessed in section 5.2, that ceilometer backscatter is a useful proxy for the concentration of particulates within the CAP. Münkel et al. (2007) investigated particulates that were convectively mixed from the surface. In contrast, in CAPs the particulate concentrations aloft often differ from those at the surface. When relative humidity is low, ceilometer backscatter can be viewed as a proxy for the concentration of larger particles suspended in the air.

Correlation measures the degree of linear fit between two variables. A correlation of 0.65 suggests that a linear fit between the two variables ($PM_{10}$ and $\log_{10}\beta$) produces reasonable agreement. This relationship is log-linear with respect to $\beta$, which confirms theoretical expectations that backscattering varies linearly with scatterer number concentration, when particle sizes are not changing (eq. 3.4).

To explore the relationship further, Figure 5.5 (b), uses the backscatter coefficient and the linear regression equation to estimate $PM_{10}$ concentrations for the entire PCAPS period. A high degree of similarity occurs during PCAP episodes, with significant divergence

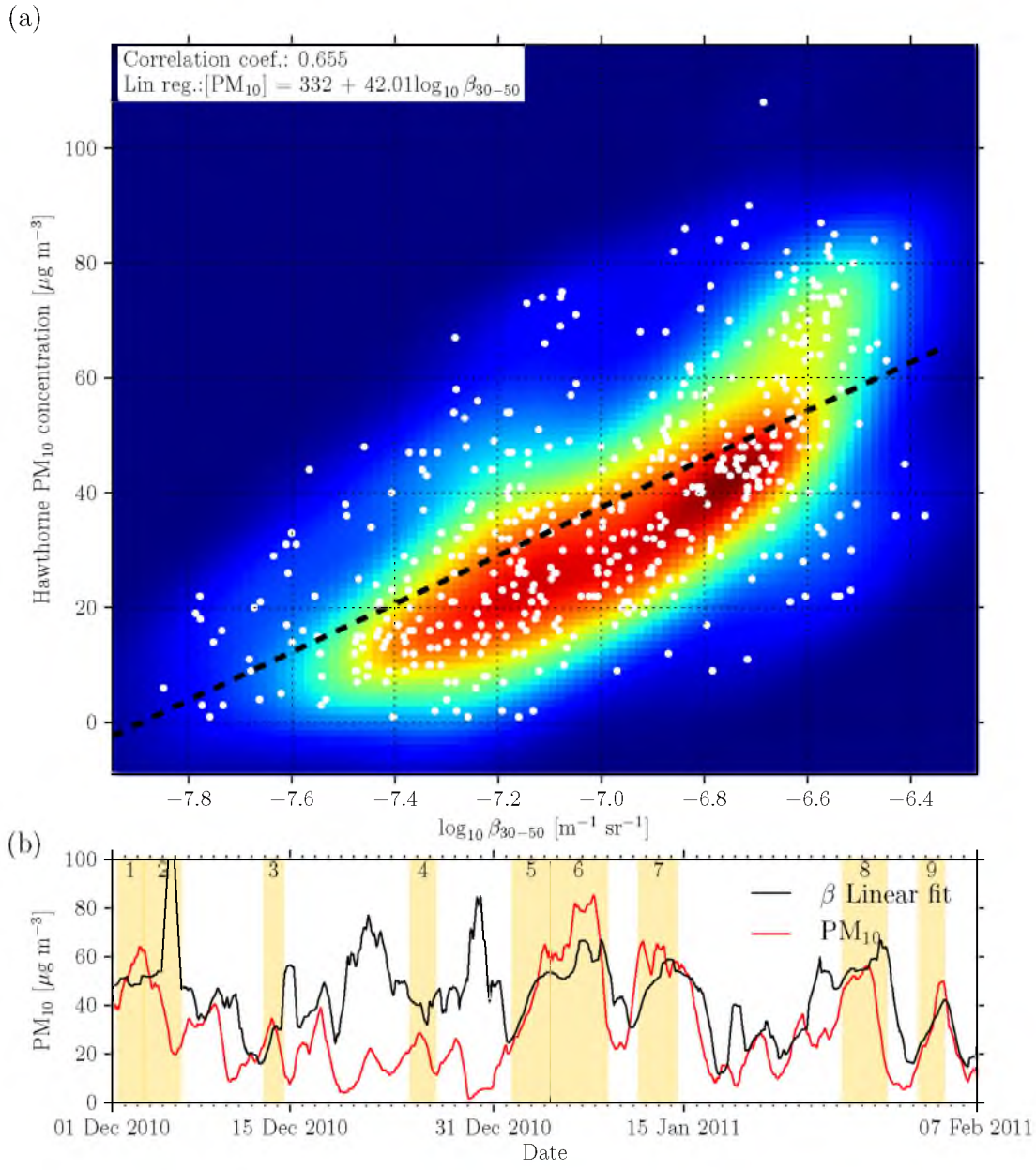


**Figure 5.5**. Direct comparison of low-level ceilometer backscatter and surface $PM_{10}$ measurements. (a) scatter plot of Hawthorne $PM_{10}$ concentrations and 60-minute average 30-50 m ceilometer backscatter coefficient ($\log_{10}\beta_{30-50}$) during PCAPS CAP events (identified by a ridge-top to surface $\theta$ deficit greater than 4 K) where surface RH was less than 80%. A black dashed line indicates the linear fit computed from the scattered data. (b) 24-hour running mean smoothed $PM_{10}$ curve (red) and an estimate of $PM_{10}$ concentration (black) using backscatter data and the linear regression between backscatter and $PM_{10}$ concentration. PCAPs periods defined by $H_{22} \geq 4.04$ MJ m$^{-2}$ are shaded in yellow.

during non-PCAP periods. This is likely due to higher moisture and precipitation in non-IOP periods, which scour particulates while providing high backscatter. Thus, the CAP environment appears to be one in which the ceilometer data from a near-ground layer provides a reasonable estimate of surface $PM_{10}$ concentrations.

From the Münkel et al. (2007) study, a correlation coefficient of 0.84 was found for this same relationship in a convective boundary layer between a collocated particulate sampler and a ceilometer. The reasonably good correlation found in our experiment suggests that aerosol concentrations associated with backscatter in the stable atmosphere at 30 to 50 m AGL are frequently similar to aerosol concentrations near the surface, even at spatially distant locations.

The complexities of the PCAP environment, and the resulting requirement to remove nearly 2/3 of the dataset, means that it is impractical to invert this analysis and compute $PM_{10}$ concentrations from ceilometer backscatter. Additionally, as ceilometer backscatter is uncalibrated, any relationship derived at one time is not expected to persist over time, as instrument characteristics change and are not corrected for. Like many areas of ceilometer analysis, the tool serves primarily as a visual and qualitative resource, rather than a quantitative mechanism for making complex atmospheric measurements. The rest of the work in this thesis analyzes ceilometer backscatter coefficient profiles under the assumption that aerosol concentration governs the backscatter received from the ceilometer.

## 5.4 Evaluation of automated methods for determining aerosol layer depth

This section applies the automated methods in section 3.4.2 to estimate aerosol depths, aiming to determine the best method for use in the stable boundary layer of persistent cold-air pools. These methods were originally developed for analysis of the convective boundary layer (CBL), and it is expected that their performance will vary when applied to nonhomogeneous stable boundary layers. The significant stratification and high aerosol content improve the performance of some methods, such as the gradient and threshold methods, while layering within the aerosol layer (AL) inhibits some other methods of analyses. Other differences are expected to exist between CBL and CAP AL analysis. This section explores the applications of aerosol depth algorithms in describing and analyzing stable CAPs.

### 5.4.1 Threshold or isopleth method

The simplest method of quantitatively analyzing backscatter coefficient time-height datasets is to subjectively identify particular $\log_{10}\beta$ values that are of interest, and isopleth these values. This was demonstrated by the thin black and thick white lines on Figure 5.1. By visual inspection, a threshold value for contouring the top of the layer of surface-based aerosols was estimated (for this Vaisala CL-31 ceilometer) as -7.6 $m^{-1}$ $sr^{-1}$. This is shown as the white contour on Figure 5.1 (smoothed over 5 minutes). The top of the aerosol layer can be continuously identified by contouring the elevation where the backscatter exceeds this threshold. Contours are conventionally used in plots to emphasize changes in a field, and they are used similarly in Figure 5.1, where the behavior of different aerosol layers in the CAP are accentuated with the contours.

A single threshold value was found to suffice for AL depth during the entire PCAPS period. This is because of the large difference between AL and free troposphere backscattering values. The changes and errors resulting from uncalibrated backscatter values did not affect the backscatter levels in a large enough way to make the identified value fail at some point. However, it is important to recognize the influence of calibration, that even for a single instrument a specific threshold value, in polluted PCAP ALs, will not hold for the lifetime of the instrument.

Thus, the choice of a threshold value is subjective but, once chosen, the clean air threshold value for a particular lidar is surprisingly robust from PCAP event to PCAP event, at least for a single winter season. This method is the most reliable way of determining the height of the top of the aerosol layer during an urban (i.e., polluted) PCAP event, and should provide very useful information for gaining understanding of pollution transport and distribution in PCAP episodes.

### 5.4.2 Gradient method

The gradient method described in section 3.4.2.2 performs well when applied to backscatter profiles from PCAP ceilometer observations. This analysis method was illustrated previously in Figure 5.1 (b) where the gradient of the backscatter coefficient field is plotted to highlight the changes in backscatter concentration. Figure 5.6 illustrates another application of this method, showing the gradient method is able to detect multiple gradients that form within the polluted aerosol layer of a PCAP. With a 5-minute time smoothing and 20-m vertical smoothing, the method is able to reliably detect coherent gradients within the CAP aerosol layer. In CBL research, the strongest gradient is expected to indicate the top of the surface-based convective layer. Since convective mixing is not occurring in a PCAP,

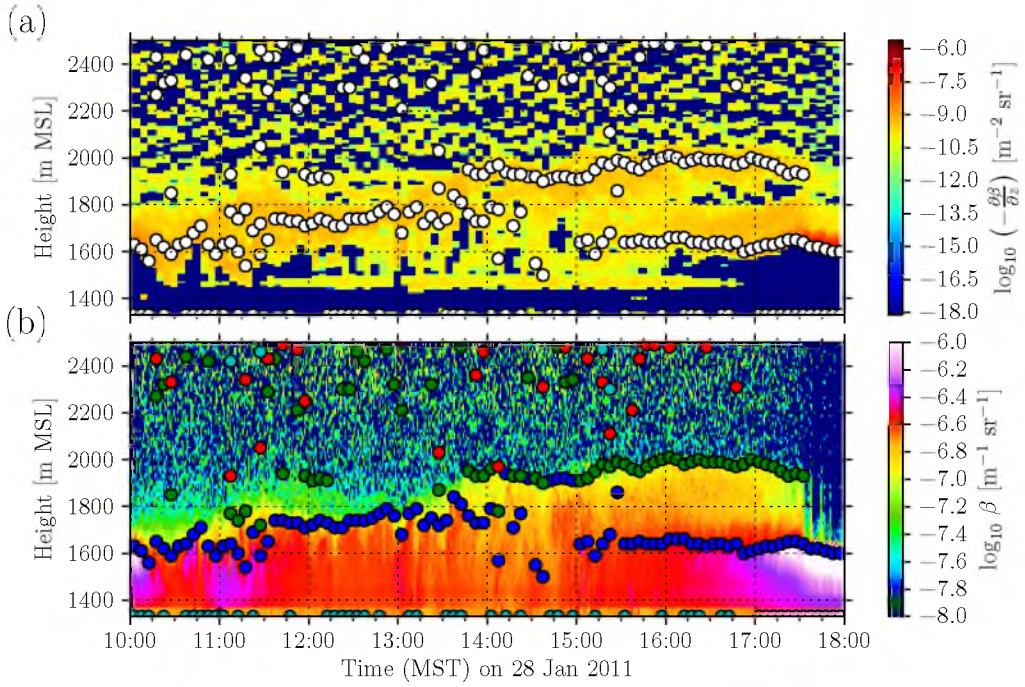


**Figure 5.6**. Illustration of the gradient method for determining aerosol depth and layering in a PCAP. (a) shows the computed $\log_{10}$ of the negative gradient field, which is analyzed for local minima exceeding -9.7 $m^{-2}$ $sr^{-1}$ over 40-m height intervals. White dots are located at these points. (b) shows these same points plotted on the original backscatter field, where colors indicate the order of detection, with blue being first, then green, red, and turquoise. The gradient method's ability to identify internal gradients is the main application of the method, as gradients can be symbolic of mixing, stability, or particulate formation. The detection of multiple gradients is important, as this allows for the identification of gradients within the CAP.

gradients are not necessarily strongest at the top of the aerosol layer but can, instead, identify aerosol layering within a PCAP.

The gradient method, as shown in Figure 5.6, can detect gradients within the aerosol layer that form as a result of nonhomogeneous mixing processes within a PCAP. Where computed gradients, such as those in Figure 5.6 (a), are local minima that exceed a subjective gradient threshold (-9.7 $m^{-2}sr^{-1}$ for Figure 5.6), an elevation point is detected. The algorithm we used can detect up to four elevation points per averaging time interval. Figure 5.6 shows that, unfortunately, bogus gradients can be identified by this method in the noise above the CAP aerosol layer. There are, however, techniques to eliminate these points.

### 5.4.3 Inflection point method

The inflection point method of determining CBL depth outlined in section 3.4.2.3 has proven to be poorly suited for study of PCAPs. The method is illustrated in Figure 5.7, where the computed inflection point field (Figure 5.7 (a)) is extremely noisy and provides little information. The white and black lines indicating MLH determinations in Figure 5.7 (b) provide little information of use in stable boundary layers. This method is very sensitive to background noise, and smoothing procedures that can markedly smooth noise for the gradient method do not seem to completely eliminate variations, which are accentuated by the inflection point method. This method is not investigated further in this thesis.

### 5.4.4 Idealized profile method

The idealized profile method described by Eresmaa et al. (2005) and in section 3.4.2.4 is well suited to PCAP analysis because the structure approximated by the single inflection idealized profile function (Figure 3.5) is very similar to the step change in backscatter observed in a polluted PCAP. The method fits a function (eq. 3.14) to the backscatter profile by iteratively solving for two variables: the height of the aerosol layer ($h$) and the thickness or intensity of the transition from polluted to clear air ($\Delta h$, the same concept as the visible transition in section 5.2.2). Initial guesses and values for boundary layer and free atmosphere backscatter intensity are required to determine the function. Testing shows that the first guesses of $h$ and $\Delta h$ are relatively unimportant, though the initial values chosen for backscatter in the layers can strongly impact the analyses. If the CAP aerosol backscatter ($B_m$) value is too high, or the free atmosphere value ($B_u$) is too low, the method is likely to settle on a solution wherein the $\Delta h$ is very large and $h$ is too low. The reverse of this is not true. If $B_m$ is too low or $B_u$ too high, only the value of $\Delta h$ will be altered.

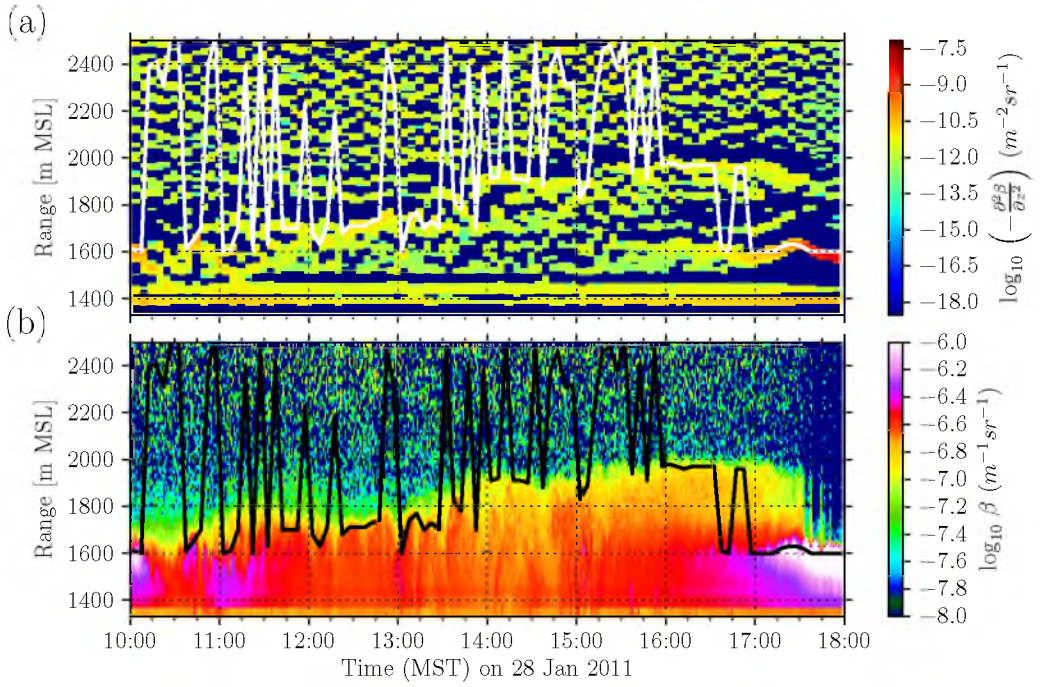


**Figure 5.7**. Illustration of the inflection point method for determining mixing layer height, with (a) showing the computed field as well as the best guess MLH (white line), and (b) with MLH (black line) plotted on top of the original backscatter field. The sporadic nature of the detected height is indicative of the method's performance in PCAP environments. The MLH has little meaning in a stable boundary layer, as opposed to the convective boundary layer.

The height detected by the idealized profile method is almost always near the top of the actual aerosol layer, as is seen in Figure 5.8. Thus, the novel information that can be garnered from this method is an estimate of $\Delta h$. Figure 5.8 shows the value of $\Delta h$ as the distance between the solid line ($h$) and the dashed lines. If the value of $\Delta h$ is large, then the polluted to clear air transition gradient is diffuse, suggesting a lower concentration of particulates in the top level of the CAP (e.g., Figure 5.3 (c)). If $\Delta h$ is small, an abrupt change from polluted to clear is indicated (e.g., Figure 5.3 (a)). The causes of sharp transitions are not well understood. It is expected that some form of forcing, such as a compressing subsidence inversion, or another form of strong stability may force an abrupt transition at the top. Additionally, weak convection may raise surface-based particles to the point of stability without the overshooting and turbulence, which would be expected with a convecting air parcel. Finally, turbulent erosion may create sharp transitions by removing aerosols from the top layers of the CAP, while at the same time sharpening the potential temperature gradient.

### 5.4.5 Variance method

The final method evaluated was the variance method, illustrated in Figure 5.9. This method, described in section 3.4.2.5, applies poorly to CAP investigations. This method is able to detect variations in backscatter levels between the clean free atmosphere and the top of the polluted CAP, but is unable to detect oscillations associated with mixing within the CAP layer. The cause of this limitation is the difference in the magnitude of backscatter variations between CAP-top and mid-CAP levels. At the top of the CAP, variances are between the clear atmosphere and the top of the CAP. At mid-CAP levels, however, the variation is between a layer of one aerosol content and a layer with a similar but different aerosol content. Thus, this variance is smaller due to the smaller differences in the values between the oscillating air masses.

Figure 5.9 highlights this limitation, where variance variations at the CAP-top are significantly greater than those within the CAP. A large sensitivity to noise and a complex behavior during airmass changes such as fog make the method unreliable, as is seen after 1700 MST in Figure 5.9. This method, like the inflection point method, does not perform well in PCAP conditions. Like the idealized profile method, the determination of the aerosol layer top is inferior to that of the threshold method. Therefore, the variance method is not used further in this research.

A summary of the different methods of objective aerosol layer analysis is given in Table 5.1. The inflection point and variance methods have little utility in PCAPS analysis. The

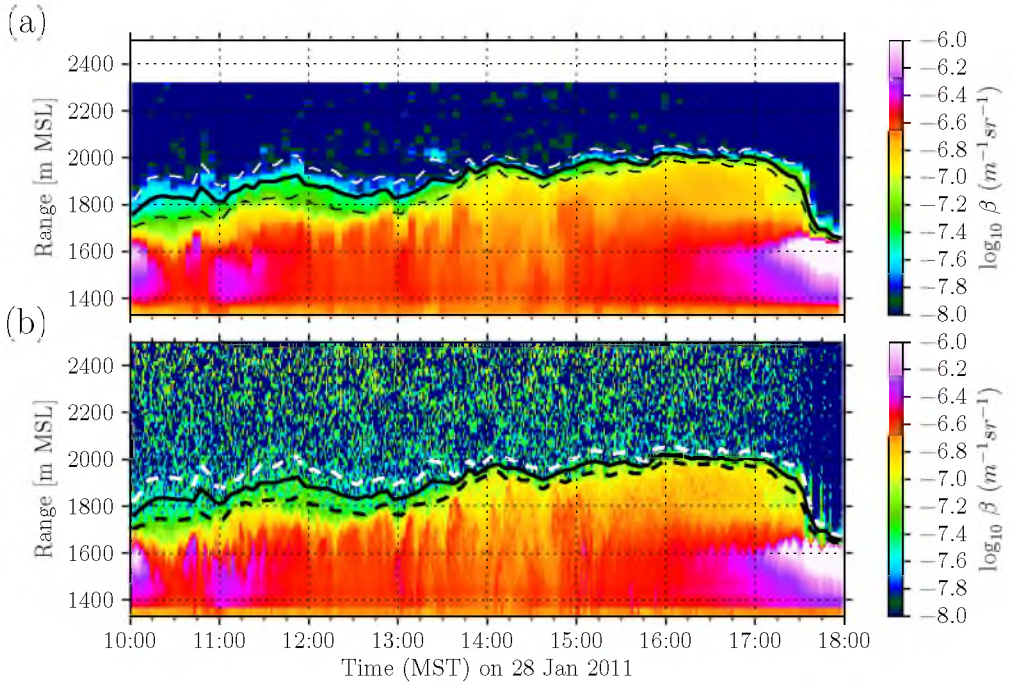


**Figure 5.8**. Illustration of the idealized profile method for determining CAP depth where a) shows the smoothed backscatter coefficient ($\beta$) field that is used for fitting, and b) shows the unsmoothed $\beta$ field. The solid line is the aerosol layer depth, term $h$ in eq. 3.14. The dashed lines show the range of $\Delta h$, also from eq. 3.14.

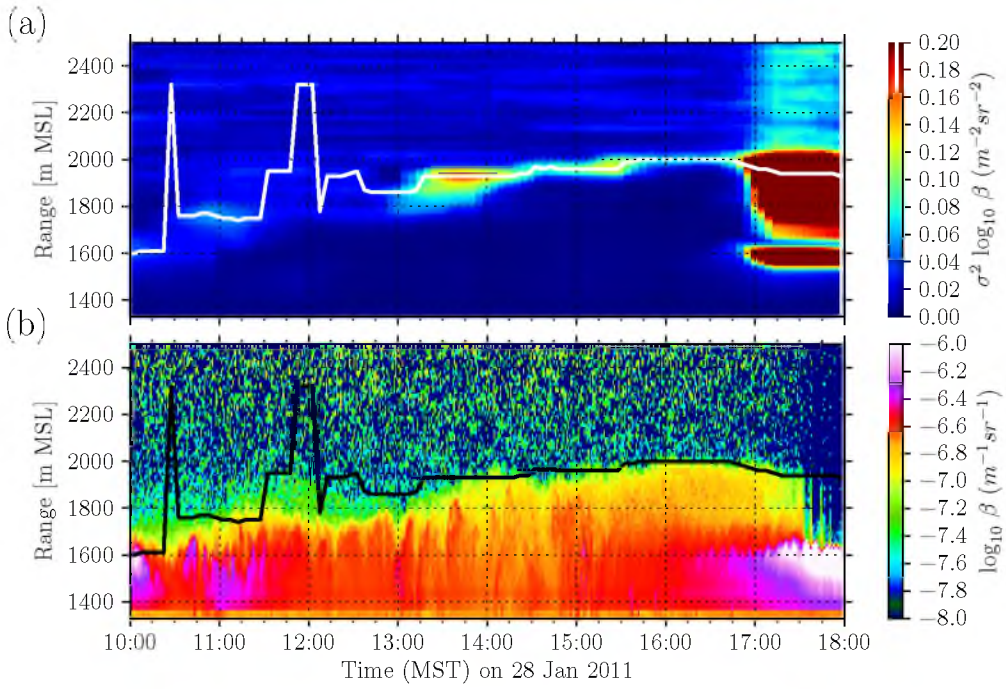


**Figure 5.9**. Variance method of detecting aerosol and mixing heights applied within a PCAP. (a) The field of temporal variance computed over 100 minutes using 5-minute smoothed ceilometer backscatter coefficients. Depths (white line) are detected as local maxima in this field. (b) shows the MLH depth from the variance method plotted on top of an unsmoothed ceilometer backscatter field.

**Table 5.1**. Summary of the application of objective MLH/aerosol layer analysis methods for CAPs. $\beta_s$ is a smoothed backscatter coefficient profile, AL in the applications column means aerosol layer.

| Method | Resolution ($s$) | Expression | Remarks | PCAP Applications |
|---|---|---|---|---|
| Threshold | 16 | $\beta >$ thresh. | Simple method that performs well in polluted PCAPs. Subjective. (Melfi et al. 1985) | AL top or internal layers |
| Gradient | 300 | $\min(\partial\beta_s/\partial z)$ | Additional uses when detecting local minimums instead of absolute minimum. Can be subjective (Hayden et al. 1997) | internal mixing, stratification |
| Inflection point | 1800 | $\min(\partial^2\beta_s/\partial z^2)$ | Small values result in high noise sensitivity. CAP characteristics not especially distinct. (Menut et al. 1999) | None identified |
| Idealized profile | 16 | $\min\left(\sum_{z=0}^{z_t}(\beta_s(z) - f(z))^2\right)$ | Robust detection, produces limited CAP information, but does indicate entrainment depth. (Steyn et al. 1999) | AL top, entrainment layer thickness |
| Variance | 300 | $\max(\sigma^2_{\text{time}}(\beta_s))$ | Theory does not apply well to PCAPs; see text. (Piironen and Eloranta 1995) | AL top |

other three methods can be used in different ways to analyze the state of the CAP layer.

Convective boundary layer lidar analysis methods, as expected, perform differently in persistent CAP atmospheres. This is due to different structuring and mixing, along with higher concentrations and increased inhomogeneity of aerosols in such atmospheres. The best of these methods are able to reliably detect the top of the AL. The threshold method is the best at detecting the top of the AL during the PCAPS period. The inflection point, while robust, does not perform well with shallow CAPS or low aerosol concentrations.

## 5.5 Waves in cold-air pools

In this section, we investigate the suitability of ceilometers for observing atmospheric wave motions in CAPs. As has been shown previously, ceilometers create detailed time-height profiles of the structure of aerosols within a persistent CAP. The 16-second temporal resolution of the Vaisala CL-31 ceilometer is sufficient for observing high-frequency oscillations in backscatter. Figure 5.1 shows a period where short oscillations in both the -6.9 and -6.7 $m^{-1}$ $sr^{-1}$ contoured layers are observed with an amplitude of about 100 m. The PCAPS ceilometer dataset observed many similar wave events that occurred on top of and within CAP layers. Ceilometer data are particularly useful for these observations, as ceilometer time resolution is usually much better than the time resolution of other vertical profiling remote sensors. The implications of observed oscillation characteristics are discussed and shear-induced Kelvin-Helmholz waves are examined.

### 5.5.1 Observing and describing waves in CAPs

Wave motions have been observed in lidar/aerosol backscatter time-height profiles from within nocturnal stable boundary layers in previous complex terrain meteorological research (Hayden et al. 1997; Cooper et al. 2006; Pinto et al. 2006). These observations were similar to those made in PCAPs, although the focus of these previous studies was generally on oscillations produced by speed shear and down-valley jets. Persistent CAPs differ in some respects, however, from nocturnal SBLs, as they tend to have higher pollutant levels.

Figure 5.10 shows several forms of oscillations observed during PCAPS with the lidar ceilometer. Figure 5.10 (a) shows symmetrical (in time) waves occupying the full depth of the CAP, similar in appearance to Kelvin-Helmholz waves observed by Pinto et al. (2006). The waves of Pinto et al., however, were produced by a down-valley jet just above the CAP. Wind vectors show no such jet in Figure 5.10 (a). Symmetrical waves in weakly forced environments, similar to those in Figure 5.10 (a), were the most common types of oscillations observed during PCAPS. Figure 5.10 (b) shows a more complex period with

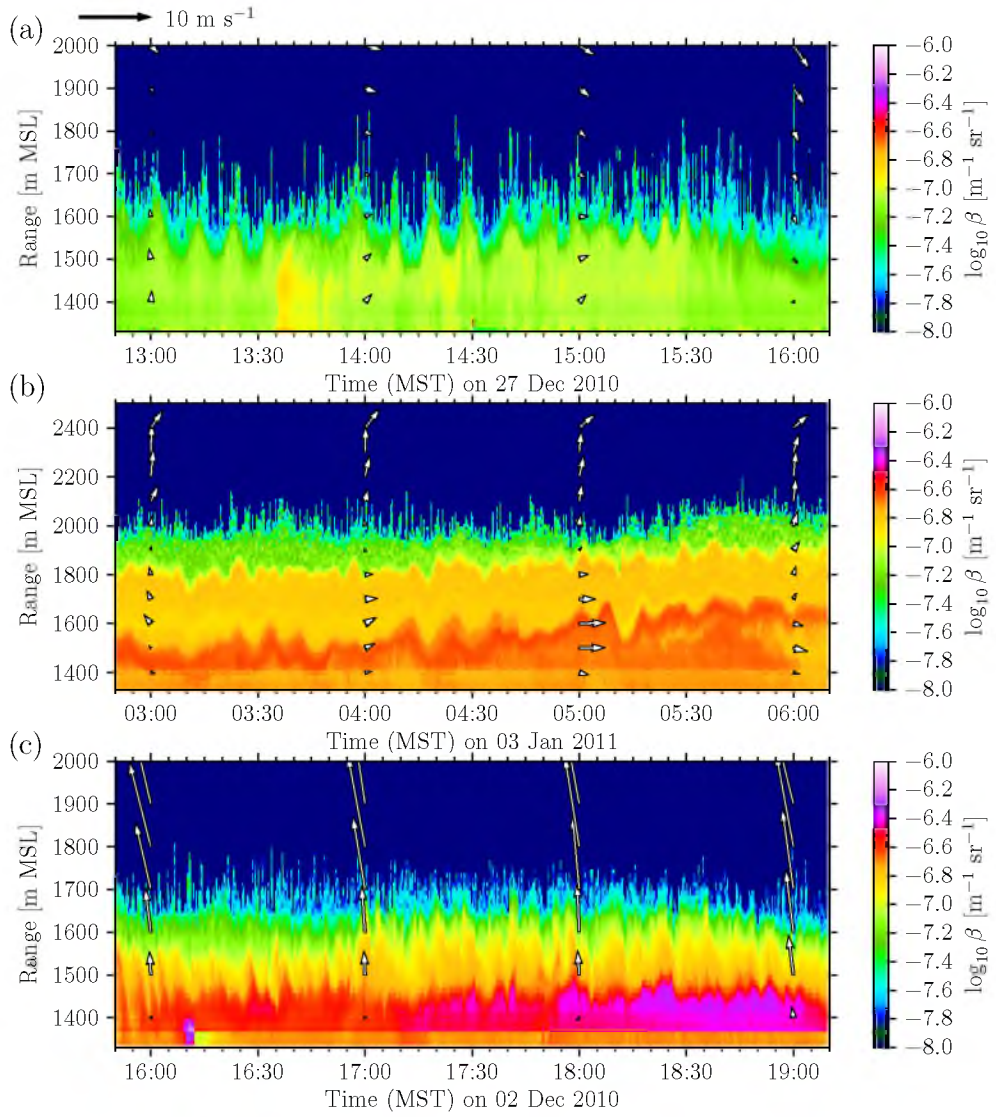


**Figure 5.10**. Examples of different types of oscillations observed in lidar backscatter coefficients (see scale), with radiosonde-derived wind vectors plotted as an overlay. The wind arrows indicate horizontal wind directions (an arrow pointing down is a north wind, an arrow pointing to the right is a west wind, etc.). Wind speeds are given by the lengths of the arrows using the scale in the top-left corner. (a) shows light winds above and within the CAP layer, and oscillations of the entire CAP. (b) shows waves within multiple layers of a CAP, with weak winds within, and light southerly winds above the CAP. (c) shows high-frequency shear-induced waves, with southerly winds increasing with height throughout the aerosol layer.

light wind shear above the CAP layer, and waves in two internal layers, but not necessarily at the top of the aerosol layer. Figure 5.10 (c) shows waves that are produced during a period of large speed shear in the vertical from strong southerly winds. The resulting waves are deep, and with shorter wavelengths than than those in Figures 5.10 (a) and (b), and are asymmetrical. These waves were frequently observed, and are shown to be Kelvin-Helmholz waves later in this section.

Few PCAPS observing platforms had the necessary temporal or spatial resolution to resolve the oscillations. High-resolution surface $w$ perturbation measurements could observe the waves if they were coupled with the surface (as seen by Cooper et al. (2006)); however, the strong stratification in our case decouples the upper CAP layers from the surface, suppressing or eliminating the ground wave signal in currently available PCAPS datasets.

Waves were observed at the top of a CAP aerosol layer during PCAPS almost daily, except for periods where surface-based convection was occurring. Different wave events took different shapes, with long or short wavelengths and symmetrical or asymmetrical shapes. The types of waves visible depend on the time period and depth plotted. Larger scale waves have smaller amplitude to wavelength ratios, making them difficult to observe. Subhour-scale waves are consistently observed with large amplitude to wavelength ratios, which makes them more visible on most plots less than 24 hours. For this reason, it is sometimes difficult to use ceilometer backscatter profiles to identify longer-wavelength waves.

### 5.5.2 Analyzing the frequency of oscillations

Quantitative analysis of oscillations visible in ceilometer backscatter profiles can be obtained using spectral analysis via Fourier decomposition. Determining the major frequency contributions can help to isolate dominant physical processes producing the oscillations.

Two methods are used to analyze the spectral components of waves observed in backscatter. The first uses the time-height of $\log_{10}$ backscatter values, by analyzing the variation of backscatter values through time at a specific height (white lines in Figure 5.11 (a)). This method, referred to as the backscatter method, was used by Cooper et al. (2006) to compare with the spectral pattern of the vertical velocity ($w$) measured at the surface. This confirmed that oscillations were coupled throughout the depth of the stable layer. The second method uses backscatter isopleths to produce a time series of wave height, from which frequency components of the wave are computed (black lines in Figure 5.11 (a)). The computed power spectrum for the isopleth method is shown in Figure 5.11 (b) and the power spectrum for the backscatter method is shown in Figure 5.11 (c).

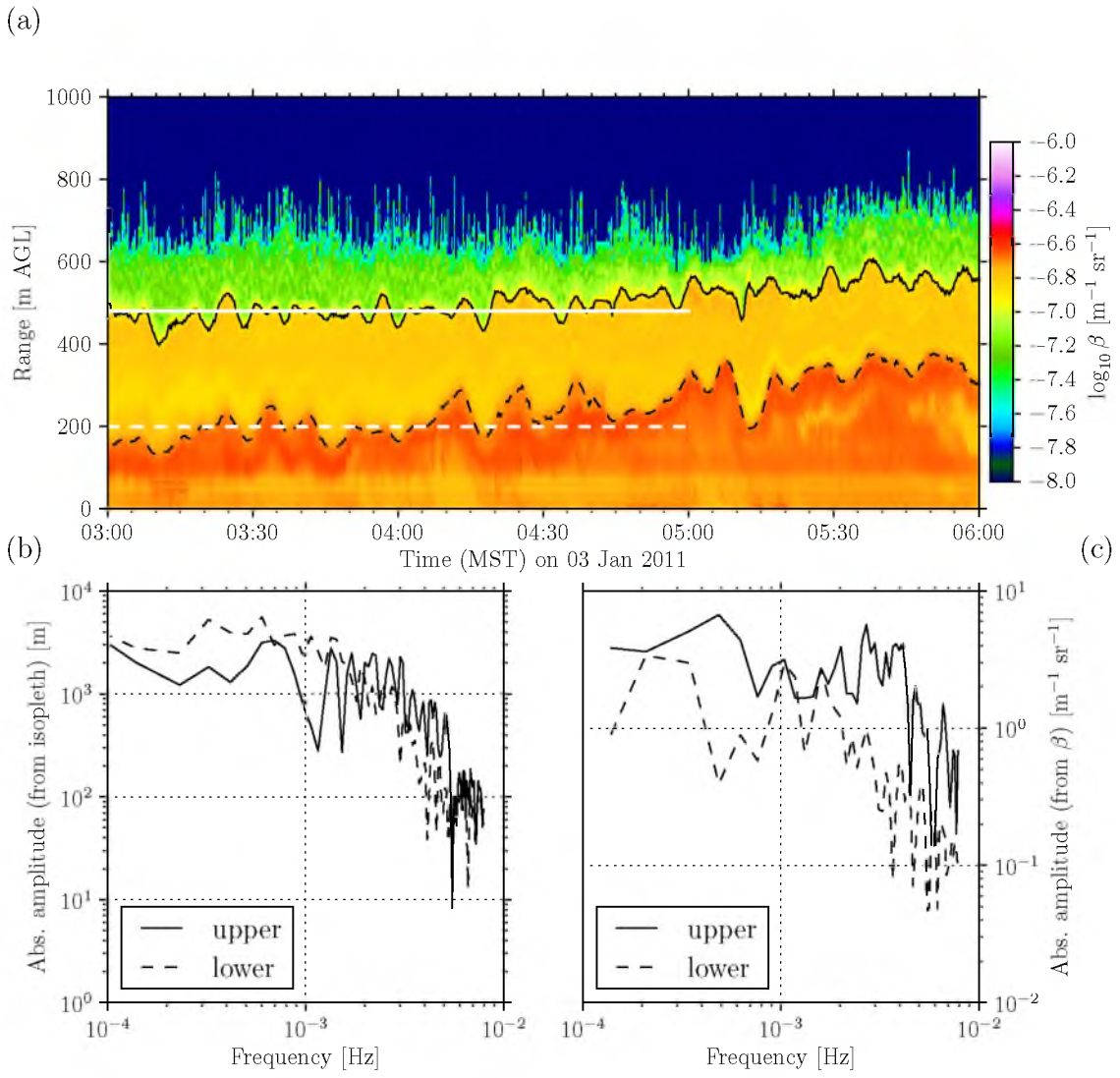


**Figure 5.11**. Waves seen in multiple layers of ceilometer backscatter during a CAP. (a) demonstrates the backscatter coefficient time-height plot, with black solid and dashed lines showing isopleths associated with the observed waves. The solid black line follows an isopleth of -6.9 $m^{-1}$ $sr^{-1}$ and the dashed black line follows an isopleth of -6.7 $m^{-1}$ $sr^{-1}$. The white solid and dashed lines in Figure (a) indicate the height and time period used to compute the backscatter power spectrum. Figure (b) shows the power spectrum of the black dashed and solid lines. (c) shows the power spectrum from the dashed and solid white lines.

The isopleth and backscatter methods produce differently shaped wave power spectra, but the dominant frequency characteristics and the difference between the high and low altitude waves are similar for the two methods. Figures 5.11 (b) and (c) show that the peak frequency for the lower altitude oscillation is lower than that of the upper altitude oscillation. Thus, the lower altitude layer is oscillating slower than the higher altitude layer. The turbulence that forced the upper wave (note the minimal shear present above the aerosol layer in Figure 5.10(b)) decays as it is transported lower into the CAP layer. This effect is likely modified or enhanced by the airmass stratification within the CAP layer, and the inherent density differences of individual layers.

#### 5.5.2.1 Waves and stability

The frequency of internal gravity wave oscillations is governed by atmospheric stability. Greater stability produces a stronger restoring force, and faster oscillations. The frequency of the oscillations is given by the Brunt-Väisälä frequency ($N$), where

$$N^2 = \frac{g}{\theta}\frac{\partial \theta}{\partial z} = g\frac{\partial \ln \theta}{\partial z}. \tag{5.1}$$

When perturbed, the top of a stable layer oscillates as a gravity wave on the boundary between air masses of slightly different densities. Waves may also be produced internally within the stable layer by a variety of mechanisms that produce perturbations, such as vertical wind shear, convection, downdrafts, circulations produced by differential sidewall heating, seiches, and wave interactions. This large variety of processes causing the perturbations complicates the relationship between the actual oscillation frequency and the theoretical frequency $N$. In some situations (e.g., Figure 5.11), the observed and theoretical frequencies correspond well. In other cases where there are multiple processes producing perturbations, a range of oscillations frequencies is produced.

The relationship between vertically-separated waves in a stratified CAP are important. In some cases, the difference in waves appears to be governed by stability. In this situation, the upper wave provides a perturbation to the lower wave, which then oscillates primarily as an internal gravity wave, with a mostly independent frequency governed by the stability at the point of oscillation. In Figure 5.11 (a), two distinct layers are oscillating. If it is assumed that the lower oscillation is forced from the upper level, then the intermediate layers may also be oscillating. This is seen in the slight variations in aerosol scatter throughout the orange layer between the two contoured lines. This means that when using aerosol backscatter, waves can be difficult to detect when gradients are absent. However, because aerosol gradients often correspond to layers of heightened stability, oscillations should occur

primarily at levels where aerosol gradients are present, and will be less frequent in more neutrally-buoyant isotropic aerosol layers. In situations where stratification is stronger, such as where the individual CAP layers are thinner than the amplitude of oscillation, the approximation of stacked, stratified, independent internal gravity waves is invalid, as waves in different stratified layers are directly perturbing others. This, and the density and stability differences between these layers, may contribute to how highly stratified waves appear to dampen or mix quickly.

Thus, the waves observed in CAPs are controlled by three independent influences: the perturbing force, the stability of stratified layers, and wave interactions. Multiple perturbing forces may occur simultaneously, such as differential sidewall heating and wind shear, which make attribution difficult. Stability is the primary driver of wave dampening. The spatial information of available datasets is insufficient to determine the influence of multiwave interactions, such as additive and destructive effects from waves encountering and reflecting off mountain boundaries, particularly for waves of small length and time scales investigated here.

### 5.5.3 Kelvin-Helmholz waves

Figure 5.10 (c) shows waves formed where wind speed shear is present at the top of the CAP layer. These waves often have the characteristic shape of Kelvin-Helmholz (KH) waves, where air masses of different density and momentum interact, resulting in the stereotypical wave shape seen in Figure 5.12 (b). The forcing behind Kelvin-Helmholz waves is shear between air masses of different densities. Breaking KH waves are sources of turbulent transport of heat and momentum, and can play a role in eroding the tops of CAPs. Pinto et al. (2006), for example, described KH waves formed as a result of a down-valley jet in the SLV that eroded the nocturnal CAP layer.

Remotely sensed KH waves are commonly observed visually at the top of a cloud or fog layer. Houser and Bluestein (2011) show that they can be observed with radar if they are large enough. For turbulence-based remote sensors, such as sodars and radars, the turbulent aspects of the KH wave make them observable and allow their spatial distribution to be visualized. Cloud radars, with higher particle sensitivity and resolution, are able to view cloudy KH waves but have difficulty in observing clear-air KH waves. Since lidar scatters off particles instead of turbulence, the structure of a KH wave is easily observed in regions of high particulate density. Polluted CAP environments have both the large particulate and density gradients and potential for strong shearing that make it possible to observe KH waves.

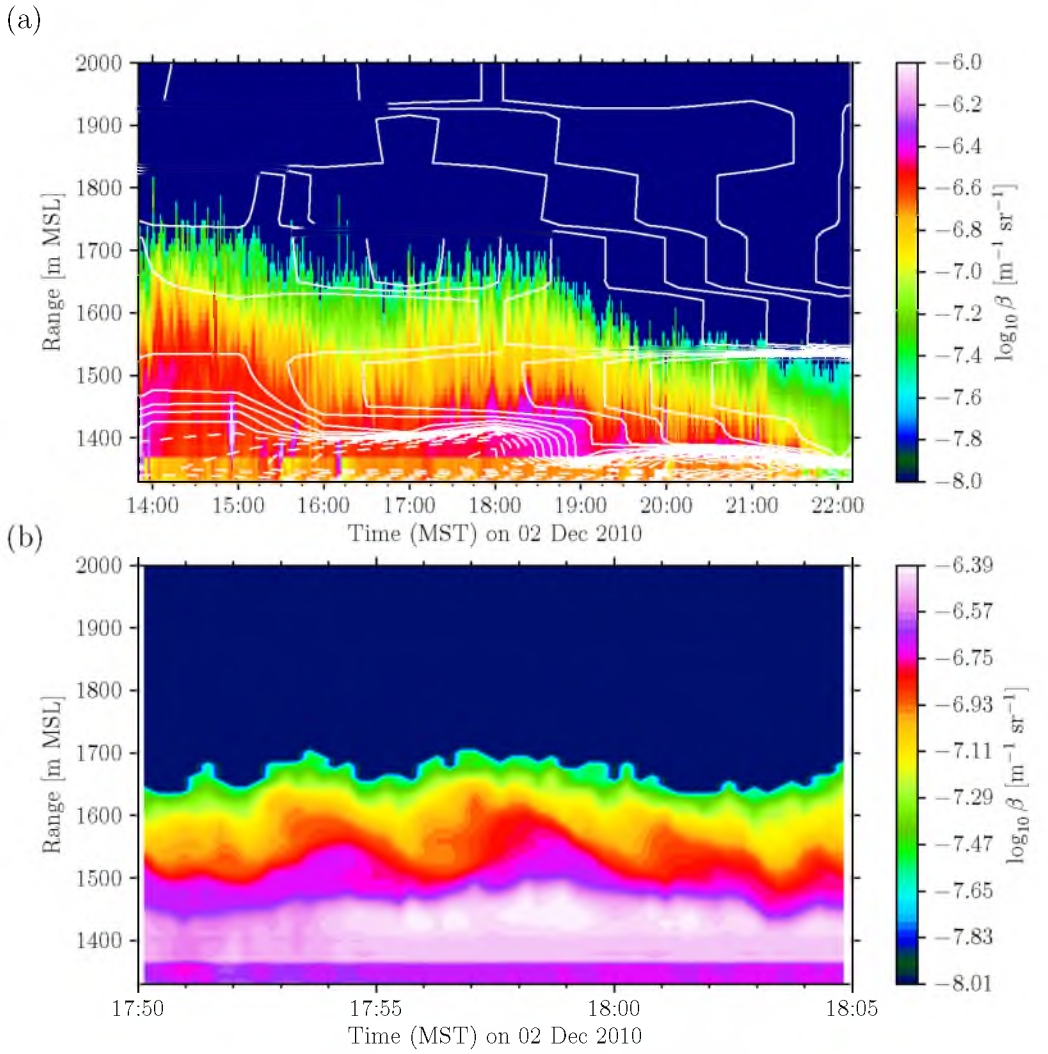


**Figure 5.12**. Ceilometer backscatter visualization of the environment and shape of Kelvin-Helmholz waves observed in a CAP. (a) 6 hours of KH waves associated with a large-scale CAP erosion process. White contours show wind speed shear ($\partial|\vec{V}|/\partial z$). (b) shows a zoomed-in view of the structure of KH waves observed at the top of the turbulently eroding CAP for a shorter time period.

Figure 5.12 depicts the shear and resulting KH waves observed at the top of the CAP layer. Figure 5.12 (a) shows the erosion of a CAP via shear and advection, where the shear, along with density differences between the CAP layer and the free troposphere, induces turbulent KH waves. Figure 5.12 (b) shows a detailed view of the structure of 3 waves from the middle of the period in Figure 5.12 (a) where the tilted asymmetric shape of the waves is clearly seen.

KH waves can be observed both at the top of and within CAP layers. Two different KH examples are shown in Figure 5.13, where Figure 5.13 (a) shows waves at the top of the aerosol layer, while Figure 5.13 (b) shows waves deeper within the layer. The wind shear profile is similar for both cases, where the wind magnitude is indicated by the right-pointing arrows. In Figure 5.13 (a), the wind shear increases within and above the wave layer, which is near the top of the CAP aerosol layer. In Figure 5.13 (b), the wind speed increases for 150 m within the CAP layer, indicating that part of the CAP aerosol layer itself is entrained into the faster moving air aloft. Often, turbulent advection processes entrain the larger scale flow into the CAP layer resulting in advection of the CAP rather than pure erosion and mixing with the larger environment. The apparent frequencies for both waves in Figure 5.13 are approximately 2 to 3 minutes.

Waves of this duration in polluted basins can be seen clearly from 16 second unsmoothed ceilometer backscatter profiles because the air has both sufficient density difference and pollution to be visible in aerosol backscatter. The ceilometer, however, does not provide information regarding the origin of the waves, whether they are forced by a local perturbation from within the CAP, or are a downwind result of terrain effects. In some instances of KH wave occurrence, the shear that causes the waves is associated with a large-scale airmass change, which is both mixing and advecting the layer. Other times, the pressure gradients that induce strong winds and shearing are temporary, resulting in partial turbulent erosion of the CAP layer. When this occurs, momentum and ultimately heat energy is added to the CAP layer without mixing out the layer (adding sufficient energy to mix the layer).

When data are plotted in a time-height format, the shape of an asymmetrical structure can be stretched and distorted. Using vertical wind profile measurements, we have computed the spatial distance over which a single wave covers if time is multiplied by the dominant advecting wind speed. This is done in Figure 5.14, where a mean wind speed of 5 m $s^{-1}$ is used to approximate the horizontal distance traveled by the wave as it passed over the ceilometer. This procedure gives an approximation for a spatially accurate, 1:1 visualization of a KH wave. A likely error in this estimate is the shape of the sheared cap of the wave.

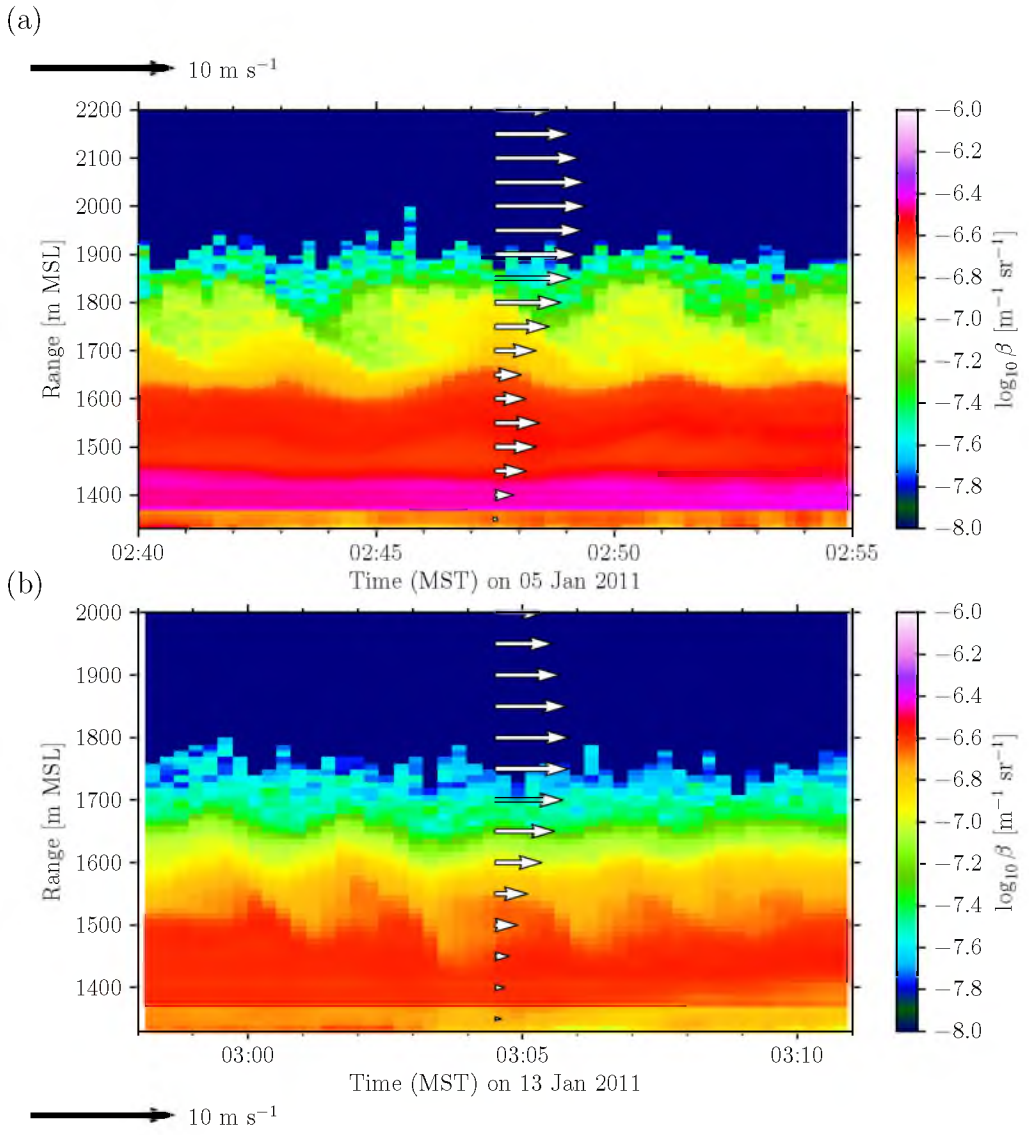


**Figure 5.13**. Illustration of KH waves observed in a CAP layer. (a) shows waves at the top of the aerosol layer, and (b) waves within the aerosol layer. Arrows indicate the $v$ wind component (along-valley), relative to a speed scale at the top and bottom left corners of the figure. Positive (southerly) winds point towards the right.

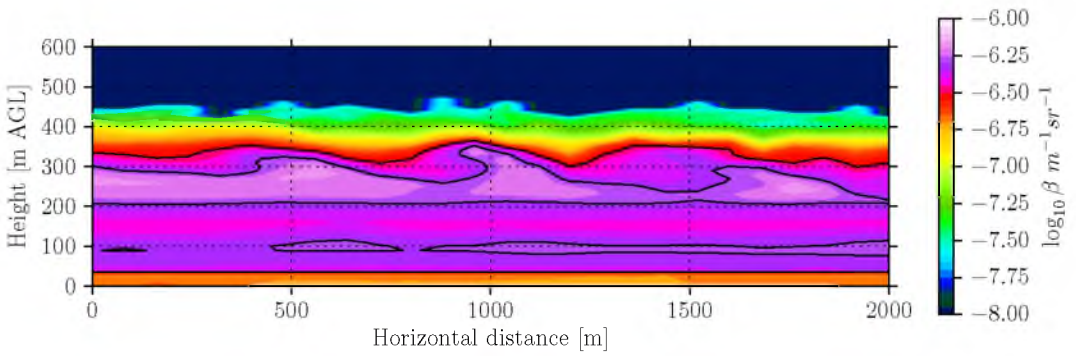


**Figure 5.14**. A depiction of a KH wave converted from time-height units to spatial units by approximating a fixed mean wind velocity over the whole range of values. The waves used are circa 22:30 MST 5 Jan 2011. Black contours of certain ceilometer backscatter values have been added to enhance visibility of wave structures.

While the main structure propagates at a mean speed, the top of a KH wave is inherently moving faster. Thus, this technique likely does not stretch the protruding part of the wave accurately.

The wavelength of this wave is approximately 500 m. This is approximately 1/10 the wavelength of the winter stratiform precipitation KH waves observed in Oklahoma by Houser and Bluestein (2011). The different scale of these CAP KH winds is an indicator of the different airmass interactions and smaller scale processes that govern CAP state. These fine-scale characteristics merit high-resolution observations in both space and time, and a further examination of their energy contributions.

## 5.6 Mixing processes in cold-air pools

The distribution of aerosols provides information on the state of vertical mixing in the boundary layer. Vertical turbulent transport or convection will result in a homogeneous distribution of aerosols over some vertical distance, while high stability that will suppress vertical motion and mixing will result in aerosol layering. Therefore, ceilometer backscatter can be used to examine vertical mixing in a PCAP. Persistent cold-air pools owe their longevity to the suppression of vertical mixing, so the expectation is naturally that mixing will be suppressed and the meteorology of PCAPs will differ in important ways from the meteorology of CBLs, where ceilometer analysis techniques were originally developed.

### 5.6.1 Visual examination of mixing types

Figure 5.15 shows examples of the signatures in ceilometer records of various types of mixing processes observed in PCAPs. In each example, the vertical structure of the CAP layer is modified by the apparent mixing processes (or lack thereof). The primary difference between mixing in stable and convective boundary layers is the suppression or lack of surface-based convection. Surface-based convection tends to produce a homogeneous distribution of particulates from the surface up to some capping inversion at the top of the growing CBL. Snow cover and low clouds, often encountered in wintertime CAPs, reduce heating of the ground and development of a CBL. Mixing is affected more strongly in general by shear-generated turbulence and radiative processes. Because the stable atmosphere is persistent, emissions of particulates and their transport in layers play stronger roles in the evolution and structure of the stable air mass.

Figure 5.15 (a) shows an exceptional wintertime period when mixing appears to be driven by heating at the surface and convective overturning such that persistent internal aerosol gradients are not observed. This occurred during daytime with clear skies and minimal

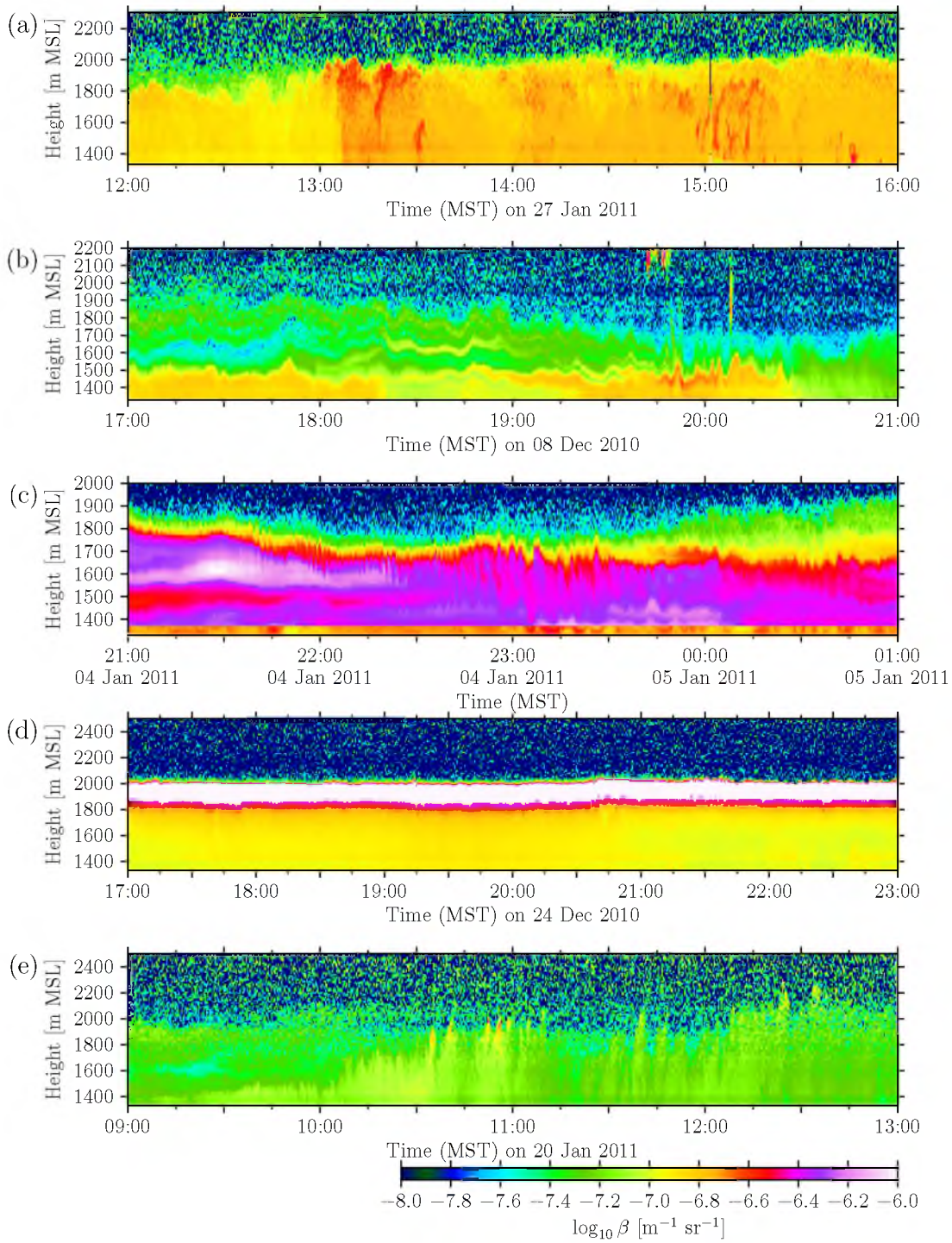


**Figure 5.15**. Depiction of 5 different types of mixing observed by ceilometer during PCAPS. (a) shows convective mixing of the entire CAP layer, while (b) shows strong stratification and no mixing, (c) shows the influence of turbulent erosion from breaking KH waves, and (d) shows a cloud-capped aerosol layer that is well mixed due to processes likely related to the capping stratus cloud layer. Finally, (e) shows convective plumes observed eroding a nocturnal CAP.

snow cover. These events are recognized in the ceilometer backscatter cross-sections by the presence of apparent surface-based convective plumes. A rawinsonde taken at 1515 MST supports this interpretation since a constant potential temperature profile is present through the entire mixed aerosol layer. The strong aerosol backscattering was associated with high relative humidity in the mixed layer. The KSLC sounding did not show the same unstable boundary layer, so this convective mixing is thought to have been localized. During the PCAPS experiment, there were often short lived periods of surface convection on days without cloud cover or snow cover, but they were rarely able to beak through the stable layer containing the aerosols.

Figure 5.15 (b) shows strong stratification within the CAP layer, leading to aerosol layering. Figure 5.15 (b) also shows how quickly these layers can vary, as the influences and causes of such layers are numerous and complex.

Figure 5.15 (c) provides an example of turbulent mixing in a CAP produced by breaking Kelvin-Helmholz waves like those discussed in section 5.5.3. In low-momentum stable atmospheres, turbulence from shear and entrainment governs most mixing within the stable CAP layer. Those processes are usually observed as layering, similar to Figure 5.15 (b). In this case, however, the breaking KH waves produce eddies large enough to produce vertical mixing that is clearly seen in the backscatter cross-section in the upper part of the aerosol layer. The waves are produced by vertical shear of horizontal winds across the density interface at the top of the aerosol layer. These breaking waves produce turbulent erosion at the top of the stable layer. Ultimately, the shear decreases and the KH waves disappear leaving a much more homogeneous (though still stratified) CAP layer. There were no events in PCAPS where turbulent mixing completely erodes a CAP layer except when horizontal advection, usually resulting from an airmass change, is occurring. Thus, the energy contribution from turbulent waves is less than the energy deficit within the CAP layer, which was also found by Zhong et al. (2003).

Figure 5.15 (d) shows the effect on the CAP of stratus clouds that develop within the stable layer. The observations from PCAPS do not provide a clear explanation of the processes that are involved in the mixing observed at these times.

Figure 5.15 (e) shows convective plumes occurring during a low-momentum period (not a CAP). Plumes are seen as vertical columns of homogeneous aerosol. The depth of a plume is usually a function of atmospheric stability and the intensity of turbulence fluxes at the surface. This, like Figure 5.15 (a) shows a feature common to CBLs that is less commonly observed in a CAP.

Mixing in a CAP is governed by radiative, thermodynamic, and dynamic considerations, which makes it difficult to attribute any episode of mixing or stability to any single cause. Certain effects, such as shear-induced turbulent erosion and surface convection, are dominated by single processes, and can be easily observed via ceilometer. The most frequent mixing processes in CAPs are generated by vertical shearing stresses, which are strongly moderated by atmospheric stability. The small amount of mixing that does result is from surface, cloud, and aerosol radiative effects, buoyant forces, and forcing by thermally driven flows produced by the surrounding terrain. These forces are small and combine nonlinearly to create complex variations and interactions at scales not resolved by most available remote sensors.

Information regarding mixing and the forces controlling mixing are relevant to understanding the persistence of CAPs and the surface impacts of a CAP. Vertical distribution of aerosols is relevant to the air quality experienced by residents living in the SLV. The bulk of the pollutants in the SLV are emitted from ground-based sources, so vertical mixing often decreases pollutant concentrations at the ground by mixing pollutants through a deeper mixing volume. Concentrations can increase at the ground, however, if convective plumes growing upwards from the ground encounter an elevated layer of pollutants that are returned to the ground by convective eddies. The growing mixing volume concept, however, is not generally applicable to PCAPs, as the stability restricts vertical motions and mixing. An exception occurs, however, in cloudy CAPs, demonstrated in Figure 5.15 (d). There, processes related to the presence of a cloud at the top of the aerosol layer allow the stable, non-surface-heated layer to remain well mixed up to the level of cloud saturation. The generation of gravity waves causes pollutant layers to oscillate in height, but produces little mixing of the layers unless the waves break, as illustrated for KH instability (Figure 5.15 (b)). Vertical wind shear is another mechanism that can disperse aerosols throughout the PCAP through the generation of turbulent eddies. Another pollutant dispersion mechanism often seen near the end of CAP episodes is simply the advection of pollutants from the valley by increasing winds. Further studies of the aerosol mixing processes will be enhanced by use of ceilometer data, combined with data from other in-situ and remote sensors.

### 5.6.2 Objective mixing detection

The previous section subjectively examined CAP mixing by looking at aerosol backscatter profiles during a variety of mixing situations. Vertical mixing was evaluated by considering the amount of vertical aerosol homogeneity observed within the AL in the ceilometer backscatter profiles. In this section, we attempt to objectively quantify the amount of

aerosol mixing using aerosol backscatter data.

Two methods of evaluating mixing are tested. First, the coefficient of variation (standard deviation divided by the mean) of $\log_{10}\beta$ is calculated from the surface to the top of the AL, where the top of the layer is determined objectively using the threshold method. Individual values of $\log_{10}\beta$ are available from each of the 10-m range gates from the surface to the top of the AL, providing a number of values from which a mean and standard deviation can be calculated for each profile taken at 16-s intervals. A poorly mixed AL will have high values of the coefficient of variation. Second, local maxima in the $\log_{10}\beta$ gradients from the surface to the top of the AL are identified using the gradient method (section 5.4.2). Local gradient maxima within the AL identify aerosol layering, an indicator of poor vertical mixing.

The analysis results for the 5 selected events identified in Figure 5.15 are shown in Figure 5.16, where the gray scales represent the computed coefficients of variation and the dots indicate the heights of local gradient maxima. The gray scale is plotted to heights in the subfigures that correspond to the AL depth. Overall, both methods are successful at identifying (b) and (c) as the events where stratification and aerosol layering are most prominent. As expected, periods of aerosol mixing produce light gray shading, especially prominent in (d) and (e). The high-backscatter convection period in (a) exhibits a higher coefficient of variation because of a lower aerosol concentration at the top of the AL at the beginning of the period, resulting in a step change in backscatter before 1300 MST. Figure 5.16 (b) is highly stratified, particularly between 1830 and 1930 MST. The analyses identified stratification in (c) except for the period where waves were breaking and mixing the entire AL, between 2240 and 2320 MST

The backscatter gradient mixing detection method worked well for the highly stratified period seen in Figures 5.15/5.16 (b). It also worked well in the turbulent mixing case of Figures 5.15/5.16 (c), showing stratification except for the period where waves were breaking and mixing the entire AL between 2240 and 2320 MST. However, when an aerosol sublayer was below 150 m AGL, the gradient method did not identify the sublayer, as is seen in (c). When a strong gradient is detected in the lowest layers of the CAP, it may be an indicator of a shallow CBL growing at the base of the CAP. Figures 5.15/5.16 (b), (c) and (d) were all after sunset, so no CBLs were present in this analysis. Because it is difficult to observe regions in the lower range gates of the lidar, a shallow CBL must be more than about 150-200 m deep and show a sufficiently different backscatter signature to be reliably detected.

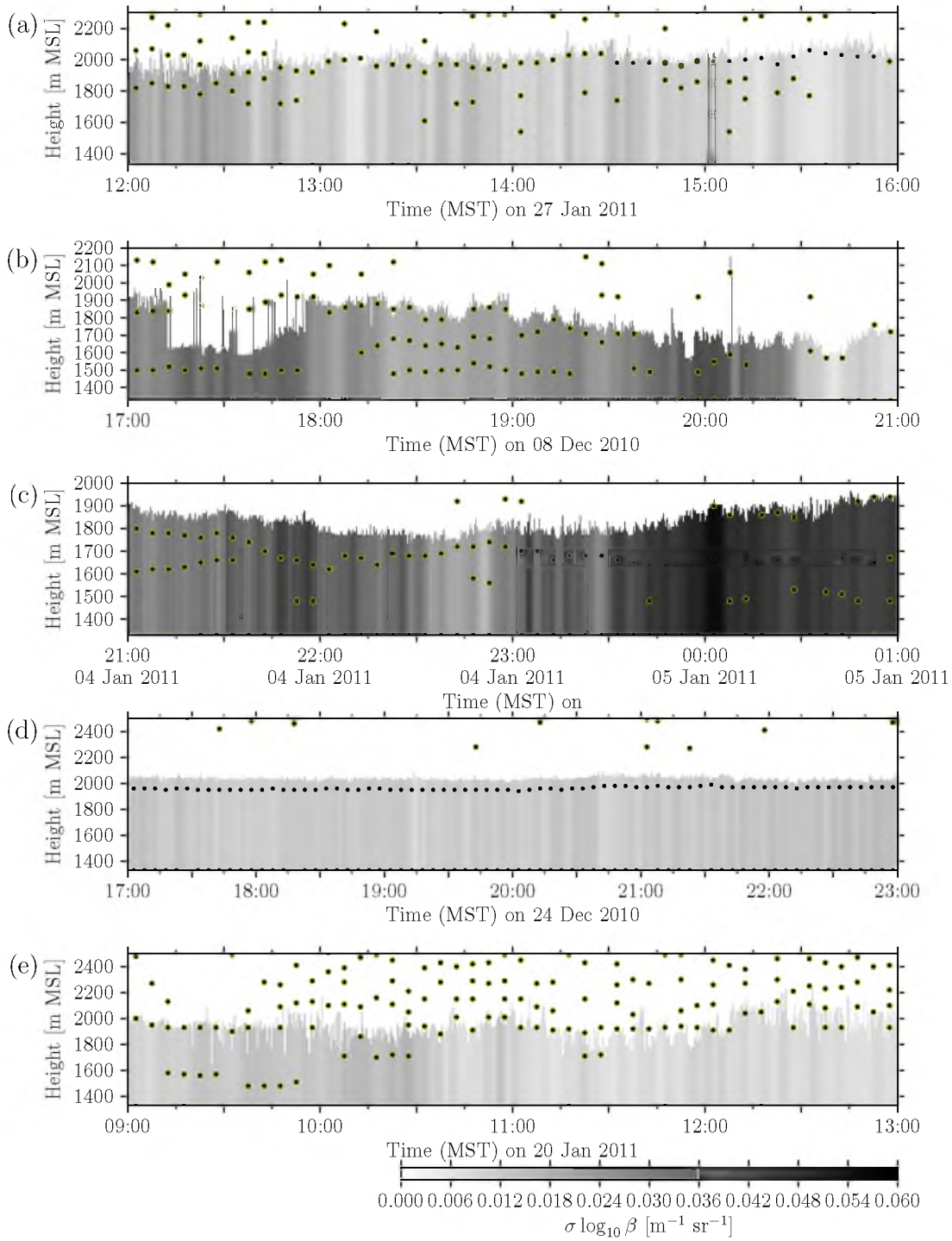


**Figure 5.16**. Examples of automated CAP mixing characterization based on aerosol layer normalized $\log_{10} \beta$ standard deviations or detected gradients in the aerosol field. The periods plotted correspond to those in Figure 5.15. Mixing is determined by aerosol homogeneity, and homogeneity of aerosols can be seen either in the computation of backscatter variance within the AL, or in sharp changes in aerosol backscatter within the AL.

The two objective mixing detection methods, the coefficient of variation and gradient methods, are generally successful in separating well-mixed and stratified periods within events and between events, quantifying the relative amount and location of mixing.

## 5.7 Overlaying ceilometer observations with other datasets

Ceilometer backscatter cross-sections provide useful visualizations of fine-scale aerosol features and clouds. In this section, we combine ceilometer cross-sections with overlays of other meteorological data to assist with more detailed analyses. Basic state variables such as temperature, moisture, and winds can be overlaid, as well as derived variables and modeled and gridded variables. As we have developed the capability of making ceilometer cross-sections, other students and colleagues have found these to be useful base figures for overlays that assist with their PCAPS analyses.

The PCAPS field program measured atmospheric state using rawinsondes and remote sensors. Potential temperature data from rawinsondes was already used to illustrate this overlay technique in Figure 5.1. The reader is referred back to this figure, which illustrates the relationship between backscatter and atmospheric stability during a PCAP episode. An interesting relationship was immediately apparent between gradients in $\beta$ and gradients in $\theta$, showing that high stability layers or temperature jumps occurred at the tops of significant aerosol sublayers and at the top of the AL. The threshold method was used to determine the AL top, which is the height where the -7.6 $m^{-1}$ $sr^{-1}$ was encountered. The tops of aerosol sublayers within the AL also were associated with local increases in potential temperature gradients, especially in the 0115 and 0415 MST soundings. This characteristic small stable layer is observed at all times a rawinsonde crossed a reasonably strong aerosol gradient. Aerosols tended to be better mixed vertically in layers where the stability was weak (for example, the 0115 MST sounding from the surface to 1600 m MSL).

In this section, we extend our earlier analyses to look at another event, combining the ceilometer backscatter cross-section with radiosonde potential temperature ($\theta$) and mixing ratio ($w$) soundings from a sequence of 12 rawinsondes on 2-4 January 2011 (Figure 5.17). The potential temperature soundings are yellow and the mixing ratio lines are green. A threshold analysis of aerosol depth (quasi-horizontal purple line) and hand analyses of the temporal variation in heights of a subsidence inversion (red line) and the valley stable layer or inversion (yellow line) were added to this figure. This event also included altostratus clouds above the valley. Virga fell into the upper valley atmosphere from these clouds from 2000 MST 2 January through 1100 MST 3 January and between 2200 on 3 January and

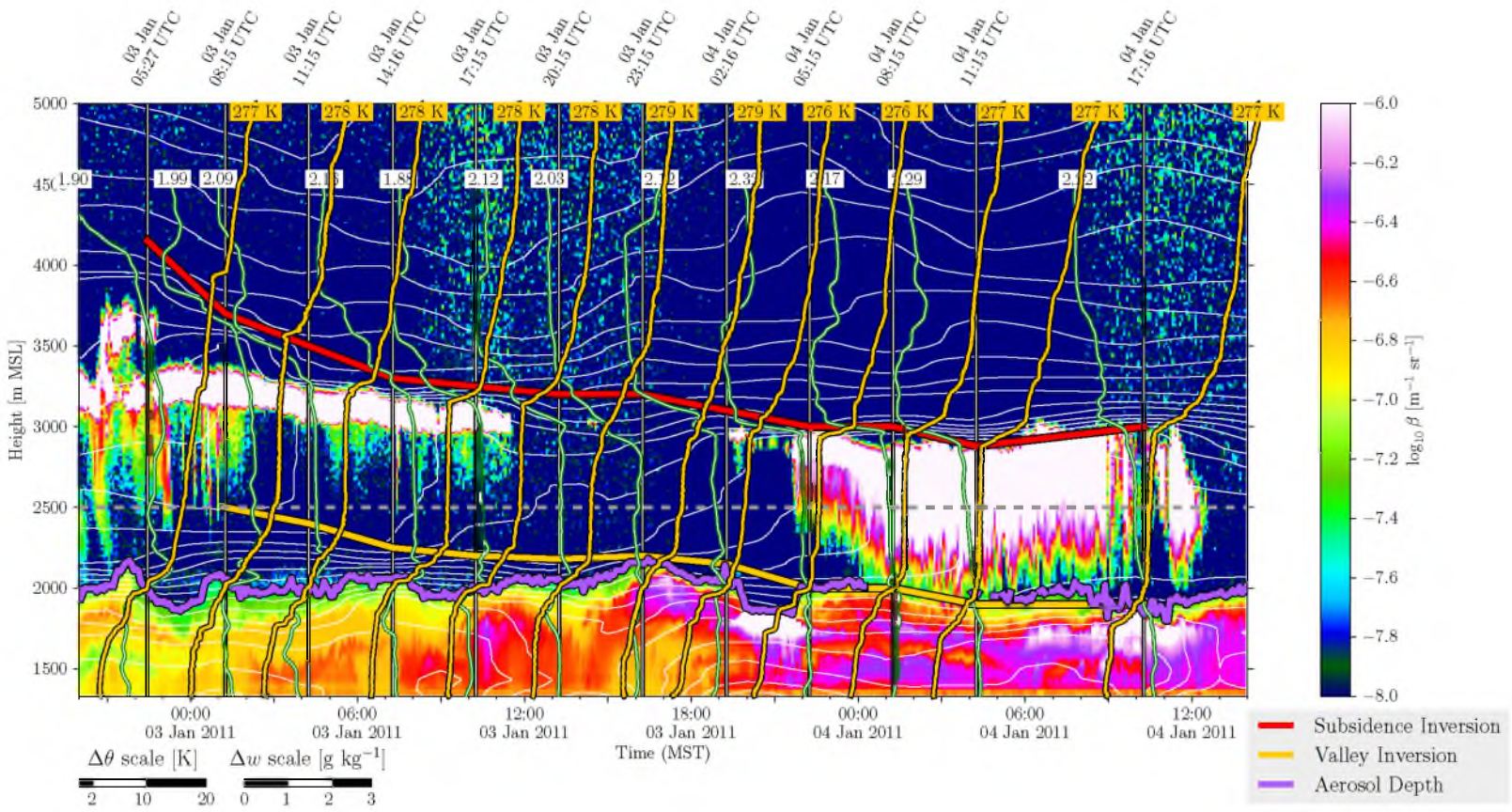


**Figure 5.17**. Ceilometer backscatter overlaid with thermodynamic soundings and subjective layer boundaries, demonstrating the value of adding ceilometer particle backscatter to high-frequency rawinsonde profiles. Profiles are shown as vertical white lines, yellow lines indicating potential temperature (with the surface $\theta$ shown at the top of the figure), and green lines showing mixing ratio $w$. Sounding times in UTC are shown above the corresponding black/white line. Subjectively drawn contours indicate the large-scale subsidence inversion (thick red line), valley inversion (thick yellow line), and the top of the aerosol layer (thick purple line). To assist in interpretation, potential temperatures from the PCAPS time-height dataset (section 4.4.3) have been contoured in white.

1200 MST on 4 January. Low stratus clouds formed within the valley aerosol layer at its top in the late evening of 3 January and from 0600 MST to noon on 4 January. Clouds are visualized in white. The ridgeline height of the Oquirrh Mountains on the west side of the valley is shown as a horizontal dashed line at 2500 m MSL, and white contours are lines of constant potential temperature from the PCAPS time-height data set developed by PhD student Neil Lareau.

The relationship between potential temperature structure and backscatter variations is similar to that seen in Figure 5.1, where potential temperature gradient maxima tend to occur at the same heights as $\log_{10}\beta$ gradient minima. In other words, thin high-stability layers or jumps in potential temperature occur at the tops of aerosol layers. As with periods of cloud-capped aerosol layers, the observations from PCAPS were not focused on observing fine-scale fluctuations and forces from above the surface layer. Additionally, all quality-control processes on rawinsondes smooth the temperature profiles, and remove any trace of these stable layers. As a result, information regarding the causes and relationships between stability and aerosol layering cannot be determined from the observational dataset alone. This stable-layer relationship has a practical implication, however: weak stable layers observed with radiosondes from within a polluted CAP can be used as an independent measure of the depth of an aerosol layer or the height of aerosol sublayers.

During the period of interest, a large-scale subsidence inversion, associated with atmospheric warming and drying, descended from midtropospheric levels to 2900 m MSL. Altostratus formed at the base of this inversion, although they dissipated briefly from midday to the evening of 3 January. At this time, the subsidence inversion strengthened and the altostratus layer reformed, producing a 14-hour-long period of virga, which descended into the valley, occasionally reaching as low as the top of the AL. Virga is a difficult phenomenon to observe without using lidar or cloud radar, so its observation with a ceilometer can be beneficial to understanding atmospheric influences on CAPs.

The top of the valley inversion, contoured as a thick yellow line, is considered to be the primary stable layer associated with the PCAP in the valley. This stable layer extended upward to levels near the Oquirrh Mountain ridgetops early in the period, well above the aerosol layer, but descended slowly and only converged with the AL top by the late evening of 3 January. This illustrates that valley inversion and aerosol layer depths differ. It is often assumed by others that the two terms are synonymous; this erroneous concept probably comes from the close correspondence between aerosol depths and mixing layer heights in unstable boundary layers, where the base of an elevated inversion caps the vertical dispersion

of pollutants in the underlying convective boundary layer. It is often the case that the aerosol layer forms in the lower levels of the deeper valley inversion or stable layer.

The potential temperature and mixing ratio profiles are quite interesting. The aerosol layer is generally weakly stable, except during midday on 3 January when convection mixes the aerosols to a depth of 500 m and near 10:30 am on 4 January when virga fell from a cloud that formed within the AL and the near-surface air warmed. There is much variation in mixing ratio from time to time and in the vertical within the valley inversion, exhibiting the layering that is often also seen in potential temperature profiles. A subcloud layer extends downward from the altostratus cloud deck to the top of the valley inversion and this layer maintains a moist adiabatic lapse rate and exhibits good vertical mixing of moisture.

The value of ceilometer time-height cross-sections of backscatter coefficients in the analyses of Figures 5.1 and 5.17 comes both from the increased time resolution of the ceilometer data compared to supporting data and from the depiction of the evolution of aerosol and hydrometeor distributions that are closely related to other atmospheric variables. In the next section, we will extend these overlay analyses further to gain a broader view of the meteorology of the entire PCAPS experimental period.

## 5.8 Overview of the PCAPS experimental period

An overview of the PCAPS experimental period is given in Figure 5.18, showing the variations with time of the aerosol layer depth, the valley heat deficit, the occurrence of clouds, fog, precipitation, and virga, average ceilometer backscatter through the aerosol layer, and surface $PM_{10}$ concentrations. The ceilometer backscatter, potential temperature, and wind speed data on which this overview figure is based is shown in more highly resolved weekly plots in the Appendix. In the next sections, the variations of these variables over the experimental period will be examined, with special emphasis on periods when cold-air pools were present in the Salt Lake Valley.

### 5.8.1 Quantifying clouds and hydrometeors during PCAPS

Cloud base altitudes are indicated in Figure 5.18 by black dots, while precipitation and fog are indicated by vertical green lines, and virga by purple lines. Clouds and hydrometeors were determined from ceilometer data as areas of very high backscatter, as described in section 5.1.1. To quantify the frequency of clouds and precipitation during PCAPS, the maximum backscatter from the surface to 5 km AGL was computed for every hour of the project. With this dataset, periods when this hourly backscatter maximum exceeded -6

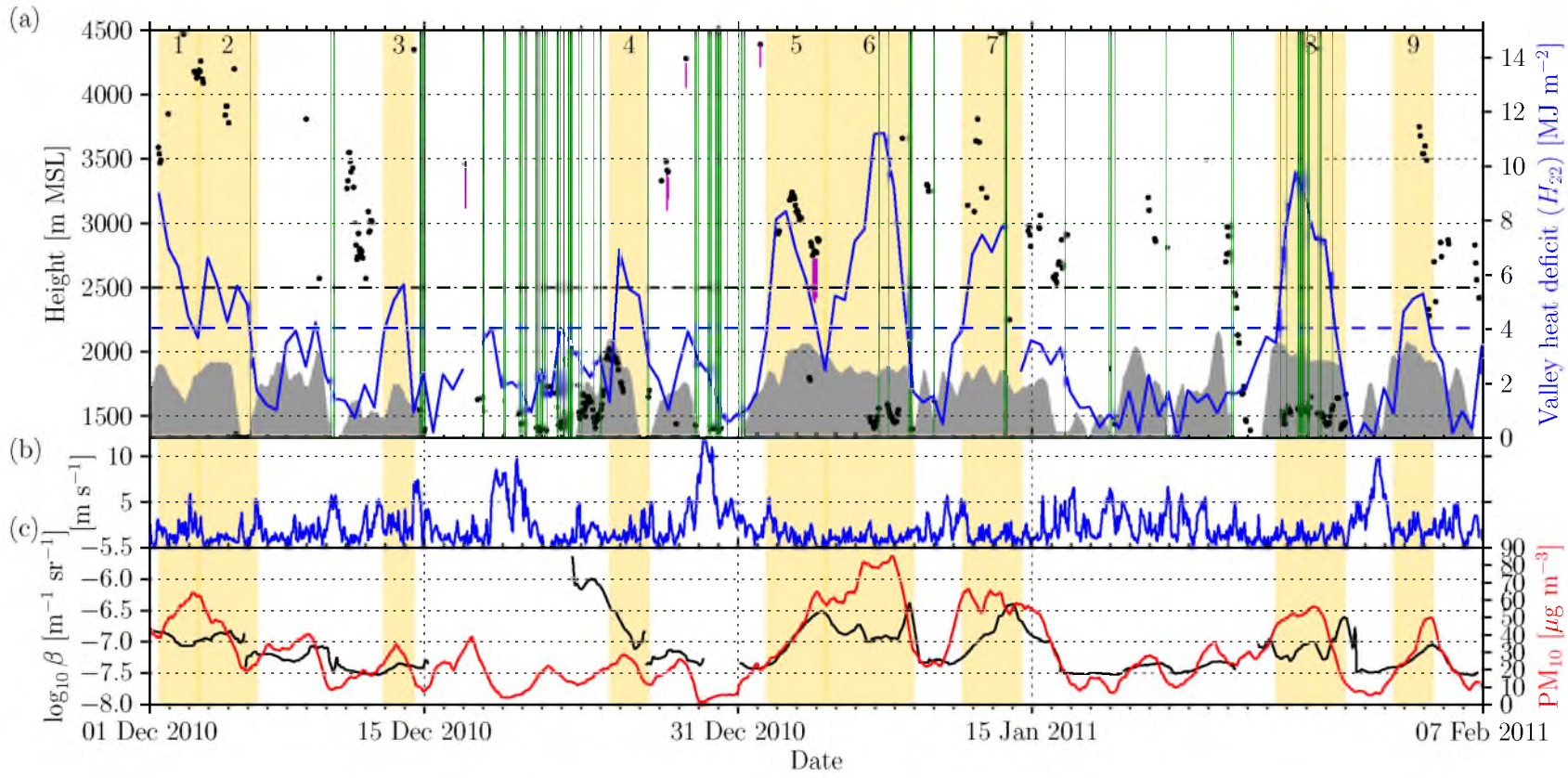


**Figure 5.18**. Meteogram covering the entire PCAPS field period of 1 December 2010 to 7 February 2011 and indicating the 9 $H_{22}$-defined PCAP episodes (yellow rectangles numbered 1 to 9). (a) AL depth from objective and subjective ceilometer backscatter information (gray area), valley heat deficit $H_{22}$ (blue line, a dashed blue line indicates the PCAP $H_{22}$ threshold of 4.04 MJ m$^{-2}$), periods of precipitation or fog from ceilometer (green columns), low-level cloud base heights (from ceilometer, black dots), and virga (from ceilometer, purple lines). The dashed black line indicates the approximate Oquirrh Mountain ridge height on the west side of the valley. (b) One hour running mean of the wind speed at the ceilometer site. (c) 24-hour running mean of AL average $\log_{10}\beta$ (black line), 24-hour running mean of hourly PM$_{10}$ from the Hawthorne Elementary School (red line).

$m^{-1}$ $sr^{-1}$ (the upper limit/white area of all ceilometer plots in this thesis) were considered to have been cloudy or producing precipitation.

For the PCAPS experiment period, 822 hours (of 1884 total hours of ceilometer data) had clouds with bases below 5 km AGL. This corresponds to 44% of the project. When periods with PCAPs were considered (periods where $H_{22} \geq 4.04$ MJ $m^2$ plus or minus six hours from the sounding), 348 of 696 hours, or 50% of the hours had cloud bases below 5 km AGL.

Readers interested in the specific times of clouds and precipitation events are directed to the Appendix to view weekly ceilometer backscatter time-height cross-sections for the PCAPS period. Because clouds and precipitation have complex dynamic (such as eddies and negative convection), thermodynamic, and radiative properties, frequent cloudiness can complicate analysis of CAP events.

Other precipitation-related phenomena such as subcloud evaporation and sublimation were observed during PCAP events with the ceilometer. The potential impacts of these processes are diverse – from the addition of moisture and cold air to the destabilization of the subcloud atmosphere.

### 5.8.2 Aerosol layer depths and their comparison with other air quality and meteorological variables

We have already explored methods to objectively describe the state of the aerosol layer, where section 5.4 explored automated, objective methods of determining gradients and aerosol layer depth, and section 5.6 explored aerosol layer mixing and stratification. Because aerosol layer depth is an important air quality parameter that is resolved so clearly in ceilometer backscatter profiles, we developed an AL depth dataset for the entire PCAPS experimental period.

Aerosol layer depths were calculated using hourly averaged ceilometer backscatter profiles. The resulting dataset consisted of 1884 hour-averaged profiles. The threshold method (section 3.4.2.1) with a threshold of -7.6 $m^{-1}$ $sr^{-1}$ was then used to determine the top of the aerosol layer. This objective method identified the tops of densely polluted layers and the indicated tops of low cloud layers or fogs. Because of lidar beam saturation effects, the indicated tops of low clouds or fogs actually represented the altitude where saturation effects reduced the lidar return to zero. These altitudes would generally underestimate the cloud or aerosol depths. Further, the automated threshold method is incapable of determining a height in periods of very weak pollution concentration or rain.

Because of the numerous complications presented by atmospheric hydrometeors, a man-

ual assessment was performed to modify the resultant objective dataset during periods of clouds or hydrometer saturation. The results are shown in the Appendix, where the figures show hourly values of aerosol layer depths. White dots represent the objective threshold method values, while green dots represent subjectively determined values for aerosol depths during periods with clouds or hydrometeors. The subjective modifications were based on linear interpolations across cloudy periods taking account of potential temperature patterns. Hourly values were considered missing when no AL top could be determined during prolonged periods of precipitation. These hourly values appear as times without any AL depth markers in the appendix figures.

Using the hourly AL depth dataset, we calculated the mean and standard deviation of hourly AL depths for the entire PCAPS period, for the 9 events where $H_{22} \geq 4.04$ MJ $m^{-2}$, and for all events where the 24-hour running mean of the hourly surface $PM_{10}$ concentrations exceeded 20 $\mu$g $m^{-3}$. The results are shown in Table 5.2.

The mean top of the aerosol layer was 1811 m MSL over the whole winter period. This is approximately 500 m above the valley floor. During high stability or pollution events, the mean AL depth was somewhat higher, 1853 and 1861 m MSL, with standard deviations of 135 and 152 m, respectively. The standard deviation was somewhat higher when calculated over the entire winter period because of the higher fraction of low-AL depths, clouds, fogs, and precipitation events in this period.

Beyond simple statistics, we can examine the evolution of the aerosol layer from Figure 5.18, which shows the 12-hour smoothed aerosol layer depth during the entire field project. The plotted dataset omits values for the aerosol layer depth for periods when a 12-hour average AL could not be computed. These are primarily long periods of precipitation or where the aerosol layer depth would be near zero.

The ground-based aerosol layer in the Salt Lake Valley during the winter of 2010-2011 generally extended to heights of about 1850 m MSL, or to about 46% of the valley's depth. The aerosol layer nearly disappears during periods of heavy or prolonged precipitation. Passing storms or fronts with strong winds may temporarily sweep the aerosols out of the valley. This is indicated by the consistency between strong wind speeds in Figure 5.18 (b) and small aerosol depths (Figure 5.18 (a)) and low $PM_{10}$ concentrations (Figure 5.18 (c)). On the other hand, the aerosol layer is present during much of the winter, even during periods of relatively low stability (i.e., periods when $H_{22} < 4.04$ MJ $m^{-2}$) and they can even persist during fog events such as those on 29-30 January, and during light rain events such as those on 13 January. This general consistency in the depth of the AL during the

**Table 5.2**. Aerosol layer averages from the PCAPS field experiment for various periods.

| | Mean AL depth (m MSL) | Standard Deviation | Dataset |
|---|---|---|---|
| Entire PCAPS Period | 1811 | 185 | 1349 hours of 1884 possible hours |
| PCAP Events (9) | 1861 | 135 | 614 hours of 696 possible hours |
| $PM_{10} > 20$ $\mu$g $m^{-3}$ | 1853 | 152 | 907 hours of a possible 1058 hours |

winter, despite the variable meteorology, is somewhat surprising. Further, there is often little variation in AL depth within PCAP events (i.e., when $H_{22} \geq 4.04$ MJ m$^{-2}$), even though there are substantial concurrent variations in the $PM_{10}$ concentrations (see Figure 5.18 (c)). The aerosol layers slowly descend in some events (1, 2, 4, 8, and 9), while rising in others (3 and 5). The AL depth remains nearly constant in events 6 and 7.

Radiative and mixing processes occurring at the tops of low-level clouds that form within the valley and in the subcloud layer do not substantially alter the aerosol layer depths. This is seen particularly during events 6 and 8, where diurnal cloud and fog patterns evolve, but the aerosol layer top remains steady.

While the number of fogs in the winter 2010-2011 data set was limited, it is interesting to see that the fogs tend to occur late in the strongest stability, multiday PCAP periods. These fogs tend to occur at night, and burn off during the daylight hours before becoming reestablished the next night, as can be seen in the Appendix for the 6-7 January and 27-30 January events. Interestingly, the fog formation does not appear to significantly affect the AL depth, as the aerosol layer depths are similar before and after the fogs. Note that our subjective analysis of AL depths generally used linear interpolation across these nighttime fog events.

Prof. Whiteman (personal communication, 2013), in related research, has identified relationships between $H_{22}$, a measure of bulk atmospheric stability within the valley, and $PM_{2.5}$ in which increases in $H_{22}$ above a 4.04 MJ m$^{-2}$ threshold trigger the buildup over multiple days of surface $PM_{2.5}$ concentrations. Figure 5.18 (a) includes this threshold, which can be compared to time-varying $H_{22}$ values. Variations in bulk stability are known to be produced primarily by the passage of large-scale weather systems (Whiteman et al. 1999). This triggering relationship is also seen for $PM_{10}$ in Figure 5.18. The relationship is such that, so long as the bulk stability exceeds the threshold, $PM_{10}$ increases continuously day-by-day despite subsequent oscillations in $H_{22}$ above the threshold. This increase of pollutant concentration suggests that the buildup of bulk stability within the valley plays an important role in causing the air to stagnate within the valley. Otherwise, the pollutants could be advected out of the valley rather than building up within the valley stable layer.

$PM_{10}$ concentrations tended to increase from day-to-day following the exceedance of the heat deficit threshold, but the increase in $PM_{10}$ often started before the threshold (determined on the basis of $PM_{2.5}$ observations) was exceeded. Also, $PM_{10}$ concentrations began to fall well before the cold-air pool (again, based on the $PM_{2.5}$ threshold) ended. While no information was available on the varying primary or secondary $PM_{10}$ emission

rates, there was still a good relationship between stability and $PM_{10}$, suggesting that the emission rates may not vary much from day to day and are thus a secondary factor compared to atmospheric stability. Large temporal variations in $H_{22}$ (Figure 5.18 (a)), however, do not generally produce corresponding changes in aerosol layer depth, suggesting that there is a control on aerosol layer depth and that the surface $PM_{10}$ concentrations increase because of increased aerosol loading within the AL, or trapping of an aerosol sublayer near the ground in the lower part of the aerosol layer. Over the entire winter period, the AL depth appears to be more or less independent of $H_{22}$. Further, a $H_{22}$-AL depth relationship is not apparent within PCAP episodes.

Section 5.3 showed the existence of a linear relationship between 30- to 50-m-averaged $\log_{10}\beta$ and surface $PM_{10}$ concentration at the Hawthorne School, after high humidity and non-CAP events were removed from the analysis. Figure 5.18 (b) shows a similar agreement for the backscatter as averaged throughout the entire (variable depth) AL. This is an important similarity, because it indicates that, to some undetermined degree, surface particulate concentrations relate to the pollution throughout the aerosol layer. In evaluating this relationship, one must exclude cloudy or foggy periods when AL depth is determined subjectively because, in such cases, areas of high backscatter from clouds and fogs are combined with areas of negligible backscatter above the cloud, resulting in artificially low backscatter.

Surface $PM_{10}$ concentrations and average $\log_{10}\beta$ for the aerosol layer vary more or less concurrently throughout the winter period, and both are generally higher during high $H_{22}$ events. During periods when the AL depth has only weak temporal variations, there are often excursions where $PM_{10}$ and $\log_{10}\beta$ deviate from one another. In an idealized convective boundary layer maintaining constant depth, such excursions would not be seen. Pollutants would be instantaneously mixed throughout the convective boundary layer and changes in aerosol loading would be closely related to surface $PM_{10}$ concentrations. In stable boundary layers, on the other hand, differences in surface $PM_{10}$ and aerosol loading would occur if aerosols in the SBL were trapped in layers. Then aerosols could be trapped near the surface or aloft, and $PM_{10}$ concentrations at the surface would deviate from mean aerosol loading within the SBL. The temporal deviation of $PM_{10}$ concentration measurements from $\log_{10}\beta$ in PCAP events may thus reflect the layering of aerosols in the PCAP. This deviation can be observed from a pair of events in the PCAPS data set seen in Figure 5.18. $H_{22}$-defined PCAP 1 sees surface $PM_{10}$ increasing rapidly while AL depth and average aerosol loading remain constant, following a frontal passage. The onset of PCAP 7 also showed strong

layering, and a resulting rapid increase of surface $PM_{10}$, while the corresponding AL depth and mean $\log_{10}\beta$ were relatively slow to change.

As a result of the frequently inconsistent relationship between AL depth and $PM_{10}$, the time variation of surface pollutant concentrations seems minimally controlled by the depth of the aerosol layer. There are periods when AL depth increases concurrently with both decreases and increases in surface $PM_{10}$ concentrations. There are also periods where AL depth decreases are associated with both increase and decreases in surface $PM_{10}$ concentrations. This suggests that turbulent vertical mixing and advection within the aerosol layer play a more important role in governing surface $PM_{10}$ concentrations than the AL depth itself. This is quite different from convective boundary layers, where the growing mixed layer organizes the aerosol distribution and surface concentration of pollutants.

Detailed evaluations of the meteorology of significant individual air pollution events is the next step in gaining a fuller understanding of these events. Such evaluations, being conducted by graduate students and other colleagues, are presently underway using the PCAPS dataset. The highly variable meteorology, which includes both larger-scale (e.g., the movements and passages of high- and low-pressure systems and fronts) and local-scale (precipitation, surface sensible and latent heat fluxes, local thermally driven circulations, lake breezes, canyon flows, etc.) processes and atmospheric chemistry, will play important roles in some of these events, and will not be easily discovered by looking at an overview of the entire winter period, as exemplified in Figure 5.18. A key missing variable in all the analyses so far is the emissions inventory of primary and secondary particulates.

# CHAPTER 6

# SUMMARY AND CONCLUSIONS

This thesis has utilized data from a Vaisala CL-31 lidar ceilometer deployed by the National Center for Atmospheric Research's Earth Observing Laboratory during the PCAPS field meteorological experiment to study persistent wintertime cold-air pools in Utah's Salt Lake Valley.

Data from the CL-31 are archived in encoded files, and Vaisala proprietary software is generally used to access these files to obtain needed metadata, to plot time-height cross-sections of aerosol backscatter coefficients, and to obtain automated estimates of cloud base and boundary layer depths. Analyses of boundary layer properties with ceilometers in general and with this software in particular have focused on determining daytime convective boundary layer depths or mixing depths. This thesis, in contrast, focuses on investigating the utility of ceilometers in gaining knowledge of the structure and evolution of the stable boundary layer in persistent cold-air pools in valleys and basins.

For our analyses, the encoded data files were accessed directly through a computer program that we wrote in the Python programming language. This provided much greater flexibility in data processing and analysis and proved to be extremely useful in providing a base layer of ceilometer backscatter data on which other meteorological data could be overlaid. A special choice of color scale provided good resolution of aerosol backscatter features and gradients in the cross-section plots.

Ceilometer backscatter plots from a site on the valley floor were compared to photographs taken from the valley sidewalls. Only a few photographs were available, but an analysis showed a good correspondence between the depth of the aerosol layer determined from the ceilometer and the depth of the aerosol layer determined visually. Additionally, there was a good correspondence between visual and ceilometer observations of the abruptness of the transition between the surface-based pollution layer and the clean air above.

Previous research has shown that ceilometer backscatter coefficients obtained in the near-ground layer are closely related to nearby surface-based measurements of the ambient

concentrations of $PM_{10}$ aerosols in low-pollution convective boundary layers. The ceilometer in the Salt Lake Valley was 15 km away from the nearest $PM_{10}$ sampling station, but an analysis, nonetheless, showed a log-linear relationship between the backscatter coefficient and hourly measurements of $PM_{10}$, suggesting that particulate air pollutants can be distributed uniformly horizontally throughout the valley in the stable air within the persistent cold-air pool.

Lidar-based methods for automatically detecting mixing layer depth by analyzing aerosol backscatter were applied to PCAPS ceilometer backscatter profiles. Two of the five methods developed for convective boundary layers performed poorly in determining characteristics of stable boundary layers. Three methods, however, were found to reliably identify significant characteristics of CAP aerosol layers. The *threshold method*, proposed by Melfi et al. (1985) provided a reliable measurement of aerosol layer depth using a single backscatter coefficient that represents the boundary between polluted and clear air. A single threshold of -7.6 $m^{-1}$ $sr^{-1}$ performed well throughout the entire winter period of the PCAPS experiment (1 December through 7 February), though the uncalibrated nature of ceilometer backscatter means this value is not expected to hold for other ceilometers or long periods of time. The *idealized profile method* as applied by Steyn et al. (1999) was found to make a similarly reliable measurement of aerosol layer depth and, in addition, proved to be useful in computing a measure of the polluted to clear transition length scale ($\Delta h$). The threshold method however, performed better for aerosol layers less than 200 m in depth. The *gradient method* proved to be a good analytical tool for measuring and quantifying sublayers within the aerosol layer.

High temporal resolution ceilometer backscatter cross-sections revealed oscillations with periodicities of 5 to 20 minutes at the top of and within the persistent cold-air pools. Waves at the top of the layer, internal waves, and shear-induced KH waves were investigated with high time resolution ceilometer data. Methods to quantify waves in backscatter profiles through spectral analysis were used to identify the different frequency components at different levels in the CAP.

Rawinsondes were used to determine the magnitudes of vertical wind shear that produced ceilometer-detected KH waves. The spatial structure of the waves was also investigated by multiplying the time-height cross-section time dimension by the mean observed wind speed to produce an approximate 1:1 spatially accurate image of the KH waves.

The ceilometer data also proved useful in investigating mixing within cold-air pools. Several mixing regimes were described based on the distribution of aerosols and clouds.

Vertical and turbulent exchange of aerosols with overriding clean air could be inferred from the vertical distribution of aerosols in the ceilometer profiles. Two objective mixing determination techniques proved capable of determining the degree of stratification in a CAP layer. Standard deviations of aerosol backscatter provided a useful measure of aerosol homogeneity or mixing in the vertical. Additionally, the number of backscatter gradients within the aerosol layer exceeding a predefined threshold provided a measure of the layering of aerosols within the cold-air pool. Ceilometer analysis provided a substantial amount of information that could be used to supplement data from the in-situ and remote sensing systems that are more conventionally used in complex-terrain research.

By using the automated detection techniques and overlays of rawinsonde sounding datasets, descriptions of aerosol structure and the corresponding vertical structure of atmospheric state variables could be produced for PCAPS subperiods of interest, with thermodynamic and particulate information presenting researchers with significant information.

One of the periods investigated revealed the interaction between large- and local-scale atmospheric processes in cold-air pools. The general evolution of the stable layer is often accompanied by fine-scale stable and aerosol layers that are produced locally. Analysis of one event showed that the top of the surface-based aerosol layer does not necessarily correspond to the top or bottom of the surface-based inversion in a cold-air pool. Comparison of rawinsonde temperature soundings with ceilometer backscatter data showed that clouds which produced a strong ceilometer backscatter signal descended from the midtroposphere at the base of a subsidence inversion. The ceilometer's excellent time resolution tracked the descending cloud base very well and provided much better information on this phenomenon than could be obtained from infrequent rawinsonde soundings. The development of cloud-top cooling was better described by combining cloud-base tracking from ceilometer with temperature profiles from rawinsondes. Relationships were investigated between aerosol layers and stability. Rawinsonde data, when plotted over cross-sections of aerosol backscatter, revealed that thin stable layers often form at the top of aerosol layers and low stratus clouds. The shallow stable layers, while seen in raw rawinsonde temperature sounding data, would be difficult or impossible to detect in smoothed temperature soundings. Because of the correspondence between the thin high-stability layers and the tops of aerosol layers, the aerosol layers tracked by the ceilometer suggest the accuracy of these high-stability layers in unsmoothed soundings. The thin, high-stability layers should be examined with radiative transfer models, to better understand their formation and causation.

Ceilometer backscatter analyses were employed to describe the major aspects of persis-

tent cold-air pools during the entire wintertime PCAPS field study period from 1 December 2010 through 7 February 2011. The ceilometer recordings of aerosol backscatter were used to investigate relationships between AL characteristics and local- and synoptic-scale meteorology. Meteograms depicted the relationships between the altitude of the top of the surface-based aerosol layer, valley heat deficit, mean $\log_{10}$ backscatter within the aerosol layer, surface $PM_{10}$ concentrations measured at Hawthorne School 15 km distant from the ceilometer, precipitation, clouds, and fogs.

The altitude of the top of the surface-based aerosol layer was determined using an objective technique that defined the top as the altitude where $\log_{10}\beta$ dropped below -7.6 $m^{-1}$ $sr^{-1}$. Because the ceilometer laser beam was attenuated strongly by clouds and fogs, it was necessary to subjectively estimate the altitude of the top of the aerosol layer during precipitation, fog, and low-cloud events to arrive at a complete aerosol layer height database. A 12-h running mean determined that the height of the top of the surface-based aerosol layer during the entire winter period was 1811 m with a standard deviation of 185 m. During the 9 PCAP events, the mean height was 1861 m MSL, with a standard deviation of 135 m. Because the valley floor has an altitude of about 1300 m, the aerosol layers have a mean depth on the order of 550 m. This is approximately 46% of the depth of the Salt Lake Valley.

The valley heat deficit, defined in eq. 2.1, was used to determine the presence of stable layers, and ultimately PCAPs within the Salt Lake Valley. The heat deficit was calculated to a height of 2200 m MSL, approximately 300 m below the highest ridges of the Oquirrh Mountains west of the valley. Heat deficits calculated to this height, $H_{22}$, are most closely related to high daily-average $PM_{2.5}$ concentrations measured on the valley floor at Hawthorne School (C. D. Whiteman, pers. comm. 2013). The $H_{22}$ metric and threshold value of 4.04 MJ $m^{-2}$, described in section 4.4.3, are used as a means to define the presence of a PCAP.

The winter of 2010-2011 had extensive cloud cover and frequent precipitation. 44% of the hours in the experimental winter period had clouds below 5 km AGL and there were several episodes in which stratus and stratocumulus or fog formed within valley cold-air pools. Ten intensive observational periods were designated on the basis of cold-air pool forecasts during this winter. Nine events met the persistent cold-air pool criteria (H22 $\geq$ 4.04 MJ $m^{-2}$ for more than 24 hours). 50% of all hours during these PCAP events had clouds below 5 km.

Surface-based aerosol layers were seen throughout most of the winter in the ceilometer

data regardless of bulk atmospheric stability ($H_{22}$), reflecting the continuous emission of particulate pollutants, especially from anthropogenic sources at the valley floor. During brief and light precipitation and virga events, the aerosol layer was rarely removed or noticeably impacted. However, strong precipitation or precipitation lasting more than 12 hours scavenged particulates from the AL, leaving a moist, shallow aerosol layer. High winds associated with frontal passages or passing synoptic-scale weather systems were also associated with shallow and/or weakly polluted aerosol layers. Nighttime fogs sometimes formed after several days of PCAP conditions, generally during periods with very high stability. Fogs did not significantly affect the depth of the aerosol layer, as the aerosol layer depths preceding and following the fog events were usually very similar.

High $PM_{10}$ concentrations in the valley occurred during periods of high atmospheric stability - generally, the higher the stability and the longer the episodes, the higher the $PM_{10}$ concentrations. However, aerosol layers and significant $PM_{10}$ concentrations existed and persisted at lower stability levels. During PCAPs the aerosol layer depth remained surprisingly steady, even though $PM_{10}$ concentrations were variable. The mean $\log_{10}\beta$ in the aerosol layer, a measure of aerosol loading in the layer, varied less than $PM_{10}$ concentrations. Since the aerosol depth also was relatively steady, it is reasonable that variations in $PM_{10}$ concentrations at the ground are produced by ineffective vertical mixing of pollutants resulting in the formation of layering within the ground-based aerosol layer. Such layering is indicated in the more highly time- and height-resolved ceilometer backscatter data. Due to this stratification, the surface pollution concentrations were not strongly influenced by the aerosol layer depth. This is one of the major differences between a stable boundary layer and a well-mixed convective boundary layer, and is important for attempting to understand the cycle of particulates within PCAP environments.

This thesis has reported the first use of ceilometers in observing aerosol layer characteristics in persistent urban cold-air pools. Many of the results from this work have already initiated studies of fine-scale structure, waves, stratification, and pollution within PCAP environments. The methods developed and demonstrated can be extended, and combined with additional data sets to provide more information about cold-air pools. PCAPS data from additional in-situ and remote sensing instruments are available for comparison to the ceilometer data, including surface flux and radiative measurements. Ceilometer deployments have already occurred as a follow-up to our experience in the PCAPS program, with recent deployments of multiple ceilometers in both the Uintah and Salt Lake basins to study additional wintertime persistent cold-air pools.

Though lidar observations of CAPs have been made previously, the ceilometer data from PCAPS provided higher-resolution observations of CAP AL stratification and depth than previous measurements. This work has demonstrated the benefit of small, high-resolution lidars for studying the evolution of particulate layer structure. The analyses applied here could be extended to other remote sensing devices that provide backscatter information, included scanning Doppler lidars, which also provide wind information. The author hopes to follow up on the present work by promoting the establishment of networks of ceilometers for permanent, long-term boundary layer observation.

# APPENDIX

# CEILOMETER BACKSCATTER DURING THE PCAPS FIELD PROGRAM

This appendix contains 5 figures, A.1 to A.5, each showing two weeks of ceilometer backscatter profiles measured during the PCAPS field project. In addition to ceilometer backscatter contours, isentropes are contoured in white, with thick lines every 5 K, isotachs are contoured in gold, with thick lines every 6 m/s. Circles show hourly ceilometer-derived aerosol layer heights, where white circles mean the threshold method was used, and green circles mean the point was defined manually.

To assist in interpreting the figures, PCAPS IOPs and objectively-determined PCAP periods are shown as black and red bars at the top of each figure. The exact times of these episodes are shown in Table 4.1.

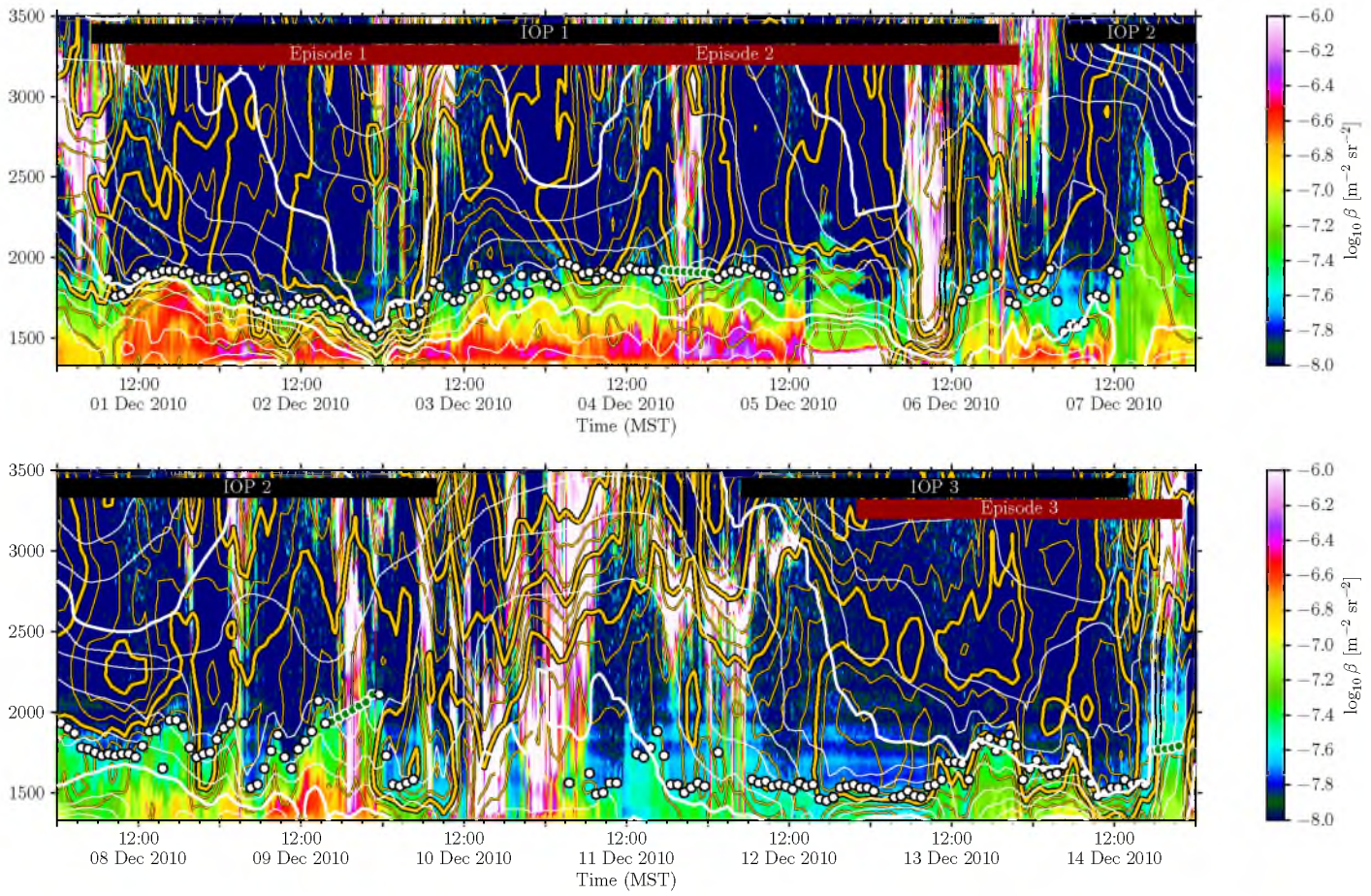


**Figure A.1**. Ceilometer backscatter from the Vaisala CL-31 laser ceilometer used in this research. 01 to 15 December 2010.

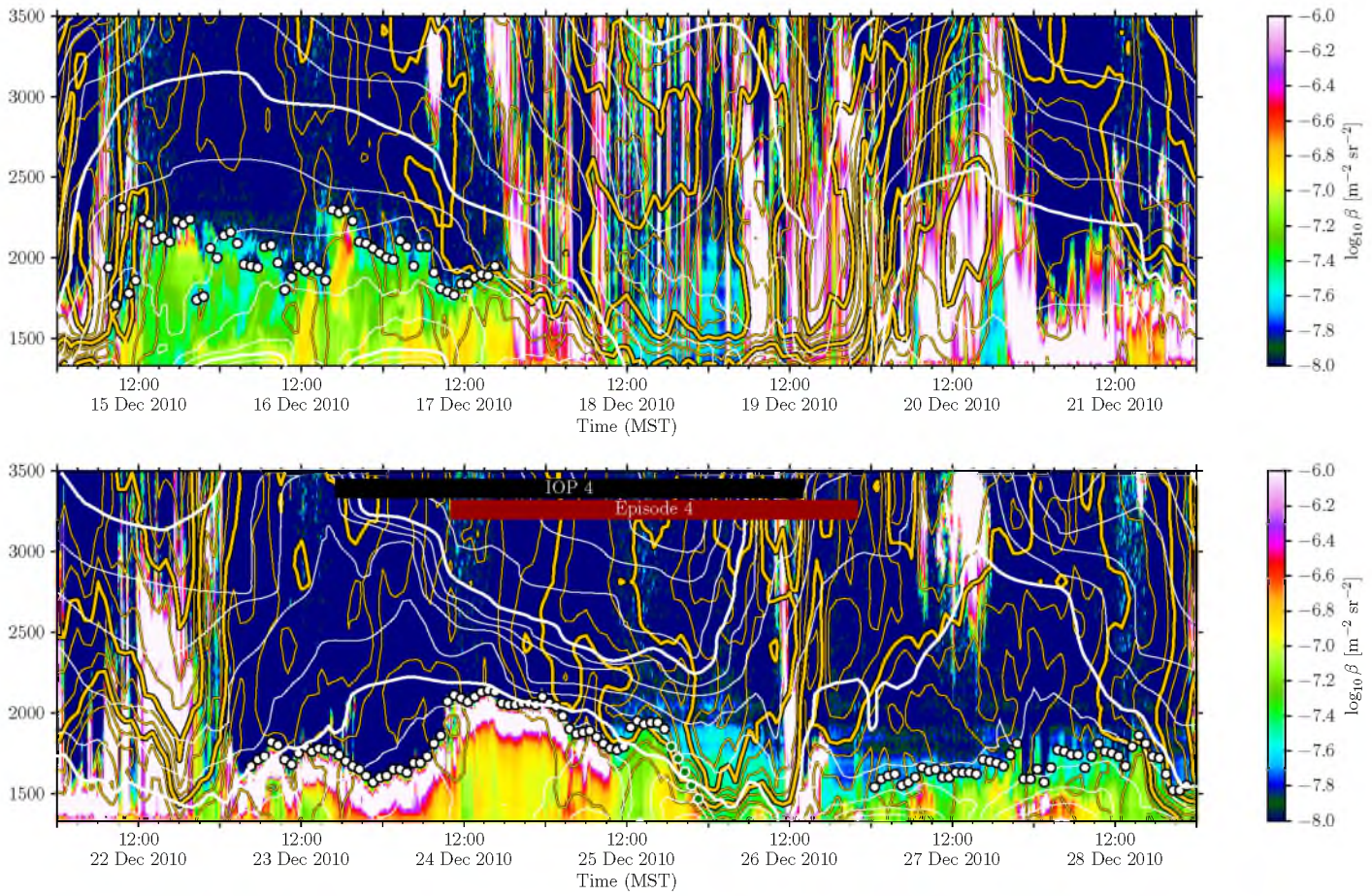


**Figure A.2**. Ceilometer backscatter from the Vaisala CL-31 laser ceilometer used in this research. 15 to 29 December 2010

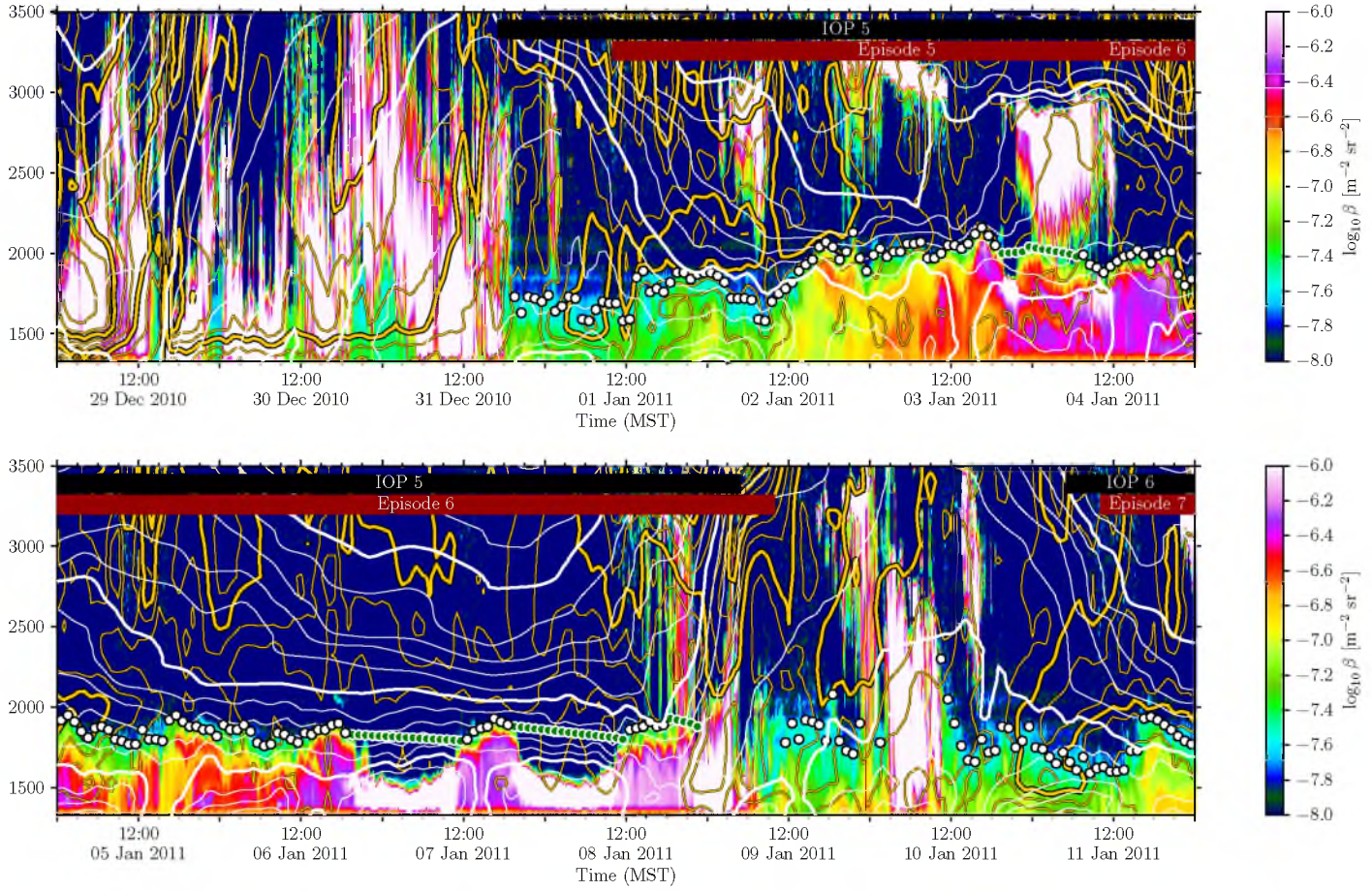


**Figure A.3**. Ceilometer backscatter from the Vaisala CL-31 laser ceilometer used in this research. 29 December 2010 to 12 January 2011

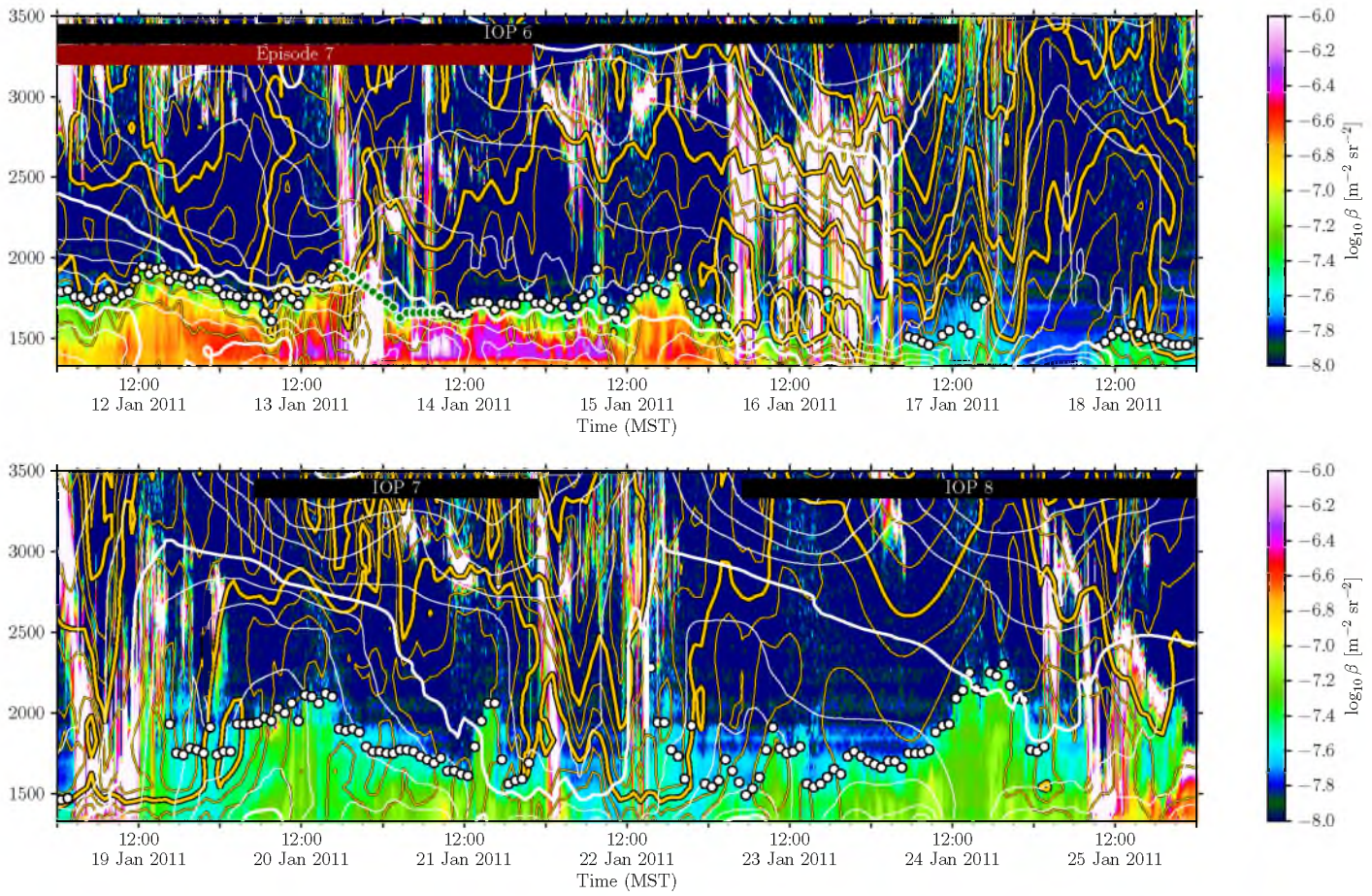


**Figure A.4**. Ceilometer backscatter from the Vaisala CL-31 laser ceilometer used in this research. 12 to 26 January 2011

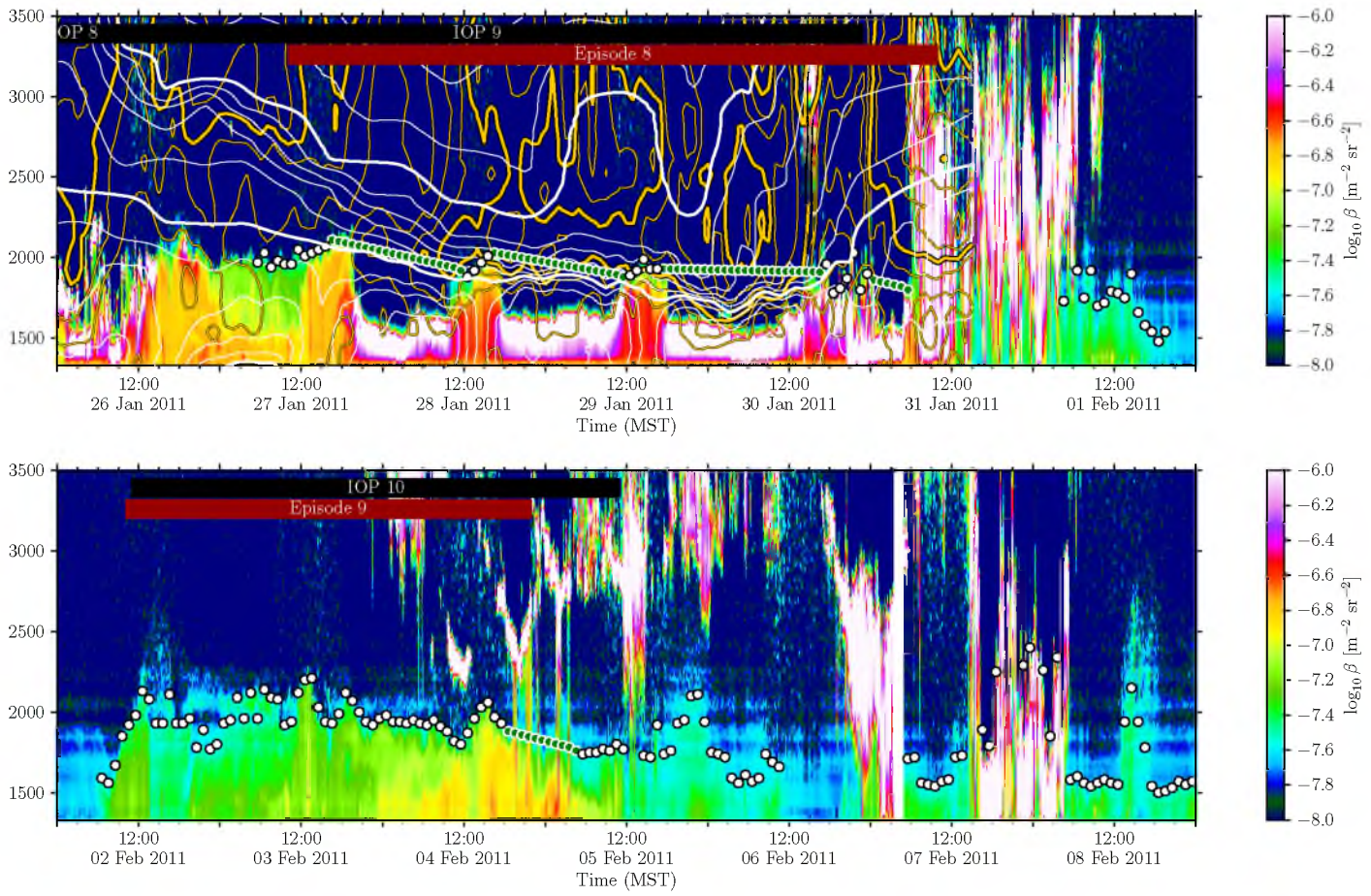


**Figure A.5**. Ceilometer backscatter from the Vaisala CL-31 laser ceilometer used in this research. 26 January to 9 February 2011

# REFERENCES


Antokhin, P. N., et al., 2012: Optik-É AN-30 aircraft laboratory for studies of the atmospheric composition. *J. Atmos. Oceanic Technol.*, **29**, 64–75, doi:10.1175/2011JTECHA1427.1.

Arend, M., B. Gross, C. M. Gan, F. Moshary, Y. Wu, and S. Ahmed, 2010: Inter-comparison of vertical profiling instruments for boundary layer measurements in an urban setting. *15th Symposium on Meteorological Observation and Instrumentation*, Atlanta, GA, City University of New York.

Banta, R. M., L. Darby, and J. Fast, 2004: Nocturnal low-level jet in a mountain basin complex. part I: Evolution and effects on local flows. *J. Appl. Meteor.*, **43**, 1348–1365.

Banta, R. M., L. S. Darby, P. Kaufmann, D. H. Levinson, and C.-J. Zhu, 1999: Wind-flow patterns in the Grand Canyon as revealed by Doppler lidar. *J. Appl. Meteor.*, **38**, 1069–1083, doi:10.1175/1520-0450(1999)038⟨1069:WFPITG⟩2.0.CO;2.

Billings, B., V. Grubišic, and R. Borys, 2006: Maintenance of a mountain valley cold pool: A numerical study. *Mon. Wea. Rev.*, **134**, 2266–2278.

Bissonnette, L. R., 1996: Multiple-scattering lidar equation. *Appl. Optics*, **35**, 6449–6465.

Bodine, D., P. M. Klein, S. C. Arms, and A. Shapiro, 2009: Variability of surface air temperature over gently sloped terrain. *J. Appl. Meteor. Climatol.*, **48**, 1117–1141, doi:10.1175/2009JAMC1933.1.

Brown, W. O. J., S. A. Cohn, B. Lindseth, and J. Jordan, 2011: The NCAR 449 MHz modular wind profiler prototype deployment and future plans. *35th Conf. on Radar Meteorology*, Amer. Meteor. Soc.

Brun, J., P. Shrestha, and A. P. Barros, 2011: Mapping aerosol intrusion in Himalayan valleys using the Moderate Resolution Imaging Spectroradiometer (MODIS) and Cloud–Aerosol Lidar and Infrared Pathfinder Satellite Observation (CALIPSO). *Atmos. Environ.*, **45**, 6382–6392, doi:10.1016/j.atmosenv.2011.08.026.

Burch, J., 1963: Optical research and the solid state laser. *J. Sci. Instrum.*, **40**, 147–152.

Clements, C. B., C. D. Whiteman, and J. D. Horel, 2003: Cold-air-pool structure and evolution in a mountain basin: Peter Sinks, Utah. *J. Appl. Meteor.*, **42**, 752–768.

Cohn, S. A. and W. Angevine, 2000: Boundary layer height and entrainment zone thickness measured by lidars and wind profiling radars. *J. Appl. Meteor.*, **39**, 1233–1247.

Cohn, S. A., W. O. J. Brown, C. L. Martin, M. E. Susedik, G. D. Maclean, and D. B. Parsons, 2001: Clear air boundary layer spaced antenna wind measurement with the Multiple Antenna Profiler (MAPR). *Ann. Geophys.*, **19**, 845–854, doi:10.5194/angeo-19-845-2001.

Cohn, S. A., V. Grubišić, and W. O. J. Brown, 2011: Wind profiler observations of mountain waves and rotors during T-REX. *J. Appl. Meteor. Climatol.*, **50**, 826–843, doi:10.1175/2010JAMC2611.1.

Cohn, S. A., C. L. Holloway, S. P. Oncley, R. J. Doviak, and R. J. Lataitis, 1997: Validation of a UHF spaced antenna wind profiler for high-resolution boundary layer observations. *Radio Sci.*, **32**, 1279–1296, doi:10.1029/97RS00578.

Collis, R., 1966: Lidar: a new atmospheric probe. *Q. J. Roy. Meteorol. Soc.*, **92**, 220–230.

Cooper, D., M. Leclerc, J. Archuleta, R. Coulter, W. Eichinger, C. Kao, and C. Nappo, 2006: Mass exchange in the stable boundary layer by coherent structures. *Agric. Forest Meteorol.*, **136**, 114–131, doi:10.1016/j.agrformet.2004.12.012.

Davis, K. J., N. Gamage, C. R. Hagelberg, C. Kiemle, D. H. Lenschow, and P. P. Sullivan, 2000: An objective method for deriving atmospheric structure from airborne lidar observations. *J. Atmos. Oceanic Technol.*, **17**, 1455–1468.

De Wekker, S. F. J., K. S. Godwin, G. D. Emmitt, and S. Greco, 2012: Airborne Doppler Lidar Measurements of Valley Flows in Complex Coastal Terrain. *J. Appl. Meteor. Climatol.*, **51**, 1558–1574, doi:10.1175/JAMC-D-10-05034.1.

Di Giuseppe, F., A. Riccio, L. Caporaso, G. Bonafé, G. P. Gobbi, and F. Angelini, 2012: Automatic detection of atmospheric boundary layer height using ceilometer backscatter data assisted by a boundary layer model. *Q. J. Roy. Meteorol. Soc.*, **138**, 649–663, doi:10.1002/qj.964.

Doran, J., J. Fast, and J. Horel, 2002: The VTMX 2000 campaign. *Bull. Amer. Meteor. Soc.*, **83**, 537–551.

Dorninger, M., C. D. Whiteman, B. Bica, S. Eisenbach, B. Pospichal, and R. Steinacker, 2011: Meteorological events affecting cold-air pools in a small basin. *J. Appl. Meteor. Climatol.*, **50**, 2223–2234, doi:10.1175/2011JAMC2681.1.

Elterman, L., 1951: The measurement of the stratospheric density distribution of the atmosphere with the searchlight technique. *J. Geophys. Res.*, **56**, 509–520.

Emeis, S., 2011: *Surface-Based Remote Sensing of the Atmospheric Boundary Layer*, Atmospheric and Oceanographic Sciences Library, Vol. 40. Springer.

Emeis, S., C. Jahn, C. Münkel, C. Münsterer, and K. Schäfer, 2007: Multiple atmospheric layering and mixing-layer height in he Inn valley observed by remote sensing. *Meteorol. Z.*, **16**, 415–424, doi:10.1127/0941-2948/2007/0203.

Emeis, S., C. Münkel, S. Vogt, W. J. Müller, and K. Schäfer, 2004: Atmospheric boundary-layer structure from simultaneous SODAR, RASS, and ceilometer measurements. *Atmos. Environ.*, **38**, 273–286, doi:10.1016/j.atmosenv.2003.09.054.

Emeis, S., K. Schäfer, and C. Münkel, 2008a: Long-term observations of the urban mixing-layer height with ceilometers. *14th International Symposium for the Advancement of Boundary Layer Remote Sensing*, Vol. 1, doi:10.1088/1755-1307/1/1/012027.

Emeis, S., K. Schäfer, and C. Münkel, 2009: Observation of the structure of the urban boundary layer with different ceilometers and validation by RASS data. *Meteorol. Z.*, **18**, 149–154, doi:10.1127/0941-2948/2009/0365.

Emeis, S., K. Schäfer, C. Münkel, R. Friedl, and P. Suppan, 2011: Evaluation of the interpretation of ceilometer data with RASS and radiosonde data. *Bound.-Lay. Meteorol.*, **143**, 25–35, doi:10.1007/s10546-011-9604-6.

Emeis, S., K. Schäfer, C. Münkel, and K. Schafer, 2008b: Surface-based remote sensing of the mixing-layer height a review. *Meteorol. Z.*, **17**, 621–630, doi:doi:10.1127/0941-2948/2008/0312.

Eresmaa, N., J. Härkönen, S. M. Joffre, D. M. Schultz, A. Karppinen, and J. Kukkonen, 2012: A three-step method for estimating the mixing height using ceilometer data from the Helsinki Testbed. *J. Appl. Meteor. Climatol.*, **51**, 2172–2187, doi:10.1175/JAMC-D-12-058.1.

Eresmaa, N., A. Karppinen, S. M. Joffre, J. Räsänen, and H. Talvitie, 2005: Mixing height determination by ceilometer. *Atmos. Chem. Phys. Discuss.*, **5**, 12 697–12 722.

Fast, J. and L. Darby, 2004: An evaluation of mesoscale model predictions of down-valley and canyon flows and their consequences using Doppler lidar measurements during VTMX 2000. *J. Appl. Meteor.*, **43**, 420–436.

Fernando, H. J. S. and J. C. Weil, 2010: Whither the stable boundary layer? *Bull. Amer. Meteor. Soc.*, **91**, 1475–1484, doi:10.1175/2010BAMS2770.1.

Franke, K., A. Ansmann, and D. Müller, 2001: One-year observations of particle lidar ratio over the tropical Indian Ocean with Raman lidar. *Geophys. Res. Lett*, **28**, 4559–4562.

Fritts, D. C., D. Goldstein, and T. Lund, 2010: High-resolution numerical studies of stable boundary layer flows in a closed basin: Evolution of steady and oscillatory flows in an axisymmetric Arizona Meteor Crater. *J. Geophys. Res.*, **115**, doi:10.1029/2009JD013359.

Gillies, R. R., S.-Y. Wang, and M. R. Booth, 2010: Atmospheric scale interaction on wintertime Intermountain West low-level inversions. *Wea. Forecasting*, **25**, 1196–1210, doi:10.1175/2010WAF2222380.1.

Godwin, K. S., S. F. J. De Wekker, and G. D. Emmitt, 2012: Retrieving winds in the surface layer over land using an airborne doppler lidar. *J. Atmos. Oceanic Technol.*, **29**, 487–499, doi:10.1175/JTECH-D-11-00139.1.

Grubišić, V., et al., 2008: The Terrain-Induced Rotor Experiment. *Bull. Amer. Meteor. Soc.*, **89**, 1513–1533, doi:10.1175/2008BAMS2487.1.

Grund, C. J., R. M. Banta, J. L. George, J. N. Howell, M. J. Post, R. a. Richter, and A. M. Weickmann, 2001: High-resolution doppler lidar for boundary layer and cloud research. *J. Atmos. Oceanic Technol.*, **18**, 376–393, doi:10.1175/1520-0426(2001)018⟨0376:HRDLFB⟩2.0.CO;2.

Haeffelin, M., et al., 2011: Evaluation of mixing-height retrievals from atuomatic profiling lidars and ceilometers in view of future integrated networks in Europe. *Bound.-Lay. Meteorol.*, **143**, 49–75, doi:10.1007/s10546-011-9643-z.

Haij, M. D., W. Wauben, and H. K. Baltink, 2007: Continuous mixing layer height determination using the LD-40 ceilometer: a feasibility study. Tech. Rep. ISSN 0169-1651 ; WR 2007-01, Royal Netherlands Meteorological Insititute, De Bilt.

Haman, C. L., B. Lefer, and G. a. Morris, 2012: Seasonal variability in the diurnal evolution of the boundary layer in a near-coastal urban environment. *J. Atmos. Oceanic Technol.*, **29**, 697–710, doi:10.1175/JTECH-D-11-00114.1.

Hayden, K., K. Anlauf, R. Hoff, J. Strapp, J. Bottenheim, H. Wiebe, F. Froude, and J. Martin, 1997: The vertical chemical and meteorological structure of the boundary layer in the Lower Fraser Valley during Pacific'93. *Atmos. Environ.*, **3**, 2089–2105.

Heese, B., H. Flentje, D. Althausen, A. Ansmann, and S. Frey, 2010: Ceilometer lidar comparison: backscatter coefficient retrieval and signal-to-noise ratio determination. *Atmos. Meas. Tech.*, **3**, 1763–1770, doi:10.5194/amt-3-1763-2010.

Heinselman, P. L., P. L. Spencer, K. L. Elmore, D. J. Stensrud, R. M. Hluchan, and P. C. Burke, 2009: Radar reflectivity-based estimates of mixed layer depth. *J. Atmos. Oceanic Technol.*, **26**, 229–239, doi:10.1175/2008JTECHA1091.1.

Hill, M., R. Calhoun, H. J. S. Fernando, A. Wieser, A. Dörnbrack, M. Weissmann, G. Mayr, and R. Newsom, 2010: Coplanar Doppler lidar retrieval of rotors from T-REX. *J. Atmos. Sci.*, **67**, 713–729, doi:10.1175/2009JAS3016.1.

Houser, J. L. and H. B. Bluestein, 2011: Polarimetric Doppler radar observations of KelvinHelmholtz waves in a winter storm. *J. Atmos. Sci.*, **68**, 1676–1702, doi:10.1175/2011JAS3566.1.

Hunt, W. H., D. M. Winker, M. A. Vaughan, K. A. Powell, P. L. Lucker, and C. Weimer, 2009: CALIPSO lidar description and performance assessment. *J. Atmos. Oceanic Technol.*, **26**, 1214–1228, doi:10.1175/2009JTECHA1223.1.

Kondo, J., T. Kuwagata, and S. Haginoya, 1989: Heat budget analysis of nocturnal cooling and daytime, heating in a basin. *J. Atmos. Sci.*, **46**, 2917–2933.

Kunkel, K., E. W. Eloranta, and S. Shipley, 1977: Lidar obervations of the convective boundary layer. *J. Appl. Meteor.*, **16**, 1306–1311.

Lareau, N. P., E. Crosman, C. D. Whiteman, J. D. Horel, S. W. Hoch, W. O. J. Brown, and T. W. Horst, 2013: The Persistent Cold-Air Pool Study. *Bull. Amer. Meteor. Soc.*, **94**, 51–63, doi:10.1175/BAMS-D-11-00255.1.

Lehner, M., C. D. Whiteman, and S. W. Hoch, 2011: Diurnal cycle of thermally driven cross-basin winds in Arizona's Meteor Crater. *J. Appl. Meteor. Climatol.*, **50**, 729–744, doi:10.1175/2010JAMC2520.1.

Lindseth, B., 2012: A 449 MHz modular wind profiler radar system. Ph.D. thesis, University of Colorado, 134 pp.

Malek, E., T. Davis, R. S. Martin, and P. J. Silva, 2006: Meteorological and environmental aspects of one of the worst national air pollution episodes (January, 2004) in Logan, Cache Valley, Utah, USA. *Atmos. Res.*, **79**, 108–122, doi:10.1016/j.atmosres.2005.05.003.

Markowicz, K. M., P. J. Flatau, A. E. Kardas, J. Remiszewska, K. Stelmaszczyk, and L. Woeste, 2008: Ceilometer retrieval of the boundary layer vertical aerosol extinction structure. *J. Atmos. Oceanic Technol.*, **25**, 928–944, doi:10.1175/2007JTECHA1016.1.

McKendry, I. G., D. Van Der Kamp, K. B. Strawbridge, A. Christen, and B. Crawford, 2009: Simultaneous observations of boundary-layer aerosol layers with CL31 ceilometer and 1064/532 nm lidar. *Atmos. Environ.*, **43**, 5847–5852, doi:10.1016/j.atmosenv.2009.07.063.

Meissner, P., 1960: Design and operation of the ceilometer computer. Tech. rep., US Department of Commerce, National Bureau of Standards, 71 pp., Washington DC.

Melfi, S. H., J. D. Spinhirne, S.-H. Chou, and S. P. Palm, 1985: Lidar observations of vertically organized convection in the planetary boundary layer over the ocean. *J. Climate Appl. Meteor.*, **24**, 806–821, doi:10.1175/1520-0450(1985)024⟨0806:LOOVOC⟩2.0.CO;2.

Menut, L., C. Flamant, J. Pelon, and P. H. Flamant, 1999: Urban boundary-layer height determination from lidar measurements over the paris area. *Appl. Optics*, **38**, 945–54.

Moran, K. and R. Strauch, 1994: The accuracy of RASS temperature measurements corrected for vertical air motion. *J. Atmos. Oceanic Technol.*, **11**, 995–1001.

Morse, C. S., R. K. Goodrich, and L. B. Cornman, 2002: The NIMA method for improved moment estimation from Doppler spectra. *J. Atmos. Oceanic Technol.*, **19**, 274–295.

Muñoz, R. C. and A. A. Undurraga, 2010: Daytime mixed layer over the Santiago Basin: Description of two years of observations with a lidar ceilometer. *J. Appl. Meteor. Climatol.*, **49**, 1728–1741, doi:10.1175/2010JAMC2347.1.

Münkel, C., S. Emeis, W. J. Mueller, and K. P. Schaefer, 2004: Aerosol concentration measurements with a lidar ceilometer: results of a one year measuring campaign. *SPIE Vol.5235*, K. Schaefer, A. Comeron, M. R. Carleer, and R. H. Picard, Eds., Bellingham, WA, Vol. 5235, 486–496, doi:10.1117/12.511104.

Münkel, C., N. Eresmaa, J. Räsänen, and A. Karppinen, 2007: Retrieval of mixing height and dust concentration with lidar ceilometer. *Bound.-Lay. Meteorol.*, **124**, 117–128, doi: 10.1007/s10546-006-9103-3.

Münkel, C. and R. Roininen, 2010: Unattended automatic monitoring of boundary layer structures with cost effective lidar ceilometers. *Geophys. Res. Abstr.*, **12**.

Ovenden, N. C., S. R. Shaffer, and H. J. S. Fernando, 2009: Impact of meteorological conditions on noise propagation from freeway corridors. *J. Acoust. Soc. Am.*, **126**, 25–35, doi:10.1121/1.3129125.

Parsons, D. B., W. Dabberdt, and H. Cole, 1994: The integrated sounding system: Description and preliminary observations from TOGA COARE. *Bull. Amer. Meteor. Soc.*, **75**, 553–567.

Petkovšek, Z., 1992: Turbulent dissipation of cold air lake in a basin. *Meteorol. Atmos. Phys.*, **47**, 237–245.

Piironen, A. K. and E. W. Eloranta, 1995: Convective boundary layer mean depths and cloud geometrical properties obtained from volume imaging lidar data. *J. Geophys. Res.*, **100**, 25 569–25 576.

Pinto, J. O., D. B. Parsons, W. O. J. Brown, S. A. Cohn, N. Chamberlain, and B. Morley, 2006: Coevolution of down-valley flow and the nocturnal boundary layer in complex terrain. *J. Appl. Meteor. Climatol.*, **45**, 1429–1449.

Pope III, C. A. and D. W. Dockery, 2006: Health effects of fine particulate air pollution: Lines that connect. *J. Air & Waste Manage. Assoc*, **56**, 709–742, doi:10.1080/10473289.2006.10464485.

Porter, J. N., B. R. Lienert, S. K. Sharma, E. Lau, K. Horton, and P. E. T. Al, 2003: Vertical and horizontal aerosol scattering fields over Bellows Beach, Oahu, during the SEAS experiment. *J. Atmos. Oceanic Technol.*, **20**, 1375–1387, doi:10.1175/1520-0426(2003)020⟨1375:VAHASF⟩2.0.CO;2.

Post, M. and W. Neff, 1986: Doppler Lidar measurements of winds in a narrow mountain valley. *Bull. Amer. Meteor. Soc.*, **67**, 264–281, doi:10.1175/1520-0477(1986)067⟨0274:DLMOWI⟩2.0.CO;2.

Price, J. D., et al., 2011: COLPEX: Field and numerical studies over a region of small hills. *Bull. Amer. Meteor. Soc.*, **92**, 1636–1650.

Reagan, J. A., X. Wang, and M. T. Osborn, 2002: Spaceborne lidar calibration from cirrus and molecular backscatter returns. *IEEE T. Geosci. Remote*, **40**, 2285–2290.

Reddy, P., D. Barbarick, and R. Osterburg, 1995: Development of a statistical model for forecasting episodes of visibility degradation in the Denver metropolitan area. *J. Appl. Meteor.*, **34**, 616–625, doi:http://dx.doi.org/10.1175/1520-0450(1995)034⟨0616:DOASMF⟩2.0.CO;2.

Reeves, H. D., K. L. Elmore, G. S. Manikin, and D. J. Stensrud, 2011: Assessment of forecasts during persistent valley cold pools in the Bonneville Basin by the North American Mesoscale Model. *Wea. Forecasting*, **26**, 447–467, doi:10.1175/WAF-D-10-05014.1.

Reeves, H. D. and D. J. Stensrud, 2009: Synoptic-scale flow and valley cold pool evolution in the western United States. *Wea. Forecasting*, **24**, 1625–1643, doi:10.1175/2009WAF2222234.1.

Rogers, R., M.-F. Lamoureux, L. R. Bissonnette, and R. M. Peters, 1997: Quantitative interpretation of laser ceilometer intensity profiles. *J. Atmos. Oceanic Technol.*, **14**, 396–411, doi:10.1175/1520-0426(1997)014\%253C0396\%253AQIOLCI\%253E2.0.CO\%253B2.

Segre, J. and N. Truscott, 1976: Erbium laser ceilometer. *US Patent 3,963,347*.

Seibert, P., F. Beyrich, S.-E. Gryning, S. Joffre, A. Rasmussen, and P. Tercier, 2000: Review and intercomparison of operational methods for the determination of the mixing height. *Atmos. Environ.*, **34**, 1001–1027.

Shephard, M. W., 1998: Haze observations with a laser ceilometer. M.S. thesis, McGill University Department of Atmospheric and Oceanic Sciences, 83 pp., Montreal, Quebec, Canada.

Sicard, M., C. Pérez, F. Rocadenbosch, J. M. Baldasano, and D. García-Vizcaino, 2006: Mixed-layer-depth determination in the Barcelona coastal area from regular lidar measurements: methods, results and limitations. *Bound.-Lay. Meteorol.*, **119**, 135–157, doi:10.1007/s10546-005-9005-9.

Silcox, G., K. Kelly, E. Crosman, C. D. Whiteman, and B. Allen, 2012: Wintertime PM 2.5 concentrations during persistent, multi-day cold-air pools in a mountain valley. *Atmos. Environ.*, **46**, 17–24, doi:10.1016/j.atmosenv.2011.10.041.

Spinhirne, J., J. Reagan, and B. Herman, 1980: Vertical distribution of aerosol extinction cross section and inference of aerosol imaginary index in the troposphere by lidar technique. *J. Appl. Meteor.*, **19**, 426–438.

Stephens, G. L., et al., 2002: The Cloudsat mission and the A-Train. *Bull. Amer. Meteor. Soc.*, **83**, 1771–1790, doi:10.1175/BAMS-83-12-1771.

Steyn, D., M. Baldi, and R. Hoff, 1999: The detection of mixed layer depth and entrainment zone thickness from lidar backscatter profiles. *J. Atmos. Oceanic Technol.*, **16**, 953–959.

Streater, S., 2010: Air Quality Concerns May Dictate Uintah Basin's Natural Gas Drilling Future. The New York Times, URL `http://www.nytimes.com/gwire/2010/10/01/01greenwire-air-quality-concerns-may-dictate-uintah-basins-30342.html`.

Stull, R. B., 1988: *An introduction to boundary layer meteorology*, Vol. 13. Springer, Dordrecht, The Netherlands.

Sugiyama, G. and J. S. Nasstrom, 1999: Methods for Determining the Height of the Atmospheric Boundary Layer. Tech. rep., Lawrence Livermore National Laboratory, 11 pp., Livermore, CA.

Tyndall, D. P., 2011: Sensitivity of surface meteorological analyeses to observation networks. Ph.D. thesis, University of Utah, Salt Lake City, Utah.

U.S. EPA, 2013: National Ambient Air Quality Standards. URL `http://www.epa.gov/air/criteria.html`.

Utah Asthma Program, 2010: Asthma and air pollution: Assosications between asthma emergency department visits, PM2.5 levels, and temperature inversions in Salt Lake County, Utah. Tech. rep., Utah Department of Public Health, 29 pp.

Utah Department of Public Health, 2013: PM2.5 Indicator Report. URL `http://ibis.health.utah.gov/indicator/view/AirQuaPM.Geo.html`.

Vaisala, 2004: Vaisala Ceilometer CL31 User's Guide. Helsinki, Finland.

Van der Kamp, D., 2008: Ceilometer observations of Vancouver's urban boundary layer. M.S. thesis, University of British Columbia, 134 pp., Vancouver, BC.

Vaughan, M. A., et al., 2009: Fully automated detection of cloud and aerosol layers in the CALIPSO lidar measurements. *J. Atmos. Oceanic Technol.*, **26**, 2034–2050, doi:10.1175/2009JTECHA1228.1.

Weissmann, M., F. Braun, L. Gantner, G. J. Mayr, S. Rahm, and O. Reitebuch, 2005: The Alpine mountain–plain circulation: airborne Doppler lidar measurements and numerical simulations. *Mon. Wea. Rev.*, **133**, 3095–3109.

Weitkamp, C., 2005: *Lidar: Range-Resolved Optical Remote Sensing of the Atmosphere.* Springer, New York, 466 pp.

White, A. B., C. J. Senff, and R. M. Banta, 1999: A comparison of mixing depths observed by ground-based wind profilers and an airborne lidar. *J. Atmos. Oceanic Technol.*, **16**, 584–590, doi:10.1175/1520-0426(1999)016⟨0584:ACOMDO⟩2.0.CO;2.

Whiteman, C. D., 1982: Breakup of temperature inversions in deep mountain valleys: Part I. Observations. *J. Appl. Meteor.*, **21**, 270–289.

Whiteman, C. D., X. Bian, and S. Zhong, 1999: Wintertime evolution of the temperature inversion in the Colorado Plateau Basin. *J. Appl. Meteor.*, **38**, 1103–1117.

Whiteman, C. D. and T. McKee, 1982: Breakup of temperature inversions in deep mountain valleys: Part II. Thermodynamic model. *J. Appl. Meteor.*, **21**, 290–302.

Whiteman, C. D., B. Pospichal, S. Eisenbach, P. Weihs, C. B. Clements, R. Steinacker, E. Mursch-Radlgruber, and M. Dorninger, 2004: Inversion breakup in small Rocky Mountain and Alpine basins. *J. Appl. Meteor.*, **43**, 1069–1082.

Whiteman, C. D., S. Zhong, W. J. Shaw, J. M. Hubbe, X. Bian, and J. Mittelstadt, 2001: Cold pools in the Columbia Basin. *Wea. Forecasting*, **16**, 432–447, doi:10.1175/1520-0434(2001)016⟨0432:CPITCB⟩2.0.CO;2.

Whiteman, C. D., et al., 2008: METCRAX 2006 Meteorological experiments in Arizona's Metor Crater. *Bull. Amer. Meteor. Soc.*, **89**, 1665–1680, doi:10.1175/2008BAMS2574.1.

Winker, D. M., J. Pelon, and M. McCormick, 2003: The CALIPSO mission: Spaceborne lidar for observation of aerosols and clouds. *SPIE Vol. 4893*, 1–11.

Wolyn, P. and T. McKee, 1989: Deep stable layers in the intermountain western United States. *Mon. Wea. Rev.*, **117**, 461–472.

Zängl, G., 2002: An improved method for computing horizontal diffusion in a sigma-coordinate model and its application to simulations over mountainous topography. *Mon. Wea. Rev.*, **130**, 1423–1432.

Zängl, G., 2005: Wintertime cold-air pools in the Bavarian Danube Valley Basin: Data analysis and idealized numerical simulations. *J. Appl. Meteor.*, **44**, 1950–1971.

Zardi, D. and C. D. Whiteman, 2012: Diurnal mountain wind systems. *Chapter 2 in Mountain Weather Research and Forecasting*, F. K. Chow, S. F. De Wekker, and B. J. Snyder, Eds., Springer Netherlands, Dordrecht, Springer Atmospheric Sciences, doi:10.1007/978-94-007-4098-3.

Zhong, S., X. Bian, and C. D. Whiteman, 2003: Time scale for cold-air pool breakup by turbulent erosion. *Meteorol. Z.*, **12**, 229–233, doi:10.1127/0941-2948/2003/0012-0231.

Zhong, S., C. D. Whiteman, X. Bian, W. J. Shaw, and J. M. Hubbe, 2001: Meteorological processes affecting the evolution of a wintertime cold air pool in the Columbia basin. *Mon. Wea. Rev.*, **129**, 2600–2613.

Zhong, S., X. Xu, X. Bian, and W. Lu, 2011: Climatology of persistent deep stable layers in Utah's Salt Lake Valley, USA. *Adv. Sci. Res.*, **6**, 59–62, doi:10.5194/asr-6-59-2011.

Zoumakis, N. and G. Efstathiou, 2006: Parameterization of inversion breakup in idealized valleys. Part I: The adjustable model parameters. *J. Appl. Meteor. Climatol.*, **45**, 600–608.